

MEASUREMENT OF  $Z + \gamma$  PRODUCTION AND SEARCH  
FOR ANOMALOUS TRIPLE GAUGE COUPLINGS IN  
PROTON-ANTIPROTON COLLISIONS AT  
 $\sqrt{S} = 1.96$  TEV

by

Jianrong Deng

Department of Physics  
Duke University

Date: \_\_\_\_\_

Approved: \_\_\_\_\_

\_\_\_\_\_  
Alfred T. Goshaw, Supervisor

\_\_\_\_\_  
Haiyan Gao

\_\_\_\_\_  
Mark C. Kruse

\_\_\_\_\_  
Thomas C. Mehen

\_\_\_\_\_  
Richard G. Palmer

Dissertation submitted in partial fulfillment of the  
requirements for the degree of Doctor of Philosophy  
in the Department of Physics  
in the Graduate School of  
Duke University

2008

# ABSTRACT

(Physics - High Energy)

## MEASUREMENT OF $Z + \gamma$ PRODUCTION AND SEARCH FOR ANOMALOUS TRIPLE GAUGE COUPLINGS IN PROTON-ANTIPROTON COLLISIONS AT $\sqrt{S} = 1.96$ TEV

by

Jianrong Deng

Department of Physics  
Duke University

Date: \_\_\_\_\_

Approved: \_\_\_\_\_

\_\_\_\_\_  
Alfred T. Goshaw, Supervisor

\_\_\_\_\_  
Haiyan Gao

\_\_\_\_\_  
Mark C. Kruse

\_\_\_\_\_  
Thomas C. Mehen

\_\_\_\_\_  
Richard G. Palmer

An abstract of a dissertation submitted in partial fulfillment of the  
requirements for the degree of Doctor of Philosophy  
in the Department of Physics  
in the Graduate School of  
Duke University

2008

Copyright © 2008 by Jianrong Deng  
All rights reserved

# Abstract

We present a measurement of  $p\bar{p} \rightarrow Z \gamma + X \rightarrow e^+e^-\gamma + X$  production using proton-antiproton collision data collected at the Collider Detector at Fermilab at a center of mass energy of 1.96 TeV.  $Z\gamma$  production provides a direct test of the triple neutral gauge couplings. A measurement of  $Z\gamma$  production cross section and search for anomalous  $ZZ\gamma$  and  $Z\gamma\gamma$  couplings are presented.

The data presented are from  $1.1 \text{ fb}^{-1}$  of  $p\bar{p}$  integrated luminosity collected at the CDF Detector. Electrons from Z decays are selected with  $E_t > 20 \text{ GeV}$ . Photons ( $E_t > 7 \text{ GeV}$ ) are required to be well-separated from the electrons. There are 390  $ee\gamma$  candidate events found with  $1.1 \text{ fb}^{-1}$  of data, compared to the SM prediction of  $375.3 \pm 25.2$  events. The Standard Model prediction for the cross section for  $p\bar{p} \rightarrow e^+e^-\gamma + X$  production at  $\sqrt{s} = 1.96 \text{ TeV}$  is  $4.5 \pm 0.4 \text{ pb}$ . The measured cross section is  $4.7 \pm 0.6 \text{ pb}$ . The cross section and kinematic distributions of the  $ee\gamma$  events are in good agreement with theoretical predictions.

Limits on the  $ZZ\gamma$  and  $Z\gamma\gamma$  couplings are extracted using the photon  $E_t$  distribution of  $ee\gamma$  events with  $M_{ee\gamma} > 100 \text{ GeV}/c^2$ . These are the first limits measured using CDF Run II data. These limits provide important test of the interaction of the photon and the Z boson.



*Dedicated to my father and grandfather*

# Acknowledgements

I am grateful to all the people who have given me support and encouragement over the years.

I am immensely grateful to my advisor, Al Goshaw, for his guidance, encouragement and support. I admire his energy and enthusiasm for high energy physics. Thank you for all you have taught me. I am thankful to members of the Duke HEP group: Ashutosh Kotwal and Mark Kruse for their advice and support.

Thanks to the WZgamma working group: Beate Heinemann, Jefferson Kist, Chris Lester, Ai Nagano and Tom Phillips. Thank you all for your hard work and for getting our project done. Special thanks go to Chris Lester for providing an important background measurement for my analysis. I am grateful to Chris Hays for helping me get started on my project and all the help on using the Duke Ntuple for an electron/photon analysis. Thanks to Yimei Huang for providing me her analysis codes and answering my questions. I am deeply thankful to the Diboson, photon and EWK working groups for help and advice in the completion of this analysis: Elliot Lipeles, Mark Neubauer, Eva Halkiadakis, Eric James, Peter Renton, Max Goncharov and Raymond Culbertson. Thanks to Shih-Chieh Hsu and Doug Benjamin for generating all the  $Z\gamma$  simulation samples for me. I am thankful to Uli Baur for all the discussion and help with the ZGAMMA program.

Thanks to Dean for sharing an office with me and being the best office mate I could ask for. Thanks to Heather for letting me have Barney and Mugsy from time to time, and proof-reading the first chapters of my thesis. Thanks to Bo for pushing me and helping me get started on my job applications. Thanks to Jie for her kindness in taking good care of me every time I went back to Duke for a short visit. Thanks to Junhua, Zhenglei and Peidong for providing me a place to stay at Duke and for

their hospitality. Thanks to Carolyn for her care and kindness, especially for helping me through my first semester at Duke. Thanks to Nils for helping me on the TDC project. Thanks to Yi for ice skating with me and sending me the best comic books. Thanks to Rick for all the joyful hours riding on the bike paths along the fox river and forest. Thanks to Eiko, Sunny, Shih-Chieh, RongShang, SongMing, Yen-Chu Chen and Yanjun for the happy holiday gatherings. I thank my friends for their friendship and support: Carolyn, Dean, Fangyan, Heather, Jie, Junhua, Zhenglei, Yi... It won't be the same without your support and friendship.

I thank Jun for his support and love. Thank you for always being there when I needed you most. I thank my family for their support and encouragement. I dedicate this thesis to my father and grandfather. Without their encouragement, I would never have gotten this far.

# Contents

<b>Abstract</b>	<b>iv</b>
<b>Acknowledgements</b>	<b>vi</b>
<b>List of Figures</b>	<b>xiv</b>
<b>List of Tables</b>	<b>xx</b>
<b>1 Introduction</b>	<b>1</b>
1.1 The Standard Model of Particle Physics . . . . .	1
1.1.1 The Fundamental Particles – Fermions . . . . .	1
1.1.2 Force Carriers – Bosons . . . . .	2
1.1.3 The Hadrons . . . . .	4
1.1.4 The Higgs Boson . . . . .	5
1.2 The SM Electroweak Theory . . . . .	5
1.3 The SM Quantum Chromodynamics Theory . . . . .	7
1.4 Terminology in Particle Physics . . . . .	8
1.5 Thesis Overview . . . . .	10
<b>2 Experimental Overview of Gauge Boson Measurements</b>	<b>11</b>
2.1 Experimental Verifications of the SM Electroweak Theory . . . . .	11
2.1.1 Observations of Charged and Neutral Currents . . . . .	11
2.1.2 The Discovery of the W and Z Bosons at CERN . . . . .	12
2.1.3 The Search for the Higgs Boson . . . . .	13
2.2 Motivation for the Studies of Gauge Boson Pairs . . . . .	14
2.3 Gauge Boson Measurements . . . . .	14

2.3.1	At the $e^+e^-$ Collider at CERN . . . . .	14
2.3.2	At the Tevatron $p\bar{p}$ Collider at $\sqrt{s} = 1.96$ TeV . . . . .	17
<b>3</b>	<b>The Tevatron Collider at Fermilab</b>	<b>21</b>
3.1	Introduction . . . . .	22
3.1.1	Synchrotron . . . . .	24
3.2	The Fermilab Tevatron Accelerator System . . . . .	25
3.2.1	The Proton Source . . . . .	25
3.2.2	The Main Injector . . . . .	26
3.2.3	The Anti-Proton Source . . . . .	26
3.2.4	The Recycler . . . . .	28
3.2.5	The Tevatron . . . . .	29
3.3	Tevatron Luminosity . . . . .	29
3.4	Discoveries at Fermilab . . . . .	31
3.4.1	The discovery of the bottom quark (1977) . . . . .	31
3.4.2	The discovery of the top quark (1995) . . . . .	32
3.5	Chapter Summary . . . . .	32
<b>4</b>	<b>The CDF Experiment</b>	<b>33</b>
4.1	Introduction: Particle Detection . . . . .	33
4.1.1	Drift Chambers . . . . .	34
4.1.2	Calorimeters . . . . .	36
4.1.3	Muon Detectors . . . . .	39
4.2	The Collider Detector at Fermilab . . . . .	40
4.2.1	The CDF Coordinate System . . . . .	41
4.2.2	CDF Center Outer Tracking (COT) . . . . .	43

4.2.3	Inner Tracker . . . . .	46
4.2.4	Calorimeter . . . . .	47
4.2.5	Muon Systems . . . . .	49
4.3	Trigger and Data Acquisition Systems . . . . .	50
4.4	Chapter Summary . . . . .	53
<b>5</b>	<b>Gauge Boson Pair Production and Trilinear Couplings</b>	<b>54</b>
5.1	Triple Gauge Boson Couplings . . . . .	54
5.1.1	Charge Triple Gauge Boson Couplings . . . . .	56
5.1.2	Neutral Triple Gauge Boson Couplings . . . . .	57
5.2	$p\bar{p} \rightarrow Z \gamma + X$ Production . . . . .	59
5.3	$p\bar{p} \rightarrow l^+ l^- \gamma$ Production Calculation . . . . .	60
5.3.1	Leading Order (LO) Cross Section . . . . .	61
5.3.2	Next-to-Leading Order (NLO) Corrections . . . . .	63
5.4	Chapter Summary . . . . .	67
<b>6</b>	<b>Z Boson Event Selection</b>	<b>69</b>
6.1	Overview of the Measurement of $Z \rightarrow ee$ Cross Section . . . . .	69
6.2	Selection of Datasets . . . . .	70
6.2.1	High $P_t$ Electron Datasets and Good Run List . . . . .	70
6.2.2	Detector Simulation Samples . . . . .	71
6.3	Electron Selection . . . . .	72
6.3.1	Central Electron Identification . . . . .	72
6.3.2	Plug Electron Identification . . . . .	75
6.3.3	Electron energy correction . . . . .	79
6.4	Acceptance . . . . .	81

6.4.1	Detector Simulation Samples . . . . .	82
6.4.2	Acceptance in the CC Region . . . . .	82
6.4.3	Acceptance in the CP Region . . . . .	83
6.4.4	Correction for slow trigger efficiency turning on at low $P_t$ . . .	84
6.5	Electron identification Efficiency Measurement . . . . .	85
6.5.1	Central Electron Identification Efficiencies . . . . .	85
6.5.2	Plug Electron identification Efficiency . . . . .	88
6.6	Trigger Efficiency . . . . .	91
6.6.1	ELECTRON_CENTRAL_18 Trigger Efficiency . . . . .	92
6.6.2	Z_NOTRACK Trigger Efficiency . . . . .	97
6.6.3	Total Trigger Efficiency . . . . .	101
6.7	Background Estimation . . . . .	101
6.7.1	QCD background shape . . . . .	101
6.7.2	QCD Background Estimation – Side-band Subtraction Method	102
6.7.3	Systematic Uncertainties . . . . .	104
6.8	Chapter Summary . . . . .	105
<b>7</b>	<b>Inclusive Z Cross Section Measurement</b>	<b>107</b>
7.1	Previous measurements . . . . .	107
7.2	The Inclusive Z Cross Section in the Channel with Two Central Electrons	108
7.2.1	Measure Inclusive Z Cross Section in CP Channel . . . . .	110
7.3	Measurement of the Inclusive Z Cross Section – $1 \text{ fb}^{-1}$ . . . . .	111
<b>8</b>	<b>Photon Selection, Identification and Background Study</b>	<b>112</b>
8.1	Photon Selection Criteria . . . . .	112
8.2	Photon identification efficiency . . . . .	114

8.3	Photon Background . . . . .	122
8.3.1	Overview of the fake rate measurement . . . . .	122
8.3.2	Raw Fake Rate Measurement . . . . .	124
8.3.3	Real Photon Correction . . . . .	126
8.3.4	True Fake Rate . . . . .	131
8.3.5	Quark/gluon Ratio Correction . . . . .	132
8.4	Chapter Summary . . . . .	133
<b>9</b>	<b>Cross Section Measurement of <math>p\bar{p} \rightarrow e^+e^-\gamma + X</math> Production</b>	<b>134</b>
9.1	$Z\gamma$ Event Selection . . . . .	134
9.1.1	Z Selection . . . . .	134
9.1.2	$Z\gamma$ Event Selection in the Central Photon Channel . . . . .	136
9.2	Total $Z\gamma$ Event Selection Efficiency . . . . .	136
9.3	Background Estimation . . . . .	137
9.3.1	Z + jet QCD Background . . . . .	138
9.3.2	$\gamma$ + Jet QCD Background . . . . .	139
9.4	$Z\gamma$ Cross Section Calculation . . . . .	140
9.5	Systematic Uncertainties . . . . .	141
9.6	$Z\gamma$ Cross Section Measurement . . . . .	143
9.6.1	Previous measurement . . . . .	143
9.6.2	$Z\gamma$ Cross Section Result . . . . .	144
9.6.3	$Z\gamma$ Event Display . . . . .	151
<b>10</b>	<b>Anomalous Triple Gauge Boson Couplings</b>	<b>155</b>
10.1	Current Limits on $ZZ\gamma$ and $Z\gamma\gamma$ Couplings . . . . .	155
10.2	Anomalous Gauge Couplings (AGC) . . . . .	156



10.3 Anomalous Coupling Monte Carlo Samples . . . . .	158
10.4 Reconstruction Efficiency . . . . .	158
10.5 Setting Limits on Anomalous Gauge Couplings . . . . .	159
10.5.1 Expected limits . . . . .	161
10.5.2 Uncertainties on expected limits . . . . .	162
10.6 Results . . . . .	163
10.7 Combine $Z \rightarrow ee$ and $Z \rightarrow \mu\mu$ Channels . . . . .	164
10.8 Chapter Summary . . . . .	165
<b>11 Summary and Conclusion</b>	<b>167</b>
<b>Appendix</b>	<b>169</b>
<b>A Electroweak Theory</b>	<b>170</b>
A.1 Local Gauge Symmetry . . . . .	170
A.2 Spontaneously Symmetry Breaking . . . . .	172
A.3 The Higgs Mechanism . . . . .	173
A.4 The GSW Electroweak Theory . . . . .	175
<b>Bibliography</b>	<b>178</b>
<b>Biography</b>	<b>184</b>

# List of Figures

1.1	The fundamental particles of ordinary matter [1]. . . . .	2
1.2	The three generations of the fundamental particles [1]. . . . .	3
1.3	The elementary matter particles and force carrier particles in the SM [2].	4
1.4	Baryons and mesons. [3]. . . . .	6
2.1	An example of a charged current. . . . .	12
2.2	An example of a neutral current. . . . .	12
2.3	W-pair production. . . . .	16
2.4	Z-pair production. . . . .	17
3.1	Accelerator Complex Overview [22]. . . . .	21
3.2	A Radio Frequency(RF) cavity [23]. . . . .	22
3.3	A Radio Frequency(RF) cavity [24]. . . . .	23
3.4	A radio frequency accelerator [25]. . . . .	23
3.5	The magnetic force [26]. . . . .	24
3.6	The Linac drift tube [27]. . . . .	26
3.7	Fermilab anti-proton target station [28]. . . . .	27
3.8	The Stochastic Cooling System [28]. . . . .	28
3.9	Run II Tevatron luminosity summary [30]. . . . .	30
3.10	2006 Tevatron luminosity projection curves [30]. . . . .	31
4.1	The interaction of various particles with the different components of a detector [32]. . . . .	34

4.2	Sense wire in drift chamber [33]. . . . .	35
4.3	Tracking [33]. . . . .	35
4.4	CDF calorimeter coverage (sideview) [36]. . . . .	37
4.5	Sampling calorimeters [37]. . . . .	38
4.6	A muon detector system [38]. . . . .	40
4.7	Drift Chambers (in blue) with resistance readout wires (in red) [38]. .	41
4.8	A simple module of charge division [39]. . . . .	41
4.9	CDF detector cutaway view [36]. . . . .	42
4.10	CDF inner detector cutaway view [36]. . . . .	43
4.11	Longitudinal view of the CDF tracking system [40]. . . . .	44
4.12	Super cell layout [41]. . . . .	45
4.13	An overview of the COT readout electronics [41]. . . . .	46
4.14	Functional block diagram of the CDF Run II data flow [43]. . . . .	51
4.15	Block diagram of the CDF Run IIa trigger system [43]. . . . .	52
5.1	Feynman diagrams for gauge boson pair production. $V_{0,1,2}$ are the photon, W or Z gauge boson [45]. . . . .	55
5.2	The general neutral gauge boson vertex $V_1 V_2 V_3$ [49]. . . . .	58
5.3	The neutral gauge boson vertex. (a) $Z\gamma V$ vertex and (b) $ZZV$ vertex ( $V = Z$ or $\gamma$ ). . . . .	58
5.4	The leading order Feynman diagrams for $p\bar{p} \rightarrow ll\gamma$ production in the SM. [50] . . . . .	60
5.5	Anomalous $ZZ\gamma$ and $Z\gamma\gamma$ contributions to $p\bar{p} \rightarrow ll\gamma$ production. [50] .	61

5.6	LHAPDF CTEQ 6L PDF sets and cross section. Green line is the cross section from the PDF central value, pink and light green lines are the uncertainties calculated from the 40 sets. . . . .	62
5.7	$ll\gamma$ Mass distribution in $Z\gamma$ production [50]. High mass region is most sensitive to anomalous couplings. Solid curve: SM; dash-dotted curve: anomalous couplings. . . . .	63
5.8	Higher order QCD corrections (virtual and real gluon emissions) to $p\bar{p} \rightarrow Z\gamma + X$ production [53]. The diagrams obtained by interchanging the Z and the $\gamma$ are not shown. . . . .	64
5.9	Photon $E_t$ distribution. The solid curve is calculated with LO PDF, the dashed curve is with NLO PDF. . . . .	65
5.10	The k-factor curves calculated with LO PDF for LO cross section (solid curve) vs NLO PDF for LO cross section (dashed curve). . . . .	66
5.11	K-factor. SM: $h_3^Z=0$ and $h_4^Z=0$ . . . . .	67
5.12	K factor curves from different anomalous gauge couplings. SM: $h_3^Z=0$ and $h_4^Z=0$ . Assign the difference as systematic uncertainty. . . . .	68
6.1	Track $z0$ of the second electron legs in the $Z \rightarrow ee$ candidate events, with $66 \text{ GeV}/c^2 < M_Z < 116 \text{ GeV}/c^2$ , and the first electron legs satisfy all the loose central electron identification cuts (see Table 6.4). The arrows show the cuts applied to the $z0$ variable. . . . .	73
6.2	Unscaled di-electron mass spectra, data vs simulation. . . . .	80
6.3	Scaled di-electron mass spectra, data vs simulation. . . . .	81
6.4	Electron_Central_18 trigger efficiency as a function of electron $P_t$ (GeV/c). Slow turn on at low $P_t$ , apply trigger Efficiency weight to MC event by event for one dataset (bhel0d) . . . . .	96
6.5	ZNOTRACK trigger efficiency in the plug region (for one dataset bhel0d), as a function of the second Electron $E_t$ (GeV), 28 GeV $E_t$ cut on the first electron. Slow turn on at low $E_t$ , a trigger efficiency weight is applied to MC event by event. . . . .	100

6.6	Di-lepton mass distribution ( $\text{GeV}/c^2$ ) in Zee CP background subtraction for one dataset (bhel0h). . . . .	104
8.1	$Z\gamma$ Final State Radiation (FSR). . . . .	115
8.2	The invariant mass ( $\text{GeV}/c^2$ ) distribution of the $ee\gamma$ three-body system with $1 \text{ fb}^{-1}$ electron data. . . . .	117
8.3	Three body mass ( $\text{GeV}/c^2$ ) distribution of the $Z\gamma$ events used in photon detection efficiency measurement. $Z\gamma$ 1fb electron data (left), $Z(\text{ee})\gamma$ detector simulation sample <i>rewk33</i> (right). . . . .	117
8.4	Central Photon N-1 detection efficiency as a function of photon $E_t$ (GeV) measured from $Z\gamma$ simulation sample. . . . .	120
8.5	Central Photon detection efficiency as a function of $\eta$ measured from $Z\gamma$ simulation sample. . . . .	120
8.6	Central Photon detection efficiencies as a function of photon $E_t$ (GeV), data vs simulation. . . . .	121
8.7	Raw fake rate with error bands and central fit. . . . .	125
8.8	The signal ( $\epsilon_{\text{gamma}}$ ) and background ( $\epsilon_b$ ) templates for the CES method [54]. . . . .	127
8.9	Iso/ $E_t$ vs $\chi^2$ . Illustrated are the four regions A, B, C and D used for determining the QCD background fraction $F_{QCD}$ [54]. . . . .	128
8.10	The conversion probabilities for signal prompt photons ( $P_{\text{conv}}^\gamma$ ) and background mesons ( $P_{\text{conv}}^{QCD}$ ) as a function of $E_t$ [54]. . . . .	129
8.11	$F_{QCD}$ using three methods: Iso vs CES $\chi^2$ , CES weighting and CPR weighting. Solid lines are the upper and lower error bands and the dashed line is central fit curve. . . . .	131
8.12	True fake rate $P_{\text{true}}^{QCD}(E_t)$ as a function of jet $E_t$ (GeV) for QCD jet sample with error bands(solid), central fit(dashed), and old measurement with $200 \text{ pb}^{-1}$ of data [68]. . . . .	132
8.13	True fake rate for the $Z + \text{jet}$ sample. . . . .	133

9.1	$ee\gamma$ event kinematics. $E_t^\gamma > 7$ GeV, $\Delta R_{e\gamma} > 0.7$ , $M_{ee} > 40$ GeV/ $c^2$ .	146
9.2	Data $M_{ee}$ - $M_{ee\gamma}$ Distribution, CC + CP, 1fb $^{-1}$ , 7 GeVphoton $E_t$ cut.	147
9.3	FSR $ee\gamma$ events, $E_t^\gamma > 7$ GeV, $\Delta R_{e\gamma} > 0.7$ , $M_{ee} > 40$ GeV/ $c^2$ and $M_{ee\gamma} \leq 100$ GeV/ $c^2$ .	148
9.4	ISR $ee\gamma$ events, $E_t^\gamma > 7$ GeV, $\Delta R_{e\gamma} > 0.7$ , $M_{ee} > 40$ GeV/ $c^2$ and $M_{ee\gamma} > 100$ GeV/ $c^2$ .	150
9.5	The COT view and the calorimeter tower view of the highest photon $E_t$ event, event 69435 in run 161830.	151
9.6	The COT view and the calorimeter tower view of the highest $M_{ee\gamma}$ event, event 619905 in run 161555.	152
9.7	The COT view and the calorimeter tower view of the highest $P_t^{ee\gamma}$ event, event 3732149 in run 162857.	153
9.8	The COT view and the calorimeter tower view of a very high $M_{ee}$ event, event 5975330 in run 186048.	154
10.1	$l\gamma$ Mass distribution in $Z\gamma$ production [50]. High mass region is most sensitive to anomalous couplings. Dashed line: FSR; dotted line: ISR; solid curve: SM; dash-dotted curve: anomalous couplings.	156
10.2	Photon $E_t$ distribution for $ee\gamma$ events with $M_{ee\gamma} > 100$ GeV/ $c^2$ . Electron 1fb $^{-1}$ .	157
10.3	Universal efficiency $N_{Rec}(E_t^\gamma) / N_{Accp}(E_t^\gamma)$ for ISR $Z\gamma$ events with CC Z's (upper curves) and CP Z's (lower curves). SM vs AGC.	159
10.4	Likelihood distribution as a function of $h_3^Z$ from data. $h_3^Z$ 95% C.L. observed limit: 0.124	160
10.5	Likelihood distribution as a function of $h_4^Z$ from data. $h_4^Z$ 95% C.L. observed limit: 0.0074.	160
10.6	Likelihood distribution as a function of $h_3^\gamma$ from data. $h_3^\gamma$ 95% C.L. observed limit: 0.13.	161

10.7	Likelihood distribution as a function of $h_4^\gamma$ from data. $h_4^\gamma$ 95% C.L. observed limit: 0.0074. . . . .	161
10.8	Expected lower and upper limit of $h_3^Z$ from pseudo-experiments: 0.128, 0.128], 1 $\sigma$ = 0.0196 (stat only). . . . .	162
10.9	Photon $E_t$ distribution for $ee\gamma$ events with $M_{ee\gamma} > 100$ GeV/ $c^2$ . Elec- tron 1 fb $^{-1}$ + Muon 2 fb $^{-1}$ . . . . .	166

# List of Tables

1.1	Units in high energy physics [5]. . . . .	8
2.1	Measurements of diboson pair production at CDF. . . . .	19
2.2	WWZ anomalous couplings limits at 95% C.L from $p\bar{p} \rightarrow WZ + X$ measurement based on $1.9 \text{ fb}^{-1}$ of data at CDF [17]. . . . .	20
2.3	95% C.L. limits on $Z\gamma$ anomalous couplings. . . . .	20
3.1	A summary of the Tevatron accelerator systems. . . . .	29
4.1	The $\eta$ coverage of the CDF muon detectors. . . . .	49
4.2	DAQ and trigger specification, Run IIa vs IIb [44]. . . . .	53
6.1	High $P_t$ electron datasets and the integrated luminosities. . . . .	71
6.2	Pythia $Z \rightarrow ee$ MC samples. . . . .	71
6.3	Central electron selection: track quality requirements . . . . .	73
6.4	Event selection: loose central electron(LCE) identification cuts. The text in bold shows the cut that is different to the standard central electron identification cut. . . . .	76
6.5	Electron selection: tight central electron (TCE) identification cuts . .	76
6.6	The standard loose plug electron identification cuts. . . . .	77
6.7	The loose plug electron (LPE) identification cuts in this analysis, the text in bold shows the cut that is different to the standard electron identification cut. . . . .	77
6.8	Tight plug electron(TPE) identification cuts used in this analysis , the text in bold shows the cut that is different to the standard electron identification cut. . . . .	79
6.9	Standard tight plug electron identification cuts. . . . .	79



6.10	Z Peak positions from the unscaled data and simulation samples . . .	81
6.11	Energy scale factors . . . . .	81
6.12	$Z \rightarrow ee$ CC channel Selection Acceptance. zewk6d MC . . . . .	83
6.13	$Z \rightarrow ee$ CP channel Selection Acceptance. Statistical uncertainties are shown. Using zewk6d MC sample, 0d dataset run range. . . . .	84
6.14	Input parameters to central electron identification and isolation efficiency measurements using number of electrons in central-central $Z \rightarrow ee$ candidates. bhel0d dataset . . . . .	87
6.15	The efficiencies and scale factors for central electron, bhel0d/0h/0i dataset. . . . .	88
6.16	Input parameters to plug electron identification and isolation efficiency measurements using central-plug $Z \rightarrow ee$ candidates for one dataset (bhel0d) . . . . .	90
6.17	The efficiencies and scale factors for plug electron, bhel0d/0h/0i dataset.	91
6.18	ELECTRON_CENTRAL_18 trigger path, PHYSICS_3.00[3] . . . . .	93
6.19	$W \rightarrow e\nu$ Event selection . . . . .	94
6.20	ELECTRON_CENTRAL_18 trigger Efficiency, data collected before run 159603. No Lshr and $\Delta z$ cuts in the loose central electron selection.	95
6.21	ELECTRON_CENTRAL_18 trigger efficiency, data collected after run 159603. No Lshr and $\Delta z$ cuts in the loose central electron selection.	95
6.22	ELECTRON_CENTRAL_18 trigger efficiency, with Lshr and $\Delta z$ cuts in the loose central electron selection for one dataset (bhel0d). $P_t > 9$ GeV/ $c$ . . . . .	96
6.23	Z_NOTRACK trigger path, from Physics Table: PHYSICS_2.05[17] .	98
6.24	Z_NOTRACK Efficiency from CC Z events for one dataset (bhel0d).	99
6.25	Z_NOTRACK Efficiency from CP Z events, bhel0d dataset . . . . .	99

6.26	Central loose electron ID Cuts and central jet selection cuts . . . . .	102
6.27	Plug loose electron ID cuts and plug jet selection cuts . . . . .	102
6.28	CC Z QCD background prediction for one dataset (bhel0d). . . . .	105
6.29	CP Z QCD background prediction for one dataset (bhel0d). . . . .	105
7.1	Cross-section calculation for $\sigma(p\bar{p} \rightarrow Z/\gamma^* + X) \cdot Br(Z/\gamma^* \rightarrow ee)$ . . .	111
8.1	Central photon identification cuts. . . . .	113
8.2	Central photon denominator cuts for identification efficiency measurement. . . . .	115
8.3	Muon+Electron Channel Central Photon total detection efficiency and N-1 detection efficiency from data . . . . .	119
8.4	Electron Channel Central Photon total detection efficiency and N-1 detection efficiency for detector simulation samples. . . . .	119
8.5	Central photon efficiency scale factor. . . . .	119
8.6	Old method. Photon detection efficiencies and scale factors using Zee samples [66]. $E_t^\gamma > 15$ GeV, $ \eta  < 1.1$ . . . . .	121
8.7	Photon detection efficiencies and scale factors using FSR photon samples. $E_t^\gamma > 7$ GeV, $ \eta  < 1.1$ . . . . .	122
9.1	Loose central electron identification cuts. The text in red shows the cut that is different to the standard central electron identification cut. . . . .	135
9.2	Loose plug electron identification cuts, the text in red shows the cut that is different to the standard plug electron identification cut. . . . .	135
9.3	A summary of the uncertainties for the $ee\gamma$ cross-section calculation and their correlations between CC and CP channels. A 'x' indicates the uncertainty is applied to that channel and thus correlated to the other channel with the same systematic. . . . .	144

9.4	Input parameters to the $ee\gamma$ cross-section calculation, $1074pb^{-1}$ . $E_t^\gamma > 7$ GeV, $\Delta R_{e\gamma} > 0.7$ and $M_{ee} > 40$ GeV/ $c^2$ . . . . .	145
9.5	Input parameters to the FSR $ee\gamma$ cross-section calculation, $1074pb^{-1}$ . $E_t^\gamma > 7$ GeV, $\Delta R_{e\gamma} > 0.7$ , $M_{ee} > 40$ GeV/ $c^2$ and $M_{ee\gamma} < 100$ GeV/ $c^2$ . . . . .	147
9.6	Input parameters to the ISR $ee\gamma$ cross-section calculation, $1074pb^{-1}$ . $E_t^\gamma > 7$ GeV, $\Delta R_{e\gamma} > 0.7$ , $M_{ee} > 40$ GeV/ $c^2$ and $M_{ee\gamma} > 100$ GeV/ $c^2$ . . . . .	149
9.7	The highest $E_t^\gamma$ $Z\gamma$ event . . . . .	151
9.8	The highest $M_{ee\gamma}$ $Z\gamma$ event . . . . .	152
9.9	The highest $P_t^{ee\gamma}$ event . . . . .	153
9.10	The very high $M_{ee}$ $Z\gamma$ event . . . . .	154
10.1	95% C.L. limits on $Z\gamma$ anomalous couplings. . . . .	155
10.2	95% C.L. limits on $Z\gamma$ anomalous couplings using $1fb^{-1}$ electron data. . . . .	163
10.3	Input parameters to the ISR $\mu\mu\gamma$ cross-section calculation, $2007 pb^{-1}$ . $E_t^\gamma > 7$ GeV, $\Delta R_{l\gamma} > 0.7$ , $M_{ll} > 40$ GeV/ $c^2$ and $M_{ll\gamma} > 100$ GeV/ $c^2$ . . . . .	164
10.4	Input parameters to the ISR $ee\gamma + \mu\mu\gamma$ cross-section calculation, $1074$ (e) + $2007$ ( $\mu$ ) $pb^{-1}$ . $E_t^\gamma > 7$ GeV, $\Delta R_{l\gamma} > 0.7$ , $M_{ll} > 40$ GeV/ $c^2$ and $M_{ll\gamma} > 100$ GeV/ $c^2$ . . . . .	165
10.5	Limits (95% C.L.) for e + $\mu$ combined . . . . .	165

# Chapter 1

## Introduction

### 1.1 The Standard Model of Particle Physics

The Standard Model (SM) of particle physics is a theory that describes fundamental particles and their interactions. The Standard Model was developed in the 1970s and has been tested and verified by experiments over the past three decades. A brief review of the Standard Model is given in this chapter.

#### 1.1.1 The Fundamental Particles – Fermions

Ordinary matter is made up of atoms, which are formed from electrons and atomic nuclei composed of protons and neutrons. As illustrated in Figure 1.1, two up quarks and one down quark bind together to form protons, while one up and two down quarks form neutrons. The electron (e), the up quark (u) and the down quark (d) are examples of fundamental matter particles in the SM. The fundamental particles are divided into leptons and quarks, and are further grouped into three generations based upon their mass. The leptons and quarks are spin 1/2 particles (fermions). There are three leptons with electric charge -1 (“-1” =  $-1.6 \times 10^{-19}$  C), the electron (e), muon ( $\mu$ ) and tau lepton ( $\tau$ ) and three electrically neutral leptons, the neutrinos  $\nu_e$ ,  $\nu_\mu$  and  $\nu_\tau$ . For each lepton, there is an antilepton with an opposite charge. There are six leptons and six antileptons. There are three quarks with electric charge 2/3, up (u), charm (c) and top (t), and three with electric charge -1/3, down (d), strange (s) and bottom (b). For each quark, there is an antiquark with an opposite charge.

Each quark and antiquark comes in three colors, so there are a total of 36 strongly interacting fermions. The electron, the electron neutrino, the up quark and the down quark, together form the first generation. The second and third generations, shown in Figure 1.2, are heavier duplicates of the first generation. The mass of the top quark is a factor of  $10^5$  larger than that of the electron.

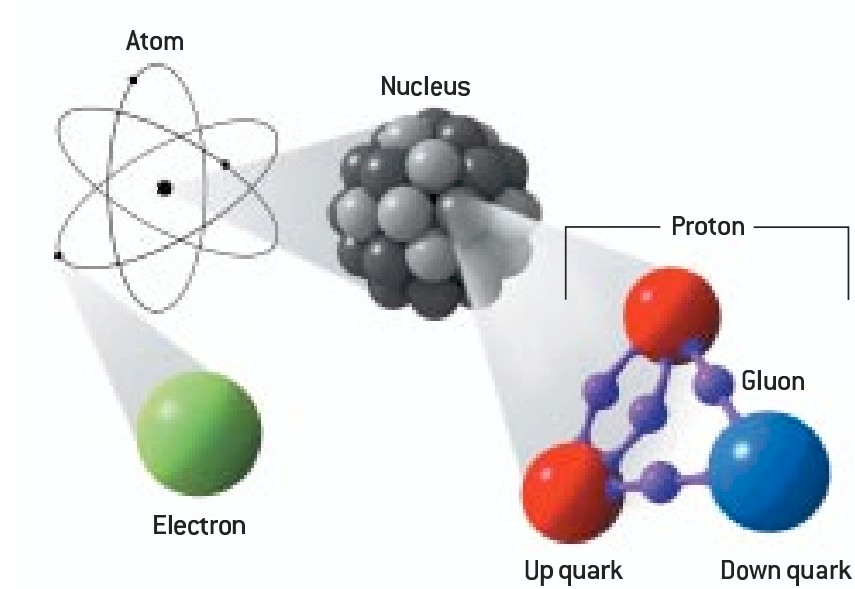


**Figure 1.1:** The fundamental particles of ordinary matter [1].

### 1.1.2 Force Carriers – Bosons

There are four known forces: the strong force (which binds protons and neutrons together inside atomic nuclei), the weak force (which allows neutrons to decay to protons), the electromagnetic force and the gravitational force. The first three forces are described by the Standard Model. The Standard Model successfully unifies the electromagnetic force and the weak force into an electroweak force. Photons are particles that mediate the electromagnetic interaction. The mediators of the weak interaction are W and Z bosons. The Standard Model quantum chromodynamics

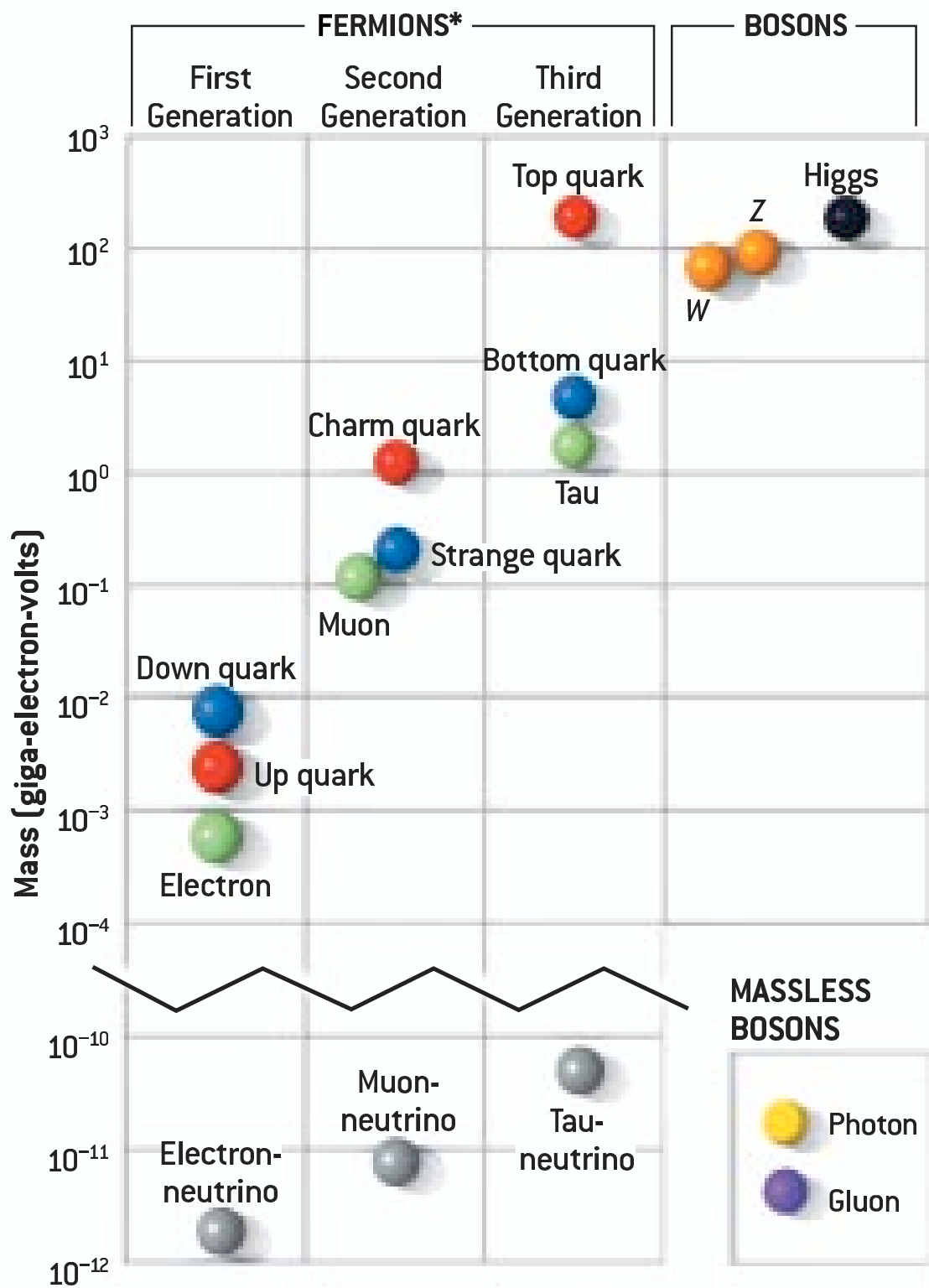


**Figure 1.2:** The three generations of the fundamental particles [1].

(QCD) theory describes the strong interaction. Gluons (g) mediate this interaction. These force carriers are spin 1 particles (bosons). The SM has been very successful in describing the strong, weak and electromagnetic interactions.

These elementary particles of matter and force carriers are summarized in Figure 1.3.

Force		Carrier	
Electromagnetic		Photon	
Weak		$W^\pm, Z$	
Strong		Gluon	

Leptons				Quarks			
Electric charge $-1$		Electric charge $0$		Electric charge $+2/3$		Electric charge $-1/3$	
Electron	$e^-$	Electron neutrino	$\nu_e$	Up	$u$	Down	$d$
Muon	$\mu^-$	Muon neutrino	$\nu_\mu$	Charm	$c$	Strange	$s$
Tau	$\tau^-$	Tau neutrino	$\nu_\tau$	Top	$t$	Bottom	$b$

Three 'generations' [bracketed on the left of the Leptons and Quarks table]

Increasing mass [arrow pointing down on the right of the Leptons and Quarks table]

**Figure 1.3:** The elementary matter particles and force carrier particles in the SM [2].

### 1.1.3 The Hadrons

Each matter particle has an antimatter equivalent, which has the same mass but opposite charge. The antiparticle of an electron  $e^-$  is a positron  $e^+$ . The antiparticle of a quark is represented by a bar over the letter, for example, the antiparticle of the  $u$  quark is  $\bar{u}$ . Quarks and antiquarks form composite particles called hadrons. Hadrons

are subdivided into mesons and baryons, where mesons are quark-antiquark states, such as pions, and baryons are three quark states, such as protons and neutrons. All hadrons are color singlets formed from either color - anticolor states (mesons) or three color states (baryons). Figure 1.4 gives a few examples of mesons and baryons.

### **1.1.4 The Higgs Boson**

The SM is a quantum field theory, where fields, such as the electric and magnetic fields, are basic ingredients. The energy quanta of the fields are measured as elementary particles in the laboratory. For example, the photon is the quantum of the electromagnetic field. In the SM, particles interact with a scalar Higgs field, where the strength of the interactions determines the mass of the particles. The scalar Higgs bosons are spin zero particles. There will be at least one new particle associated with the Higgs field, the Higgs boson.

## **1.2 The SM Electroweak Theory**

One of the primary goals of physics is to understand nature in a simple and unified way, in terms of a few simple principles. To a remarkable degree, the theory of elementary particle interactions can be understood as consequences of symmetry principles of nature. For example, taking a local gauge symmetry as a fundamental principle leads to the determination of the interaction of the electromagnetic field. “Local” means the symmetry transformation may vary from point to point in space-time. A local gauge symmetry requires the existence of a massless vector field.

In a field theory with a global symmetry, when the symmetry is spontaneously broken, the field acquires a vacuum expectation value and the symmetry of the theory



<b>Baryons <math>qqq</math> and Antibaryons</b> Baryons are fermionic hadrons. There are about 120 type of baryons.				
Symbol	Name	Quark content	Electric charge	Mass $\text{GeV}/c^2$
<b>p</b>	proton	<b>uud</b>	1	0.938
<b><math>\bar{p}</math></b>	anti-proton	<b><math>\bar{u}\bar{u}\bar{d}</math></b>	-1	0.938
<b>n</b>	neutron	<b>udd</b>	0	0.940
<b><math>\Lambda</math></b>	lambda	<b>uds</b>	0	1.116
<b><math>\Omega^-</math></b>	omega	<b>sss</b>	-1	1.672

<b>Mesons <math>q\bar{q}</math></b> Mesons are bosonic hadrons. There are about 140 type of mesons.				
Symbol	Name	Quark content	Electric charge	Mass $\text{GeV}/c^2$
<b><math>\pi^+</math></b>	pion	<b><math>u\bar{d}</math></b>	+1	0.140
<b><math>K^-</math></b>	kaon	<b><math>s\bar{u}</math></b>	-1	0.494
<b><math>\rho^+</math></b>	rho	<b><math>u\bar{d}</math></b>	+1	0.770
<b><math>B^0</math></b>	B-zero	<b><math>d\bar{b}</math></b>	0	5.279
<b><math>\eta_c</math></b>	eta-c	<b><math>c\bar{c}</math></b>	0	2.980

Figure 1.4: Baryons and mesons. [3].

is no longer apparent. “Global” means the symmetry transformations do not depend on position in space-time. It can be shown that the theory must contain a massless particle for every spontaneously broken continuous symmetry [4]. This is known as *Goldstone’s theorem*, and the massless particles are called *Goldstone bosons* [4].

If both local gauge symmetry and spontaneous symmetry breaking are included in the same theory, the spontaneous symmetry breaking generates a mass for the gauge boson. This mechanism is called the *Higgs mechanism*. The scalar field that causes spontaneous breaking of the gauge symmetry is known as the *Higgs field*, and the field boson is called the *Higgs boson*.

A  $U(1)$  gauge symmetry, which performs a simple phase change, can be viewed as a multiplication of a  $1 \times 1$  unitarity matrix.  $SU(2)$  means the transformations are  $2 \times 2$  unitary matrices, which are “special” matrices with determinant unity. In a theory with  $SU(2) \times U(1)$  symmetry, there are four gauge boson fields. The Higgs mechanism generates one massless and three massive gauge bosons. These vector bosons are the  $\gamma$ ,  $Z^0$  and  $W^\pm$ , the mediators of the electroweak interaction. This theory is known as the *Glashow-Weinberg-Salam Electroweak theory*. S. Glashow, S. Weinberg, and A. Salam shared the 1979 Nobel Prize in physics for their contributions to the theory of the unified weak and electromagnetic interaction between elementary particles. The theory makes precise predictions for the couplings of vector bosons to fermions and the self-couplings between the gauge bosons.. A more detailed discussion of the Glashow-Weinberg-Salam Electroweak theory is given in Appendix A.

### 1.3 The SM Quantum Chromodynamics Theory

The strong interaction is described by a gauge theory, known as quantum chromodynamics (QCD). It is a gauge theory of the symmetry group  $SU(3)$ . Each of the

quarks comes in three different color charges (as opposed to the electric charge in the electroweak interaction). The gauge bosons of the color interactions, carry the strong color quantum number and form an octet of bi-colored gluons (the gluon carries a unit of color and a unit of anti-color). Therefore the gluon, unlike the photon, interacts with itself. No free quarks or free gluons have been observed experimentally. Quarks and gluons are confined within composite particles (hadrons). The strength of the strong interactions decreases with increasing momentum transfer (or decreasing distance), and vanishes asymptotically. Quarks behave as free particles at extremely high energies. This is referred to as *asymptotic freedom*, which was discovered in 1973 by David Gross, Frank Wilczek and David Politzer. They shared the Nobel Prize in Physics for 2004 for the discovery of asymptotic freedom in the theory of the strong interaction.

## 1.4 Terminology in Particle Physics

**Table 1.1:** Units in high energy physics [5].

Quantity	High Energy Unit	Value in SI units
length	1 fm	$10^{-15}$ m
time	1 ns	$10^{-9}$ s
energy	1 GeV = $10^9$ eV	$1.602 \times 10^{-10}$ J
mass	1 GeV/ $c^2$	$1.78 \times 10^{-27}$ kg

In particle physics, high energy accelerators are built to probe the structure of particles with typical sizes of  $10^{-15}$  meter and masses of  $10^{-27}$  kilogram. The basic units, such as meters, kilograms and seconds, are not very convenient in particle physics. The units commonly used are summarized in Table 1.1. The unit of length is the fm (femtometre, which equals  $10^{-15}$  m). The unit of energy is the GeV, which

equals  $10^9$  eV (electron volt). One electron volt is the energy an electron gains when passing through an electrostatic potential difference of one volt. The mass of a particle is commonly quoted in units of  $\text{GeV}/c^2$ . In calculations, the speed of light  $c$  is commonly set to 1, and the unit of mass becomes the GeV. Using this convention, the mass of proton is 0.938 GeV. The relations between the following energy units are:

$$1 \text{ MeV} = 10^6 \text{ eV}, \quad 1 \text{ GeV} = 10^3 \text{ MeV}, \quad 1 \text{ TeV} = 10^3 \text{ GeV}. \quad (1.1)$$

For example, the center-of-mass energy of the Tevatron proton-antiproton ( $p\bar{p}$ ) collider at Fermilab is  $\sqrt{s} = 1.96 \text{ TeV} = 1960 \text{ GeV}$ .

The reaction rate in a collider is given by

$$R = \sigma \mathcal{L} \quad (1.2)$$

where  $\sigma$  is the interaction cross section,  $\mathcal{L}$  is the luminosity and  $R$  is the number of events produced per second. The unit of cross section is the barn, where  $1 \text{ b} = 10^{-24} \text{ cm}^2$ . The cross sectional area of a uranium nucleus is roughly equal to 1 barn. The term “barn” originally developed during World War II, when nuclear physicists were bouncing neutrons off uranium nuclei, which they described as being “big as a barn”. The relations between the following cross section units are:

$$1 \text{ b} = 10^{-24} \text{ cm}^2, \quad 1 \text{ pb} = 10^{-12} \text{ b}, \quad 1 \text{ fb} = 10^{-3} \text{ pb}. \quad (1.3)$$

The unit of luminosity  $\mathcal{L}$  is  $\text{cm}^{-2}\text{s}^{-1}$ . A typical luminosity value for the Tevatron  $p\bar{p}$  collider is  $10^{32} \text{ cm}^{-2}\text{s}^{-1}$ . Integrated luminosity is the integral of luminosity over time (in  $\text{cm}^{-2}$ ). The commonly used unit of integrated luminosity is  $\text{fb}^{-1}$ , where  $1 \text{ fb}^{-1} = 10^{39} \text{ cm}^{-2}$ . This analysis uses an integrated luminosity of  $1.1 \text{ fb}^{-1}$  of data.

## 1.5 Thesis Overview

In the following chapters, a measurement of  $p\bar{p} \rightarrow e^+e^-\gamma + X$  production is described. An experimental overview of gauge boson measurements is given in Chapter 2. The Fermilab Tevatron and the Collider Detector at Fermilab are described in Chapter 3 and 4 respectively. A theoretical overview of diboson physics is given in Chapter 5. Chapter 6 gives a description of the selection of an inclusive Z boson sample. The cross section measurement of the inclusive Z production is presented in Chapter 7. The photon selection and background study are described in Chapter 8. The selection of  $ee\gamma$  events and the measured cross section of  $p\bar{p} \rightarrow e^+e^-\gamma + X$  production are presented in Chapter 9. Finally, limits on anomalous neutral gauge couplings are given in Chapter 10.

## Chapter 2

# Experimental Overview of Gauge Boson Measurements

An experimental overview of gauge boson measurements is given in this chapter. Experimental verifications of the SM electroweak theory are presented in Section 2.1. In Section 2.2 we discuss the motivation for the studies of gauge boson pair production. In Section 2.3, we summarize gauge boson measurements at the Large Electron-Positron Collider at CERN and the Tevatron Proton-Antiproton collider at Fermilab.

## 2.1 Experimental Verifications of the SM Electroweak Theory

### 2.1.1 Observations of Charged and Neutral Currents

The SM electroweak theory describes the coupling of  $W$  and  $Z$  vector bosons to fermions, and predicts observable effects in processes mediated by weak bosons. At energies lower than the vector boson masses, these couplings have effects through virtual weak boson exchange processes. Figure 2.1 shows an example of a charged current involving a virtual  $W$  boson decay. Figure 2.2 is an example of a neutral current involving a virtual  $Z$  boson exchange. In 1973, the CERN Gargamelle [6] bubble chamber at CERN photographed the tracks of a few electrons suddenly starting to move, seemingly of their own accord. This was interpreted as a neutrino interacting with the electron by the exchange of an unseen  $Z$  boson. The discovery of neutral-current events in 1973 was important in providing evidence in favor of the

Glashow-Weinberg-Salam electroweak theory.

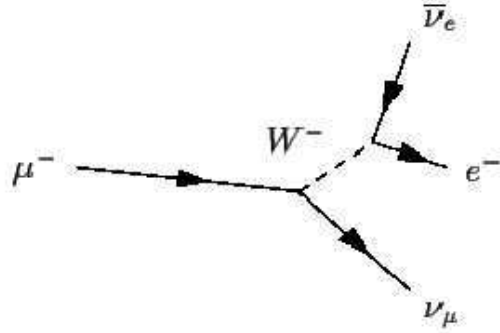


**Figure 2.1:** An example of a charged current.

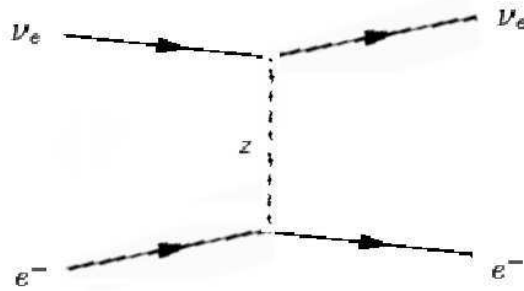


**Figure 2.2:** An example of a neutral current.

### 2.1.2 The Discovery of the W and Z Bosons at CERN

Further tests of the Glashow-Weinberg-Salam Electroweak theory are available at higher energies. In January 1983, the UA1 and UA2 collaborations at the CERN Super Proton Synchrotron (SPS) pp collider discovered the W boson [7, 8]. A few months later, The UA1 collaboration published the paper, “Experimental Observation of Lepton Pairs of Invariant Mass Around 95 GeV/c<sup>2</sup> at the CERN SPS Collider” [9], which provided the first evidence for the neutral intermediate Z boson. The No-

bel Prize in Physics 1984 was awarded to Carlo Rubbia and Simon van der Meer, “for their decisive contributions to the large project, which led to the discovery of the field particles W and Z, communicators of weak interaction” [10].

### 2.1.3 The Search for the Higgs Boson

The SM has been very successful in describing the strong, weak and electromagnetic interactions. However, the final building block in the SM, the Higgs boson, has not yet been discovered experimentally. The mass of the Higgs boson, which is not theoretically predicted, remains unknown. One of the primary goals of current and future collider experiments is to discover the Higgs boson and study its properties.

The coupling of the Higgs to fermions is  $m_f/v$  and  $M_g^2/v$  to weak gauge bosons. Here  $m_f$  and  $M_g$  are fermion mass and W or Z masses, respectively, and  $v$  is the vacuum expectation value of the Higgs field. The Higgs field has a vacuum expectation value of 246 GeV. If the mass of the Higgs boson were known, its decay pattern is then fixed by SM electroweak theory.

At the Large Electron-Positron Collider (LEP), the Higgs search is performed in the process:

$$e^+ + e^- \rightarrow Z^{0*} \rightarrow Z^0 + H. \quad (2.1)$$

For Higgs boson accessible at LEP energies, they decay primarily into pairs of b quarks. No Higgs is seen with a mass below  $114 \text{ GeV}/c^2$ .

If  $m_H > 2m_W$ , the Higgs boson can decay to  $W^+W^-$ ; if  $m_H > 2m_Z$ , it can also decay to  $ZZ$ . Once the decay channel into boson pairs opens, most of the Higgs will decay to boson pairs. There are searches for the Higgs boson in the WH and ZH associated production channels with  $H \rightarrow bb$ , and gluon fusion single Higgs production with  $H \rightarrow WW$  at the Collider Detector at Fermilab (CDF) and D0 experiments at the Tevatron [11]. The two experiments will soon be excluding Higgs bosons with mass around  $160 \text{ GeV}/c^2$  (assuming it is not there).



## 2.2 Motivation for the Studies of Gauge Boson Pairs

Electroweak theory makes precise predictions for the couplings between gauge bosons. Vector boson pair production provides direct tests of the triple gauge boson couplings. The possible trilinear couplings involving the electroweak gauge bosons  $W$ ,  $Z$  and  $\gamma$  are the  $WW\gamma$ ,  $WWZ$ ,  $ZZZ$ ,  $ZZ\gamma$  and  $Z\gamma\gamma$  couplings. Only the  $WW\gamma$  and  $WWZ$  couplings are allowed in the Standard Model, whereas the neutral trilinear couplings  $ZZZ$ ,  $ZZ\gamma$ , and  $Z\gamma\gamma$  are all zero at tree level (the lowest-order Feynman diagrams). The measurement of gauge boson pair production and the anomalous self-couplings provide an important test of the electroweak gauge theory in the Standard Model. Any deviation will provide important information about new physics beyond the Standard Model.

In the search for the Higgs boson with  $m_H > 2m_W$  at the Tevatron, the largest background is boson pair production. Thus good measurement of boson pair production is crucial step to discover and precisely measure the Higgs boson.

## 2.3 Gauge Boson Measurements

In this section we summarize the measurement of gauge bosons at the Large Electron-Positron Collider at CERN and at the Tevatron  $p\bar{p}$  collider at Fermilab.

### 2.3.1 At the $e^+e^-$ Collider at CERN

In this section we summarize the results of gauge boson measurements at the Large Electron-Positron Collider (LEP) [12].

## Z Boson Properties , the Number of Neutrino Species

The Large Electron Positron Collider was run at the Z mass energy from 1990 to 1995.

Z boson properties, such as mass, width and decay branching ratios were measured.

The measured mass and width of the Z boson are:

$$m_Z = 91.1876 \pm 0.0021 \text{ GeV}/c^2 \quad (2.2)$$

$$\Gamma_Z = 2.4952 \pm 0.0023 \text{ GeV}/c^2. \quad (2.3)$$

The measured leptonic decay branching ratio is

$$Br(Z \rightarrow ll) = 0.033658 \pm 0.000023, \text{ where } l = e, \mu \text{ or } \tau. \quad (2.4)$$

The measurements of Z decays into "invisible channels" gives important information about the number of neutrino species. The partial decay widths of the Z boson are determined as

$$\Gamma_{inv}/\Gamma_l = 5.942 \pm 0.016,$$

where  $\Gamma_{inv}$  is the Z decay width into invisible particles and  $\Gamma_l$  is the leptonic Z decay width. In the case of lepton universality (universality of the couplings of leptons to the photon, W and Z bosons), the Standard Model value for the partial widths to neutrinos and charged leptons is

$$\Gamma_{\nu\nu}/\Gamma_l = 1.9912.$$

From the ratio of the two expressions above, the number of light neutrino species is measured to be

$$N_\nu = \Gamma_{inv}/\Gamma_{\nu\nu} = 2.9841. \pm 0.0083.$$

## W-Boson Mass and Width at LEP-II

After 1996 LEP ran at energies above the W-pair production threshold.  $10 \text{ pb}^{-1}$  of data were taken close to the  $W^+W^-$  pair production threshold at  $\sqrt{s} = 161 \text{ GeV}$ . The  $W^+W^-$  cross section is sensitive to the W boson mass at the threshold energy. Based on these data, the W mass was measured from the  $W^+W^-$  threshold cross section.

Later, the LEP  $e^+e^-$  collider operated at energies over a range of center-of-mass energies,  $\sqrt{s} = 172 - 209 \text{ GeV}$ . For these data, the W mass was measured by the direct reconstruction of invariant mass of the W bosons from their decay products.

The LEP-combined results on the mass and width of the W boson are:

$$m_W = 80.447 \pm 0.042 \text{ GeV}/c^2 \quad (2.5)$$

$$\Gamma_W = 2.150 \pm 0.091 \text{ GeV}/c^2. \quad (2.6)$$

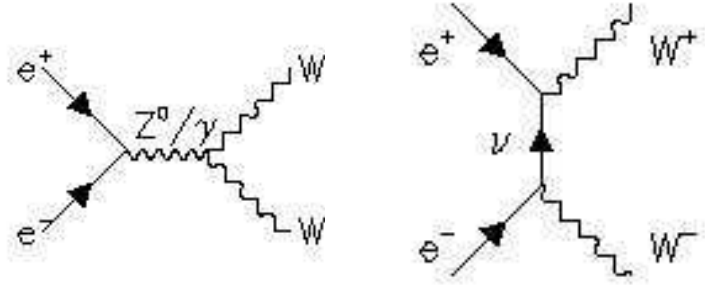


**Figure 2.3:** W-pair production.

## Gauge Boson couplings

The W-pair production process (see Figure 2.3), involves triple gauge boson vertices  $WWZ$  and  $WW\gamma$ . During LEP II operation, about 10,000 W-pair events were

collected by each experiment. W-pair production cross-sections are measured for center-of-mass energies from 161 to 189 GeV. Z-pair production cross-sections are measured for center-of-mass energies from 183 to 207 GeV(see Figure 2.4). There is no significant deviation from the Standard Model prediction for any of the electroweak gauge boson couplings studied. The LEP data experimentally verified the existence of triple gauge boson couplings among the electroweak gauge bosons.

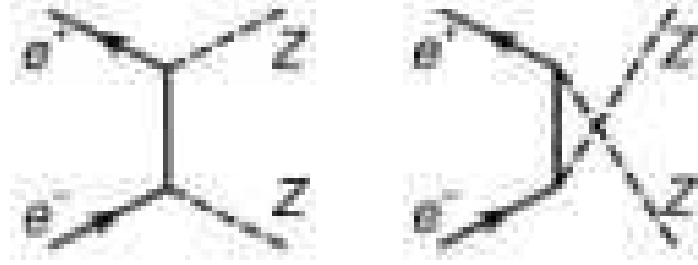


**Figure 2.4:** Z-pair production.

### 2.3.2 At the Tevatron $p\bar{p}$ Collider at $\sqrt{s} = 1.96$ TeV

In this section we summarize the results of gauge boson measurements at the Tevatron  $p\bar{p}$  Collider at  $\sqrt{s} = 1.96$  TeV.

#### **Inclusive W and Z cross sections, W mass and width**

Inclusive W and Z cross sections are measured from  $p\bar{p}$  collisions at  $\sqrt{s} = 1.96$  TeV at the Collider Detector at Fermilab(CDF) [13]. The resulting cross section times the branching ratio is:

$$\sigma(p\bar{p} \rightarrow W + X) \times Br(W \rightarrow lv) = 2.749 \pm 0.174 \text{ nb}, \quad (2.7)$$

$$\sigma(p\bar{p} \rightarrow Z/\gamma^* + X) \times Br(Z/\gamma^* \rightarrow ll) = 254.9 \pm 16.2 \text{ pb}. \quad (2.8)$$

The ratio of W and Z boson cross section can be written as:

$$R = \frac{\sigma(p\bar{p} \rightarrow W + X) \times Br(W \rightarrow lv)}{\sigma(p\bar{p} \rightarrow Z + X) \times Br(Z \rightarrow ll)} = \frac{\sigma(p\bar{p} \rightarrow W + X) \times \Gamma(W \rightarrow lv) \times \Gamma(Z)}{\sigma(p\bar{p} \rightarrow Z + X) \times \Gamma(Z \rightarrow ll) \times \Gamma(W)}. \quad (2.9)$$

The W branching ratio to lepton neutrino can be extracted from Equation 2.9 using the measured cross section ratio  $R$ , the predicted ratio of W and Z production cross sections and the measured value of  $Br(Z \rightarrow ll) = \frac{\Gamma(Z \rightarrow ll)}{\Gamma(Z)}$ :

$$Br(W \rightarrow lv) = \frac{\Gamma(W \rightarrow lv)}{\Gamma(W)} = 0.1082 \pm 0.0022, \quad (2.10)$$

which can be compared to the SM prediction of  $0.1082 \pm 0.0002$ .

An indirect measurement of the total width of the W boson can be obtained from the measured value of  $Br(W \rightarrow lv)$  using the SM value for the leptonic partial width  $\Gamma(W \rightarrow lv)$ :

$$\Gamma_W = 2092 \pm 42 \text{ MeV}. \quad (2.11)$$

The SM prediction for this parameter is  $2092 \pm 3 \text{ MeV}$ .

A direct measurement of the width of the W boson has been performed based on  $350 \text{ pb}^{-1}$  of data. The width is determined by fitting the W boson transverse mass distribution tail. The width is measured to be [14]:

$$\Gamma_W = 2032 \pm 71 \text{ MeV}. \quad (2.12)$$

This CDF measurement is the world's most precise single direct measurement.

The mass of the W boson is measured in the  $W \rightarrow e\nu$  and  $W \rightarrow \mu\nu$  channels.

Based on  $200\text{ pb}^{-1}$  of data, the mass of the W boson is measured to be [15]:

$$m_W = 80413 \pm 48 \text{ MeV} \quad (2.13)$$

This CDF measurement is the most precise single measurement of the W boson mass to date.

## Boson Pair Measurements

Boson pair production cross sections have been measured at both the CDF and D0 experiments. Table 2.1 give a summary of these measurements at CDF. The ZZ measurement [16] is the first evidence for ZZ production at a hadron collider, and the WZ measurement [17] is the first observation of the associated production of a W boson and a Z boson. These measurements use the electron or muon decay channels of W and Z bosons. All measurements agree well with the Standard Model predictions.

**Table 2.1:** Measurements of diboson pair production at CDF.

Channel	Luminosity (fb <sup>-1</sup> )	Cross section (pb)
$p\bar{p} \rightarrow W^+W^- + X$ [18]	0.8	$13.6 \pm 3.0$
$p\bar{p} \rightarrow W^\pm Z + X$ [17]	1.9	$4.3 + 1.4 - 1.1$
$p\bar{p} \rightarrow ZZ + X$ [16]	1.5	$0.75 + 0.71 - 0.54$
$p\bar{p} \rightarrow W\gamma + X \rightarrow l\nu\gamma + X (l = e, \mu)$ [19] ( $E_t^\gamma > 7 \text{ GeV}$ , $\Delta R > 0.7$ )	1.1	$18.0 \pm 2.8$

## Charged Triple Anomalous Gauge Couplings

The Standard Model electroweak gauge theory makes precise predictions for couplings between the  $\gamma$ ,  $W^\pm$  and Z gauge bosons. Limits on charged anomalous gauge boson

couplings are extracted from the  $p\bar{p} \rightarrow WZ + X$  measurement; Table 2.2 shows the limits on the WWZ anomalous couplings. Details on these coupling parameters are given in Chapter 5.

**Table 2.2:** WWZ anomalous couplings limits at 95% C.L from  $p\bar{p} \rightarrow WZ + X$  measurement based on  $1.9 \text{ fb}^{-1}$  of data at CDF [17].

Couplings	$\Lambda = 2.0 \text{ TeV}$
$\lambda$	-0.13, 0.14
$\Delta g$	-0.15, 0.24
$\Delta \kappa$	-0.82, 1.27

### Neutral Triple Anomalous Gauge Couplings

There are no neutral triple gauge couplings in the Standard Model at tree level (see Section 5.1). Any observed anomalous couplings will provide important information about new physics beyond the Standard Model.

This thesis presents measurements of the  $Z\gamma$  production cross section and a search for anomalous couplings at the  $ZZ\gamma$  and  $Z\gamma\gamma$  vertices. The current published limits on these couplings are summarized in Table 2.3. Details on these coupling parameters are given in Chapter 5.

**Table 2.3:** 95% C.L. limits on  $Z\gamma$  anomalous couplings.

Experiment Luminosity( $\text{fb}^{-1}$ )	CDF Run I [20] 0.02	LEP II [12] 0.7	D0 [21] 1.1
$h_3^Z$	-3.0, 2.9	-0.20, 0.07	-0.083, 0.082
$h_4^Z$	-0.7, 0.7	-0.05, 0.12	-0.005, 0.005
$h_3^\gamma$	-3.1, 3.1	-0.049, 0.008	-0.085, 0.084
$h_4^\gamma$	-0.8, 0.8	-0.02, 0.034	-0.005, 0.005

## Chapter 3

### The Tevatron Collider at Fermilab

The Tevatron Collider at Fermilab produces  $p\bar{p}$  collisions at a center of mass energy of 1.96 TeV. It consists of a number of different accelerator systems including the Proton Source, the Antiproton Source, the Main Injector and the Tevatron. Figure 3.1 gives an overview of the accelerator complex. A brief description of each of the systems is given in section 3.2. The Tevatron operation status is discussed in section 3.3.

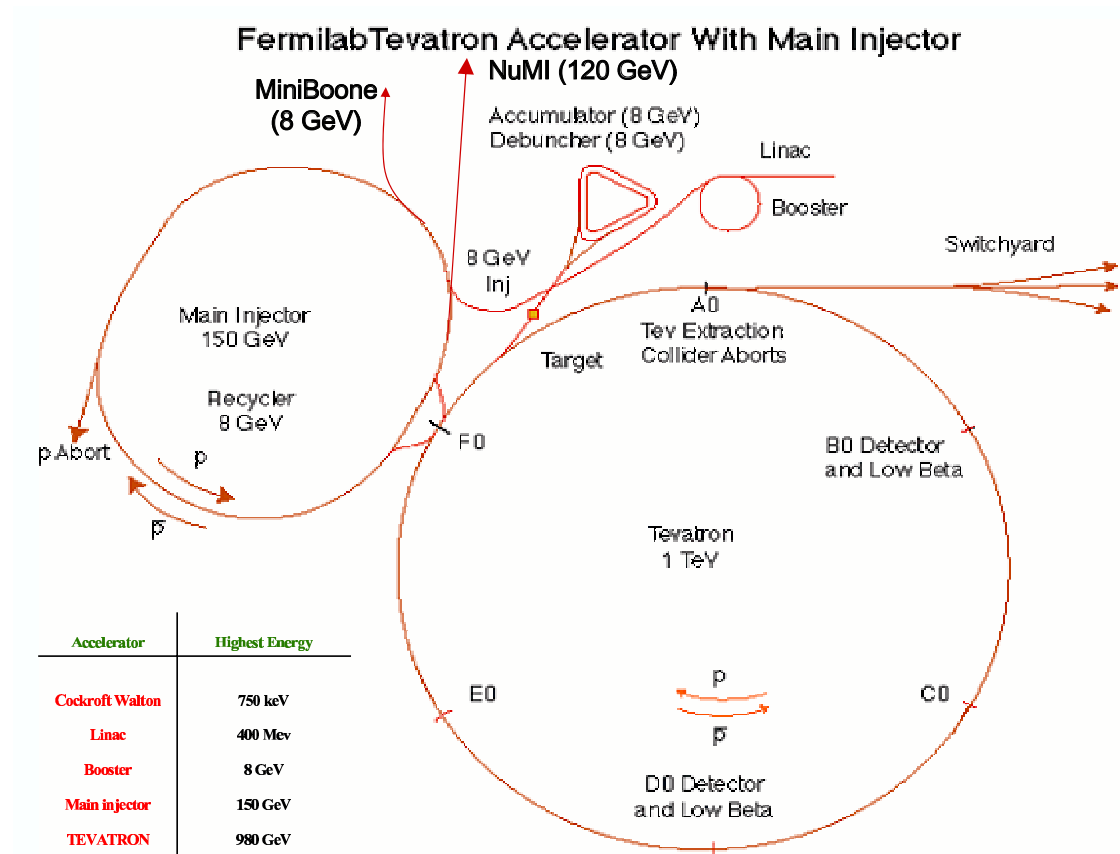
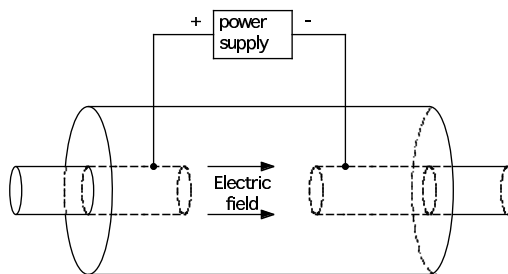


Figure 3.1: Accelerator Complex Overview [22].



### 3.1 Introduction

Electric fields are used to accelerate charged particles. A charged particle gains an energy of  $\Delta E = q\Delta V$  when passing through a static electric field where  $q$  is the particle charge and  $\Delta V$  is the potential difference of the field. To obtain high energy, a high potential gradient is needed. But if the electric field is too large, an electrical break down will occur which will cause an electric spark (and possibly an electric arc) and lead to the dropping of the potential gradient. To avoid the electrical breakdown, it is necessary to use moderate electric fields many times in a row and build up the particle's kinematic energy incrementally. A Radio Frequency(RF) cavity, shown in figure 3.2, is a structure for such a purpose. A RF cavity is essentially a gap cut into a beam pipe where an electrical field is created. When the charged particle travels through the gap, it is accelerated by the electrical field and gains energy. By placing a number of these gaps in a row, the charged particle can be accelerated to a desired energy.



**Figure 3.2:** A Radio Frequency(RF) cavity [23].

A RF cavity uses electromagnetic waves. Figure 3.3 shows a simplified example of the cavity fields vectors in the Drift Tube Linac (see section 3.2.1). The electric field is along the beam pipe and is perpendicular to the magnetic field. A positive charged beam will be accelerated when the electric field is parallel to the beam direction.

When the electric field reverses the beam must be shielded in the tubes.

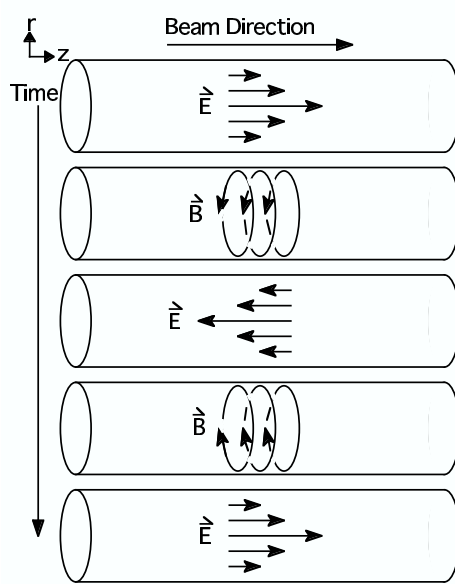


**Figure 3.3:** A Radio Frequency(RF) cavity [24].

A RF cavity also keeps the beam in bunch (discrete packets of particles, rather than a continuous stream) longitudinally, as illustrated in figure 3.4. Particles with higher energy will arrive earlier in time. These particles will get a smaller kick and slip back. Particles with lower energy will arrive later in time and they will get a larger kick and catch up.

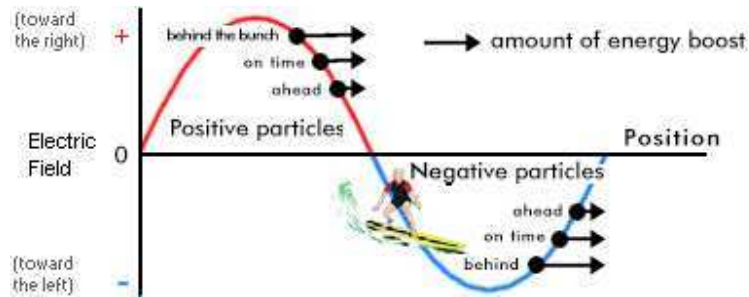


**Figure 3.4:** A radio frequency accelerator [25].

There are two basic designs for a particle accelerator: linear (linac) and circular

(synchrotron). In linacs, particles are accelerated in a single pass. In synchrotrons, particles are accelerated over many revolutions. The Fermilab Tevatron accelerator system consists of one linac and six synchrotrons

### 3.1.1 Synchrotron

In synchrotrons, magnets are used to keep the particles in a circular orbit. For a proton of momentum  $P$  (in  $\text{GeV}/c$ ), the magnetic field must have a value of  $B$  (in Tesla), where

$$B = \frac{P}{0.3\rho} \quad (3.1)$$

and  $\rho$  (in meters) is the radius of the circle. The magnetic field must be normal to the plane of the orbit (see figure 3.5). RF cavities accelerate the particles. The magnetic field changes with time while the radius of the circle remains constant. Both the magnetic field and the RF frequency must be synchronized to the beam momentum.

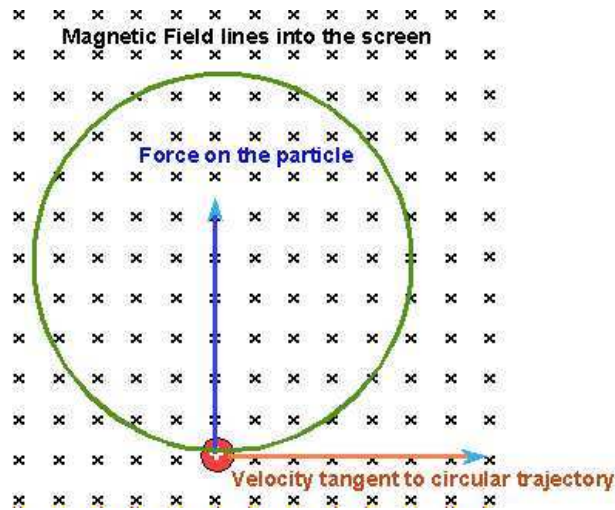


Figure 3.5: The magnetic force [26].

## 3.2 The Fermilab Tevatron Accelerator System

The individual components in the Tevatron accelerator system are discussed in this section.

### 3.2.1 The Proton Source

The Proton Source consists of the following accelerator systems: the Pre-accelerator, Linac and Booster.

1. The Pre-accelerator:

In the proton source, hydrogen gas is converted to  $H^-$  ions. The Pre-accelerator, a Cockcroft-Walton generator, creates a large static electric field. The pre-accelerator dome is charged to a potential of -750 kV and the wall of the pre-accelerator pit is kept at ground potential. The  $H^-$  ions are accelerated from the charged dome to the ground wall obtaining a kinetic energy of 750 KeV.

2. The Linac (linear accelerator) :

The Linac, of length 145 meter long, accelerates the ions to 400 MeV. RF power generates an electric field (see figure 3.6). Particles are accelerated in the gaps, and shielded in the interior of the tubes when the electric field reverses. Gaps are spaced further apart as particle speed increases. The beam emerging from the Linac will be accelerated and bunched.

3. The Booster

The Booster is 75 meters in radius , and the first synchrotron (see section 3.1.1) in the accelerator complex. The electrons are stripped off the  $H^-$  ions, and the bare protons are accelerated to 8 GeV.

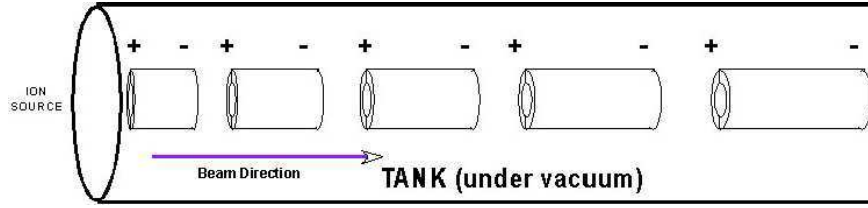


**Figure 3.6:** The Linac drift tube [27].

### 3.2.2 The Main Injector

The Main Injector is a synchrotron with a circumference about seven times that of the Booster. It has 18 RF accelerating cavities. It accelerates 8 GeV protons from the Booster to 150 GeV before injecting them into the Tevatron. A second function of the Main Injector is to accelerate 8 GeV antiprotons (from either the Accumulator or the Recycler, see section 3.2.3) to 150 GeV before injecting them into the Tevatron. A third function of the Main Injector is to accelerate 8 GeV protons from the Booster to 120 GeV, sending them to the anti-proton source target station.

### 3.2.3 The Anti-Proton Source

The Fermilab Tevatron is a proton-antiproton collider. Since the proton and antiproton will travel in the opposite directions through the magnets, a proton-antiproton collider can be built with one ring of magnets instead of two.

Unlike protons, there is no bottled anti-proton source available. The anti-proton production system consists of the following three major components: the Target Station, the Debuncher and the Accumulator.

- The Target Station (see Figure 3.7):

A beam of 120 GeV proton from the Main Injector strikes a Nickel target and produces a shower of secondary particles. A Lithium lens is used to focus the

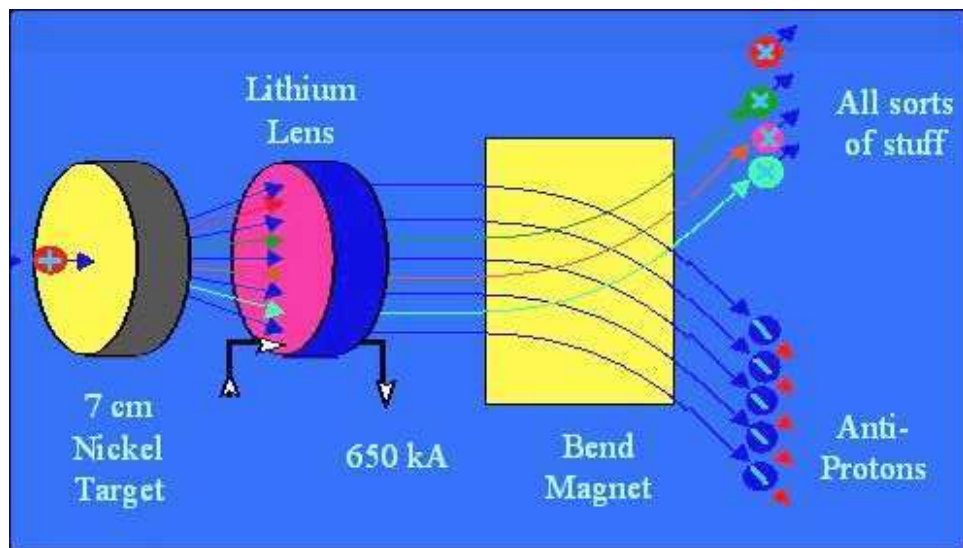


**Figure 3.7:** Fermilab anti-proton target station [28].

negative secondary particles coming out of the target. A dipole magnet, acting as a charge-mass spectrometer, selects 8 GeV anti-protons and sends them to the Debuncher. The process is very inefficient; for every 1 million protons striking the target, only about twenty 8 GeV anti-protons are collected and stored.

- The Debuncher:

The anti-protons from the target will have a very large momentum spread due to the different details of the collision process. The Debuncher, an 8 GeV synchrotron, is used to reduce the beam size and the momentum spread of the anti-proton beam.

- The Accumulator:

The Accumulator, as its name suggests, is used to accumulate anti-protons. It accumulates 8 GeV anti-protons by stacking successive pulses from the Debuncher.

Both the Debuncher and the Accumulator use Stochastic Cooling to reduce the beam

size. The Stochastic Cooling process is illustrated in figure 3.8. A particle oscillates around an ideal orbit. The cooling system uses feedback to damp the amplitude of this oscillation. A pickup electrode measures the “error” signal of the particle’s position. The “error” signal is amplified and its opposite is applied to kicker electrodes which move the particle back to the ideal orbit.

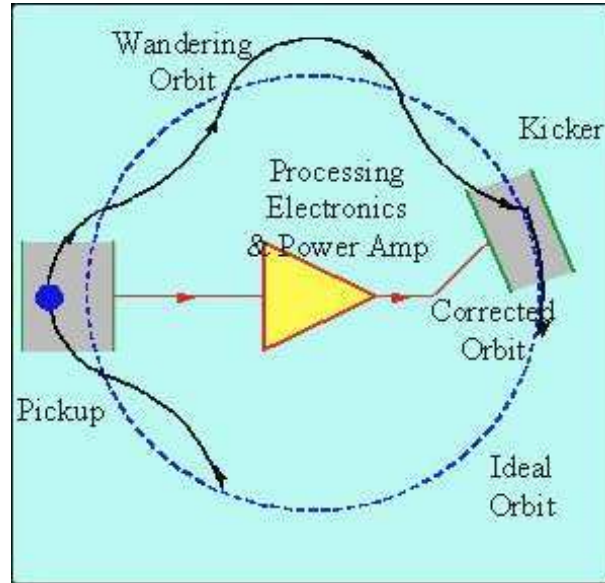


**Figure 3.8:** The Stochastic Cooling System [28].

### 3.2.4 The Recycler

The Recycler ring is an anti-proton storage ring with permanent magnets. It is located above the Main Injector. Anti-protons are extracted from the Accumulator and stored in the Recycler ring for many hours. The Recycler “cools” the anti-protons by reducing the longitudinal and transverse spread of the beam. This will provide the Tevatron Collider with a high intensity anti-proton beam.

### 3.2.5 The Tevatron

The Tevatron is the world's highest energy collider (before the Large Hadron Collider at CERN turns on). It is a superconducting synchrotron, with a radius of 1 km, about 4 miles in circumference. Using liquid helium, all the magnets are cooled to 4.6 K, where they become superconducting. The 150 GeV protons and anti-protons beams from the Main Injector are accelerated to 980 GeV and focused to collide at the CDF and D0 detectors. At 980 GeV, the superconducting magnetic field is 4.2 Tesla. There are 36 bunches of protons and 36 bunches of anti-protons circulating in the Tevatron. The  $p\bar{p}$  collisions occur every 396 ns.

Table 3.1 summarizes the accelerator systems at Fermilab.

**Table 3.1:** A summary of the Tevatron accelerator systems.

Machine	Type	Particle	Energy
Proton Source		$H^-$	25 KeV
Preacc	Cockcroft-Walton	$H^-$	750 KeV
Linac	linear accelerator	$H^-$	400 MeV
Booster	synchrotron	Proton	8 GeV
Debuncher	synchrotron	Anti-Proton	8 GeV
Accumulator	synchrotron	Anti-Proton	8 GeV
Recycler	synchrotron	Anti-Proton	8 GeV
Main Injector	synchrotron	Proton, Anti-Proton	150 GeV
Tevatron	synchrotron	Proton, Anti-Proton	980 GeV

## 3.3 Tevatron Luminosity

The collision rate is calculated as the product of the interaction cross-section and the luminosity (see Equation 1.2). The formula for luminosity is

$$\mathcal{L} = f n \frac{N_1 N_2}{A} \quad (3.2)$$



where  $f$  is the collision frequency,  $n$  is the number of bunches in either beam,  $N_1$  and  $N_2$  are the number of particles in each bunch and  $A$  is the cross-sectional area of the beams. The unit of luminosity is  $cm^{-2}s^{-1}$ . At the Tevatron, each beam has 36 bunches. For a typical store, the number of protons per bunch is  $2.7 \times 10^{11}$  and the number of antiprotons is  $7.0 \times 10^{10}$ , which gives a luminosity of  $2 \times 10^{32} cm^{-2}s^{-1}$  [29]. For an interaction cross section of 1 pb ( $1 pb = 10^{-12} \text{ barn} = 10^{-36} cm^2$ ), the collision rate is 0.7 events per hour. The Tevatron record (as of Feb 2007) for initial luminosity is  $2.8 \times 10^{32} cm^{-2}s^{-1}$ . The weekly integrated luminosity record is  $45 pb^{-1}$ . Figure 3.9 summarizes Run II Tevatron integrated luminosity. The total CDF data on tape is  $\approx 3 fb^{-1}$ . Figure 3.10 is the 2006 Tevatron integrated luminosity projection. With an anti-proton production rate of 30 mA/hr, Tevatron will deliver a total luminosity of  $8 fb^{-1}$  by the end of 2009.

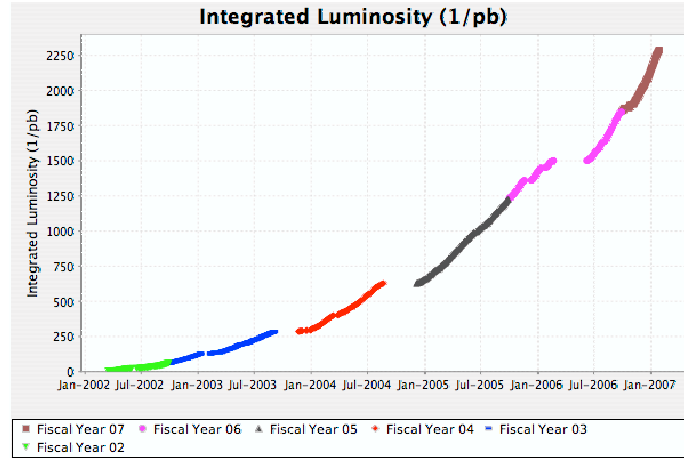


**Figure 3.9:** Run II Tevatron luminosity summary [30].

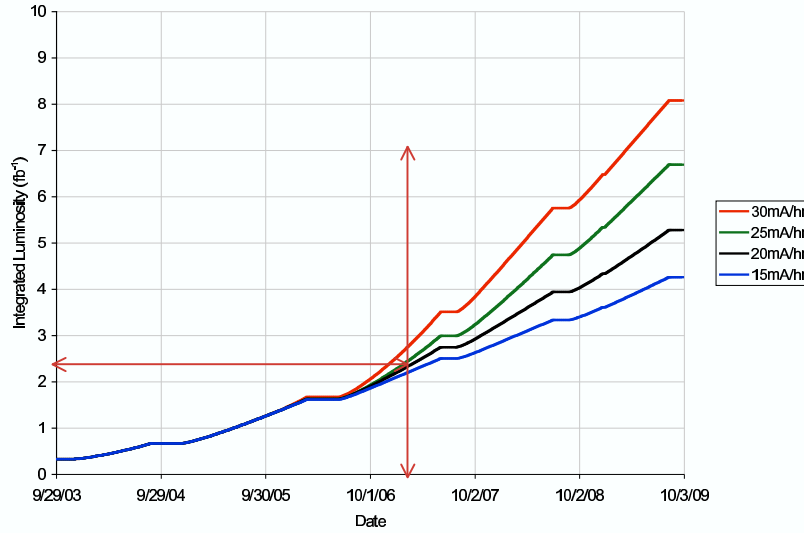


**Figure 3.10:** 2006 Tevatron luminosity projection curves [30].

## 3.4 Discoveries at Fermilab

In this section, we briefly review the discoveries of two fundamental particles at Fermilab.

### 3.4.1 The discovery of the bottom quark (1977)

In June 1977, the E288 experiment at Fermilab discovered the “upsilon” particle, which is a composite of a bottom quark with an anti-bottom quark. This discovery revealed the third generation of quarks.

The Tevatron is a factory for production of bottom quarks. Studies of particles containing the bottom quark are performed at the CDF and D0 experiments. These measurements provide information about the property of hadrons containing the bottom quarks, such as the mass, lifetime and particle - antiparticle mixing.

### 3.4.2 The discovery of the top quark (1995)

After the bottom quark was discovered in 1977, a decades-long search for its partner, the top quark, was carried out in experiments worldwide. The top quark mass was first estimated to be in the range of 5 - 65 GeV [31]. But experiments in the 1980's found nothing in this mass range. In 1990, a lower limit of top quark mass was set at  $M_t > 91 \text{ GeV}/c^2$  since top quarks were not seen in the decays of the W and Z bosons. The CDF and the D0 experiments at the Tevatron announced the discovery of the top quark in March 1995. The top quark turns out to be very heavy with a mass of  $175 \text{ GeV}/c^2$ , as heavy as a gold atom.

## 3.5 Chapter Summary

The Fermilab Tevatron provides proton-antiproton collisions at a center of mass energy of 1.96 TeV, the world's highest energy before the LHC turns on in 2008. As of January 2008, it has delivered an integrated luminosity of  $\approx 3.4 \text{ fb}^{-1}$  of data to the CDF and D0 experiments. In the next chapter, the Collider Detector at Fermilab (CDF), located at one of the collision points, is described.

# Chapter 4

## The CDF Experiment

In this chapter, we describe the detection of particles in high energy collisions. Section 4.1 gives a brief introduction to particle detection, Section 4.2 and 4.3 describe the CDF detector and the data acquisition systems.

### 4.1 Introduction: Particle Detection

To measure particles produced in high energy collisions, a typical modern detector has the following components:

- Charged particle tracking chamber
- Electromagnetic (EM) calorimeter
- Hadron calorimeter
- Muon tracking chamber

The signatures of various particles in the detector are listed below (see Figure 4.1):

- Electrons leave a charged track and energy deposit in the EM calorimeter.
- Photons pass through the tracking chamber, and are detected in the EM calorimeter.
- Quark and gluon jets (a collimated spray of high energy hadrons) are detected in the tracking chamber, EM and hadron calorimeters.

- Muons penetrate the calorimeters and are detected in the tracking chamber and muon chamber.
- Neutrinos rarely interact with detector materials and can only be detected by an imbalance in the transverse momentum ( $\cancel{E}_t$ ).

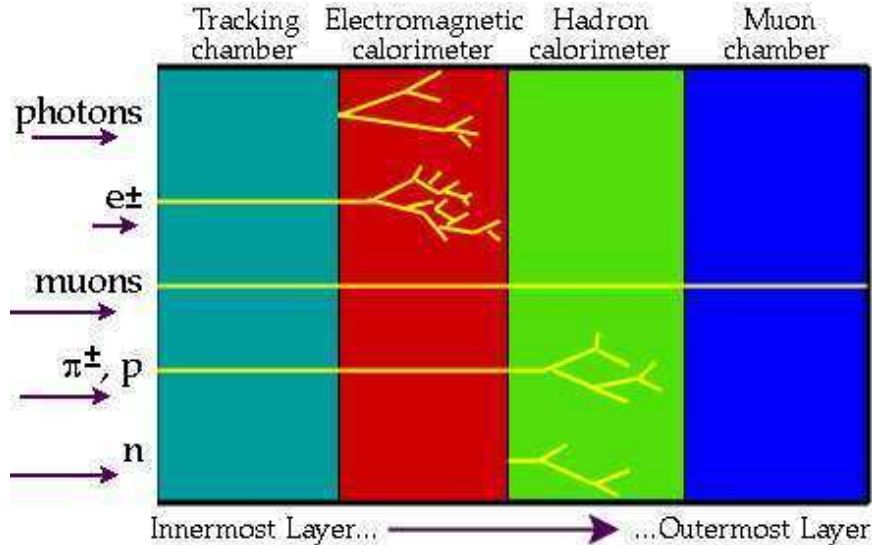


**Figure 4.1:** The interaction of various particles with the different components of a detector [32].

The basic principles of operation of particle detector are described in the following sections.

#### 4.1.1 Drift Chambers

The principle of operation of a drift chamber is illustrated in figure 4.2. When a charged particle enters a drift chamber filled with gas, it ionizes the atoms and produces electron-ion pairs. Primary electrons are accelerated towards the sense wires, the anode. The electric field near the anode is high and the electrons are accelerated

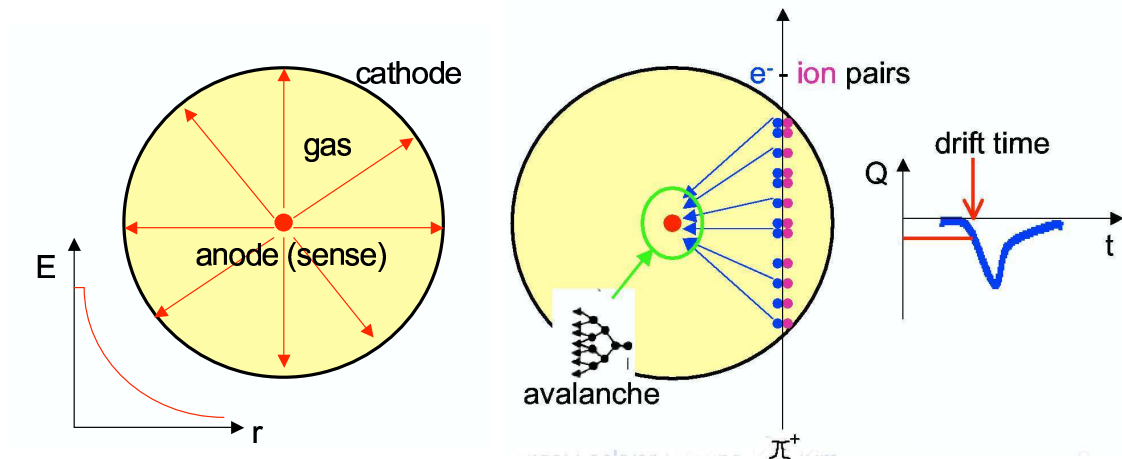


**Figure 4.2:** Sense wire in drift chamber [33].

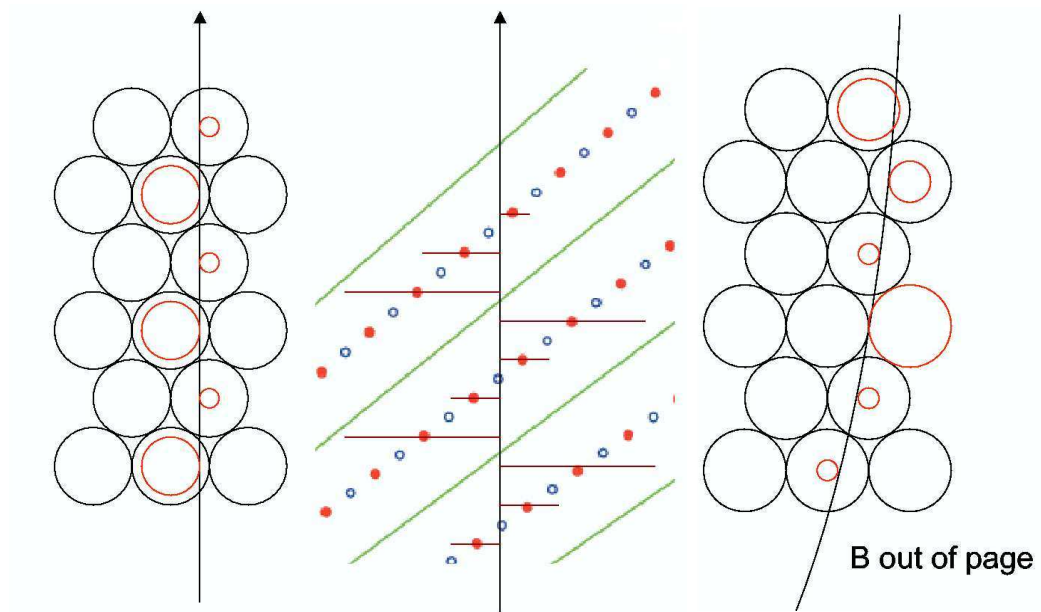


**Figure 4.3:** Tracking [33].

to an energy high enough to ionize more gas atoms. The secondary electrons, will form further electron-ion pairs and cause electron avalanche multiplication. A large electrical signal is induced when the primary and secondary electrons hit a sense wire. The signal is proportional to the energy loss per unit length,  $dE/dx$ , of the transvers-

ing charged particle. The spatial location of the primary electrons is determined by measuring the "drift time", the time of the electrons arrival at the sense wire relative to a time  $t_0$  (e.g. collision time).

The drift chamber have axial wires and stereo wires. The axial wires, parallel to the beam line, provide position measurements in the  $r - \phi$  plane. The stereo wires, tilted  $2^\circ$  to the beam line, provides position measurements in the  $r - z$  plane. The position resolution of the CDF COT drift chamber is  $\approx 140 \mu\text{m}$ .

For hits on three consecutive wires, there are 8 combinations of possible hits, since each wire has left-right ambiguity (see Figure 4.3). Only one of these combinations is correct, the ambiguity is solved by staggering the position of the drift tubes. By applying a magnetic field to the chamber, the momentum of the charged particles can be determined from the curvature  $C$  (in  $m^{-1}$ ) of the track:

$$P = 0.3RB = 0.3B/C \quad (4.1)$$

where,  $P$  (in  $\text{GeV}/c$ ) is the momentum of the charged particles,  $B$  (in Tesla) is the magnetic field and  $R$  is the radius of the track. The momentum resolution of CDF COT drift chamber is  $\sigma(p_T)/p_T^2 = 0.0015(\text{GeV}/c)^{-1}$  [34].

Silicon microstrip tracking detector is used at the detector inner radius to provide high precision tracking and vertex measurement. The vertex  $z_0$  resolution of the CDF inner silicon tracker is  $\approx 70 \mu\text{m}$  [35].

### 4.1.2 Calorimeters

The calorimeters measure the energy of electrons, photons and hadrons. A general-purpose calorimeter has an initial electromagnetic section followed by a dense hadron calorimeter. The calorimeter is segmented in  $\eta$  and  $\phi$  to form a projective tower geom-

etry. Each tower points back to the interaction region (see Figure 4.4). The calorimeter uses a sampling technique for energy measurement. Individual calorimeter cells consist of layers of absorber and scintillator detector (see Figure 4.5). Particles create electromagnetic and hadron particle showers in the absorber and the energy deposit in the scintillator detector is read out by wavelength shifter fibers that direct the light to photomultiplier tubes.

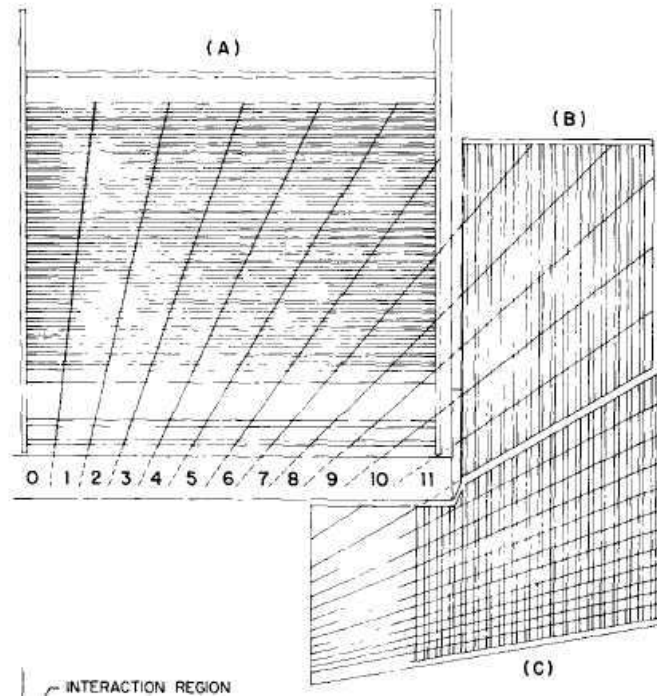


**Figure 4.4:** CDF calorimeter coverage (sideview) [36].

## Electromagnetic Calorimeter

Electromagnetic calorimeters measure the energy of electrons and photons. Electrons and photons interact via bremsstrahlung and electron pair production in the calorimeter. The secondary particles are a cascade of electrons and photons. By repeating these processes, an electromagnetic shower is developed. The amount of



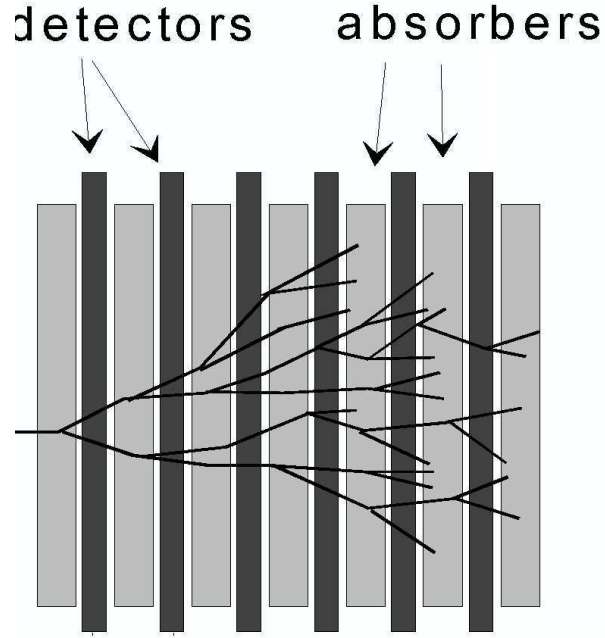


**Figure 4.5:** Sampling calorimeters [37].

ionization charge deposited in the calorimeter is proportional to the energy of the particle that initiates the shower. The CDF central electromagnetic calorimeter consists of 31 layers of 0.125 in lead absorber interleaved with 5 mm scintillator detector which give a total radiation length of  $18 X_0$ . The radiation length  $X_0$  is defined as the length of the material which reduces electron energy by a factor of  $e$ .

### Hadron Calorimeter

Hadrons undergo inelastic nuclear interactions in the hadron calorimeter and produce secondary hadrons, which again produce hadrons through inelastic nuclear interactions. By repeating these processes, a hadron particle shower is developed. Hadron showers penetrate much deeper and are broader than electromagnetic showers, so hadron calorimeters are larger compared to electromagnetic calorimeters. The CDF central hadron calorimeter consists of 32 layers of 2.5 cm steel absorber interleaved

with 1.0 cm scintillator detector giving a total hadronic absorption length of  $4.7 \lambda_0$ . The hadronic absorption length  $\lambda_0$  is defined as the length of the material which reduces pion energy by a factor of  $e$ .

### 4.1.3 Muon Detectors

A muon detector is a charge particle detector located outside the dense EM and hadronic calorimeter. The energy loss  $\frac{dE}{dx}$  for particles in the calorimeter material is proportional to  $\frac{E}{m^2}$ , where  $E$  is the energy and  $m$  is the mass of the particles [37]. The mass of the electron  $m_e$  is 0.5 MeV, while the mass of the muon  $m_\mu$  is 105.7 MeV. The energy loss of electrons in the material is a factor of  $4 \times 10^4$  larger than that of muons. The calorimeter material absorbs electrons, photons and hadrons. Muons deposit very little energy in the calorimeter and reach the muon chamber. The more material in the absorber, the better muon purity achieved. A typical muon detector system, shown in Figure 4.6, consists of a steel absorber, four layers of drift chambers and a scintillation counter. The adjacent drift chambers are ganged together (see Figure 4.7). The position of the track in the  $r - \phi$  plane is determined as in the drift chamber (see Section 4.1.1). The  $z$  position of the track can be determined based on charge division [38]:

$$z(\mu) = L \frac{Q_A - Q_B}{Q_A + Q_B} \quad (4.2)$$

where  $L$  is the length of the chamber,  $Q_A$  and  $Q_B$  are charges accumulated on wire A and B respectively. A simple model of charge division is illustrated in Figure 4.8, where a particle deposits charge on the wires a distance  $z$  from the "ganged" end of the chamber. The resistance of wire A and wire B is  $R$ , and the currents on wire A and wire B are  $I_A$  and  $I_B$  respectively. Let the length of the wire be  $L$ . By Ohm's

Law, we have:

$$I_B(R + R\frac{z}{L}) = V = I_A(R\frac{L-z}{L}) \quad (4.3)$$

which gives:

$$z(\mu) = L \frac{I_A - I_B}{I_A + I_B} \quad (4.4)$$

By replacing the currents with charges accumulated from each wires, we obtain the charge division Equation 4.2.

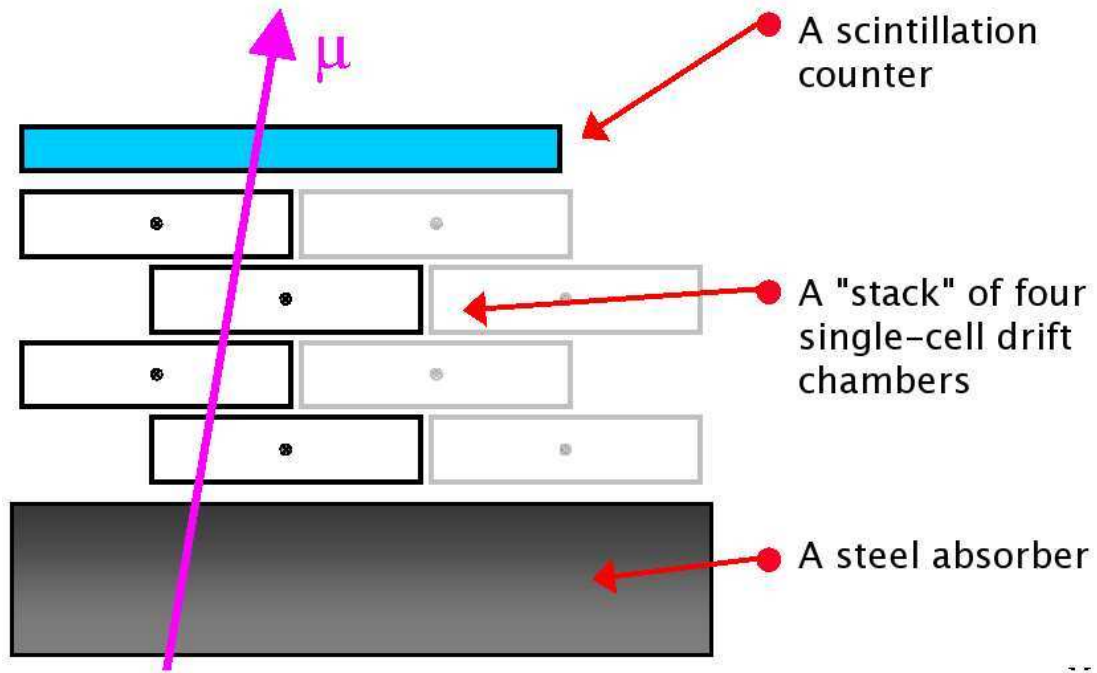


**Figure 4.6:** A muon detector system [38].

## 4.2 The Collider Detector at Fermilab

The Collider Detector at Fermilab (CDF) is a general purpose detector system for studying  $p\bar{p}$  collisions at the Tevatron collider. It contains tracking, calorimeter and muon systems. The tracking systems are inside a superconducting solenoid, which



**Figure 4.7:** Drift Chambers (in blue) with resistance readout wires (in red) [38].

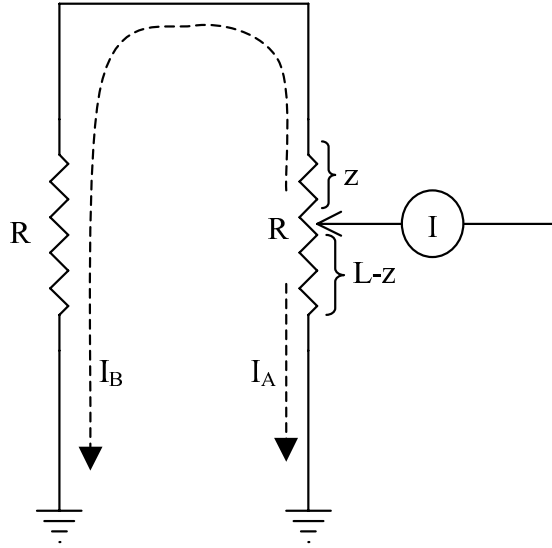


**Figure 4.8:** A simple module of charge division [39].

is 1.5 m in radius and 4.8 m in length generating a magnetic field of 1.4 T. The calorimeter and muon systems are outside the solenoid. Figure 4.9 shows an overview of the CDF detector. Figure 4.10 is an overview of the CDF inner detector.

### 4.2.1 The CDF Coordinate System

The following coordinates are used at CDF:

- $z$ : distance along the beamline. The positive  $z$ -axis is defined as the direction

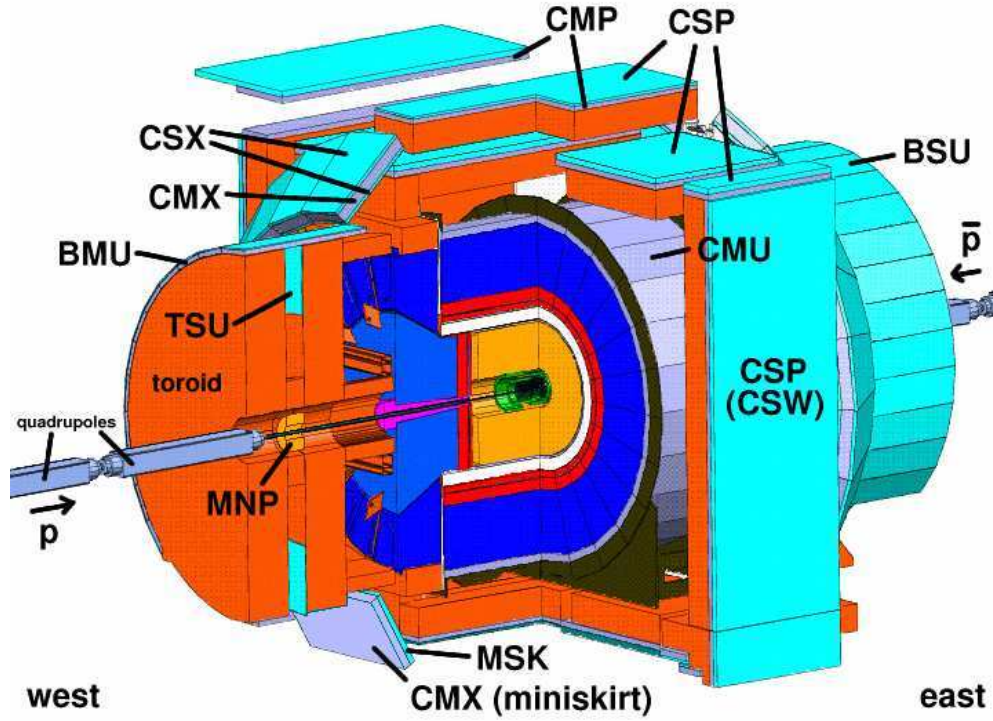


Figure 4.9: CDF detector cutaway view [36].

of the proton beam (east).  $z = 0$  is the interaction point.

- The x-y plane is the plane transverse the beam direction. The positive x-axis is pointing towards the outside of the Tevatron ring (north). And the positive y-axis is pointing upwards.
- The polar angle  $\theta$ : measured from the beam line along the proton direction.
- The pseudo-rapidity  $\eta$ : defined as  $\eta = -\ln(\tan(\theta/2))$
- The azimuthal angle  $\phi$  around the beam line: measured from the Tevatron plane. North is  $\phi = 0$ , up is  $\phi = 90^\circ$ .
- $r$ : radial distance from the beamline.

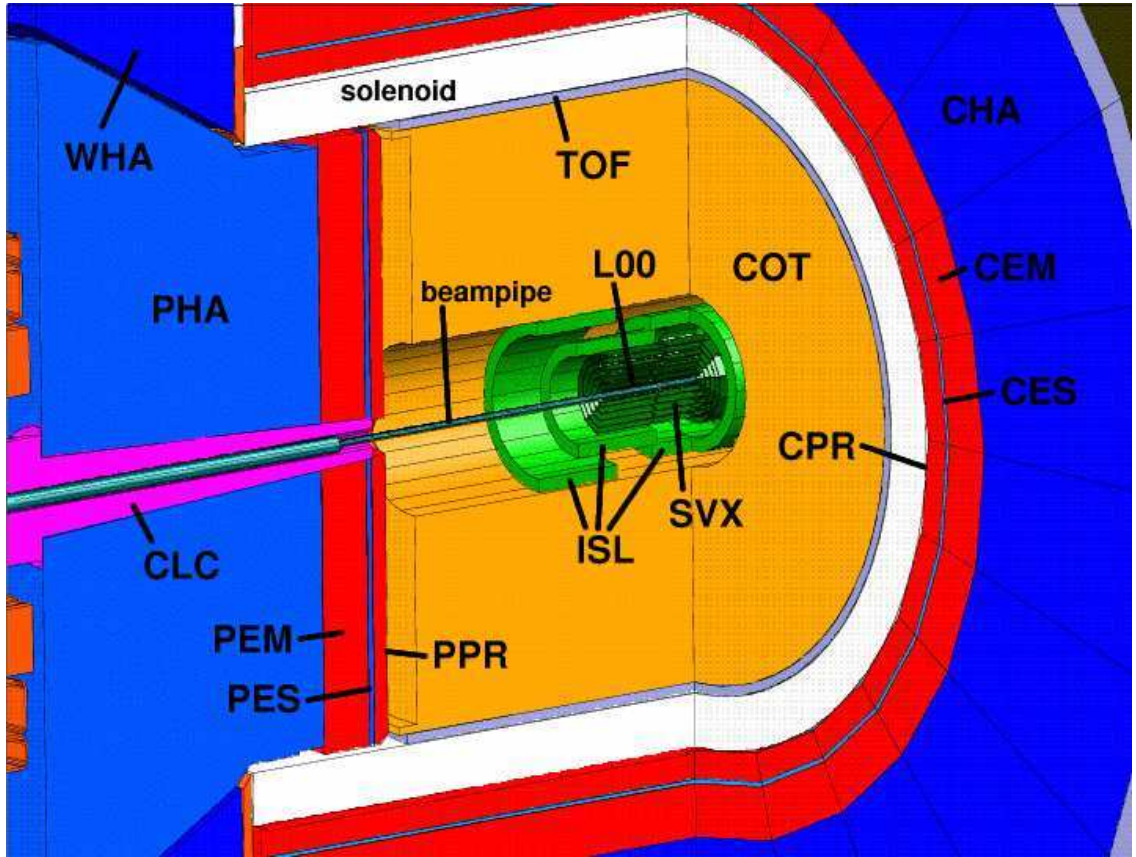


Figure 4.10: CDF inner detector cutaway view [36].

## 4.2.2 CDF Center Outer Tracking (COT)

The tracking system consists of a drift chamber and a silicon microstrip system (see Figure 4.11).

### COT Drift Chamber

The CDF COT is a 3.1 meter cylindrical drift chamber. It has 96 layers of sense wires, covering a radial range from 40 to 137 cm. These layers are grouped into 8

## CDF Tracking Volume

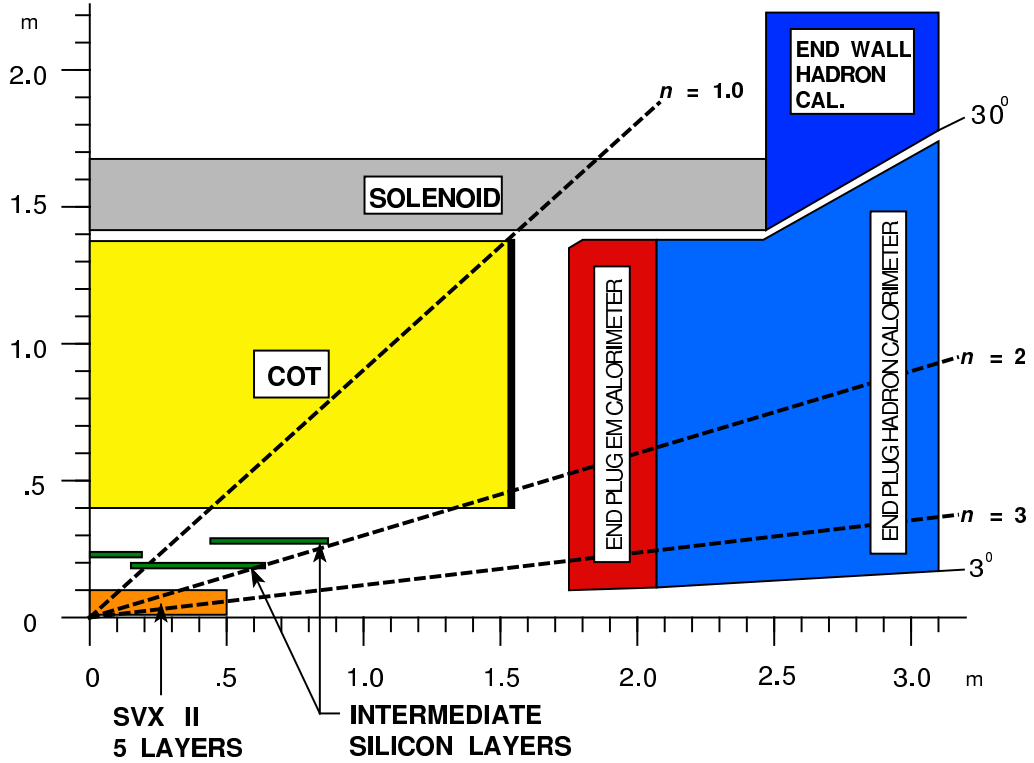


**Figure 4.11:** Longitudinal view of the CDF tracking system [40].

“superlayers”. Each superlayer is divided in  $\phi$  into “supercells”. A supercell, shown in figure 4.12 for superlayer 2, has 12 sense wires. A magnetic field  $B$  of 1.4 Tesla is applied to the drift chamber. The charged particles drifting in the electric field are deflected by the magnetic field. The COT has a coverage of  $|\eta| \leq 1$ . The hit position resolution of COT is  $\approx 140 \mu\text{m}$  and its momentum resolution is  $\sigma(p_T)/p_T^2 = 0.0015(\text{GeV}/c)^{-1}$  [34].

### COT Readout Electronics

Figure 4.13 shows an overview of the COT readout electronics. The Amplifier-Shaper-Discriminator (ASDQ) board, the readout chip which amplifies, shapes, discriminates

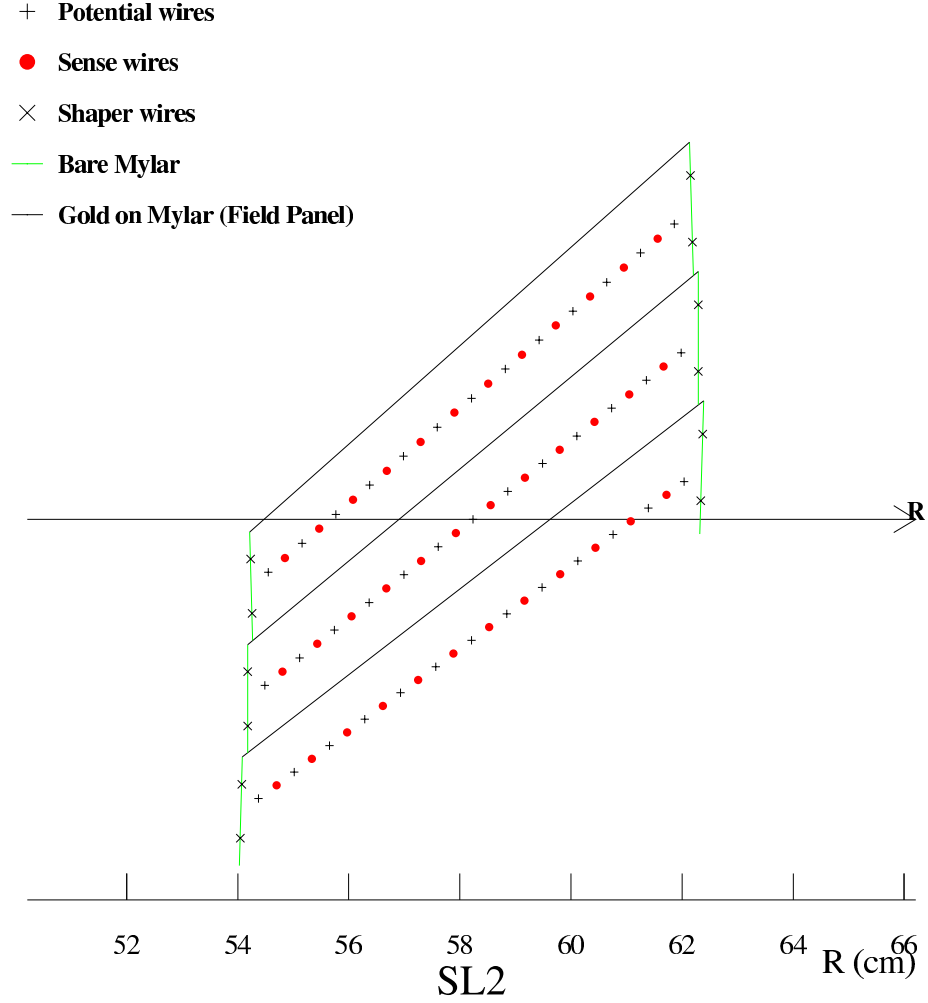


**Figure 4.12:** Super cell layout [41].

and measures charge, generates an output pulse with a pulse width logarithmically proportional to the input charge. The pulse is fed to a Time-to-Digital Converter (TDC) chip which records the arrival time of its leading edge and trailing edge in 1 ns bins. A TDC daughter board generates a fast signal which is sent to an eXtremely Fast Tracker (XFT) board. The XFT finds charged tracks and generates information used in Level-1 trigger decision (see Section 4.3 for more information about the CDF trigger system). The TDC has a  $5.6 \mu s$  time window. A Level-1 trigger accept directs



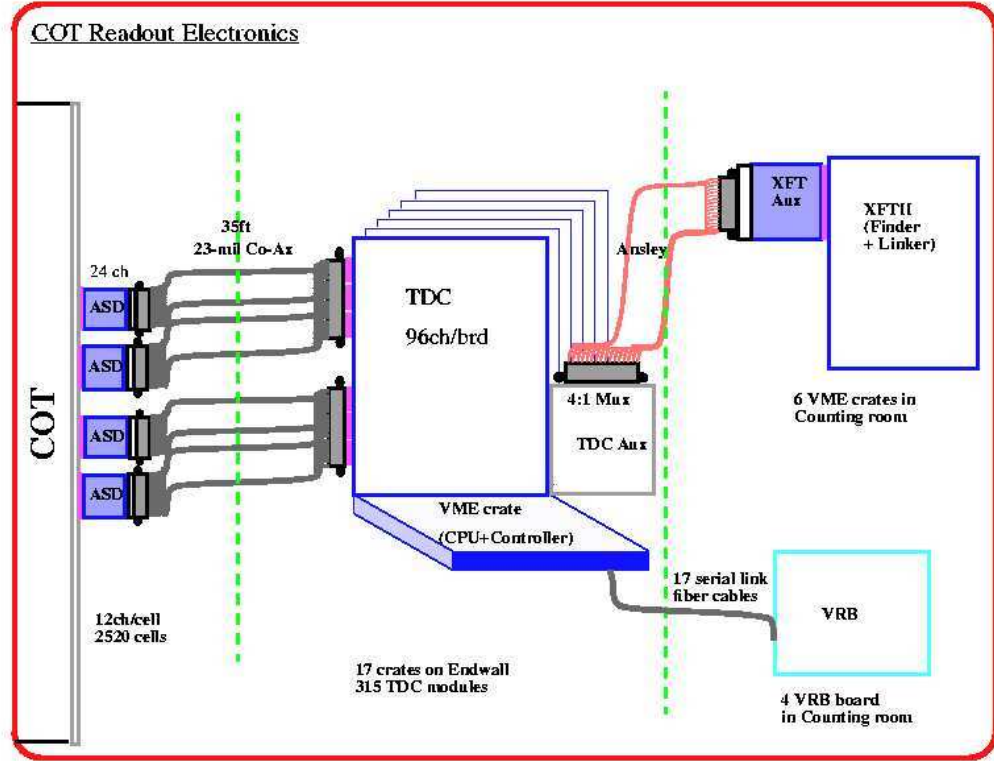


Figure 4.13: An overview of the COT readout electronics [41].

the oldest data to a Level-2 storage buffer. There are four buffers in each TDC chip, each of these buffers holds  $2.0 \mu\text{s}$  of timing data. A Level-2 trigger accept causes the TDC chip to digitize this data and send the digitized signal to the remaining readout chain for full event processing.

### 4.2.3 Inner Tracker

The inner tracker is a silicon microstrip system, which consists of eight-layer silicon detectors between radii of 1.5 cm and 28 cm from the beam line. The layer closest to the beam pipe, called layer 00, is located at a radius of 1.5 cm and provides coverage for  $|\eta| < 4.0$ . The next five layers are the Silicon Vertex Detector (SVX) system covering  $|\eta| < 2.0$ . The outer two layers (three layers in the forward region) are the

Intermediate Silicon Layer (ISL) system (see Figure 4.11). The vertex  $z_0$  resolution of SVX and ISL is  $\approx 70 \mu\text{m}$  [35].

#### 4.2.4 Calorimeter

The calorimeter systems provide energy measurement of electrons, photons and hadronic jets. The central calorimeter has 24 wedges in  $\phi$  and 10 towers in  $\eta$  on both east and west sides. Each tower is 15 degrees in azimuth and  $\approx 0.11$  in  $\eta$ . Each wedge consists of a lead-scintillator sampling electromagnetic calorimeter, followed by a steel-scintillator sampling hadron calorimeter.

##### Central Electromagnetic Calorimeter (CEM)

The CEM is a lead-scintillator sampling calorimeter. It provides coverage for  $|\eta| < 1.1$ , its energy resolution is  $13.5\%/\sqrt{E_t}$  with a 2% constant term [34].

##### Central E-M ShowerMax chamber (CES)

The CES detector is embedded within CEM wedges (see Figure 4.10), approximately 6 radiation lengths  $X_0$  deep. The CES detector is a strip and wire chamber, where the wire measures the position in  $\phi$  and the strip measures the position in  $\eta$ . It provides high-precision measurements of the  $(x, y)$  position at the expected shower maximum of electrons and photons in the EM calorimeter. The position resolution is about 2mm [42]. The measured transverse shower profile is used to distinguish photons from  $\pi^0$ 's.

### Central Pre-Radiator chamber (CPR)

The CPR chamber is mounted on the inner surface of the CEM wedges (see Figure 4.10). For each wedge, there are 32 wires running along the beam direction in each CPR chamber. The solenoid and the Central Outer Tracking (COT) detector serve as radiators for the CPR detector. The conversion rate of photons in the solenoid is measured by the charge deposited in the CPR detector. The difference in the conversion rate for single photons and two photons from  $\pi^0 \rightarrow \gamma\gamma$  decay can be used to extract the pion background fraction in a photon sample.

### Central Hadronic Calorimeter (CHA)

The CHA is a steel-scintillator sampling calorimeter. It provides coverage for  $|\eta| < 0.9$ . Its energy resolution is  $75\%/\sqrt{E_t}$  with a 3% constant term [34].

### Plug Calorimeter

The plug calorimeter is located outside the barrel end of the COT, providing coverage of  $1.1 < |\eta| < 3.6$ . There is an electromagnetic section followed by a hadron section. The Plug Electromagnetic Calorimeter (PEM) is a lead-scintillator sampling calorimeter with layers of 4.5 mm lead and 4 mm scintillator. Its energy resolution is  $16\%/\sqrt{E_t}$  with a 2% constant term [34]. The Plug Hadronic Calorimeter (PHA) is located beyond the PEM, which is an iron-scintillator sampling device with layers of 2 inch iron and 6 mm scintillator. Its energy resolution is  $74\%/\sqrt{E_t}$  with a 4% constant term [34].

### 4.2.5 Muon Systems

The Muon detector (see Figure 4.9) consists of four systems of scintillators and proportional chambers for muon detection in the range  $|\eta| < 1.5$ . Table 4.1 summarizes the  $\eta$  coverage of the four muon systems.

**Table 4.1:** The  $\eta$  coverage of the CDF muon detectors.

Chambers	$ \eta_{min} $	$ \eta_{max} $
Central Muon Chambers (CMU)	0	0.6
Central Muon Upgrade (CMP)	0	0.6
Central Muon Extension(CMX)	0.6	1.0
Barrel Muon Chambers (BMU)	1.0	1.5

The Central Muon Chambers (CMU) located outside the CHA wedges, detects muons with  $p_T > 1.4$  GeV in the central detector region in the range  $|\eta| < 0.6$ . The calorimeter steel is the absorber for the CMU system. The Central Muon Upgrade (CMP) consists of a second set of muon chambers behind an additional 60 cm of steel outside the magnet return yoke. Four layers of planar drift chambers detect muons with  $p_T > 2.2$  GeV in the central detector region of  $|\eta| < 0.6$ . The Central Muon Extension (CMX) consists of conical sections of drift tubes, located at each end of the central detector. It extends the central muon coverage to  $|\eta| < 1.0$ . The calorimeter, magnet yoke and steel of the detector end support structure are the absorber materials for the CMX detector. It detects muons with  $p_T > 1.4$  GeV in the central detector region in the range  $0.6 < |\eta| < 1.0$ . The Barrel Muon Chambers (BMU) provides muon detection in the forward region of  $1.0 < |\eta| < 1.5$ . It is located on the outside of the toroids, which provide absorbing steel for the BMU.

## 4.3 Trigger and Data Acquisition Systems

The CDF trigger and data acquisition systems are designed to accommodate the high data rate and large data volume from the detector. Figure 4.14 shows the functional block of the CDF data flow, which is a 3-tier trigger system. The first level trigger is a hardware based trigger and can process one event every 132 ns. Data from the tracking, the calorimeter and the muon detectors are sent to the Level-1 trigger system. Upon a Level-1 trigger accept, the data are transferred to one of the four Level-2 buffers. The Level-2 trigger is a combination of hardware and software trigger, which has an average decision time of 20  $\mu$ s. Upon a Level-2 trigger accept, the data from all detectors are collected in DAQ buffers and transferred to a Level-3 computer farm where the final level of event filtering is performed. Upon a Level-3 accept, the event is written to storage for offline analysis.

Figure 4.15 shows the block diagram for the CDF Run IIa trigger system. Various trigger subsystems generate variables for trigger decisions. At Level-1, available variables are:

- $P_t$  of a charged track from the XFT
- $E_{\text{EM}}$ ,  $E_{\text{HAD}}$  and HAD/EM from calorimeters
- Imbalance in the total transverse momentum  $\cancel{E}_t$

At Level-2, available variables are:

- $P_t$  and impact parameter of a charged track from the Silicon Vertex Tracker
- Energy of a jet cluster
- The (x,y) position from the EM ShowerMax chamber

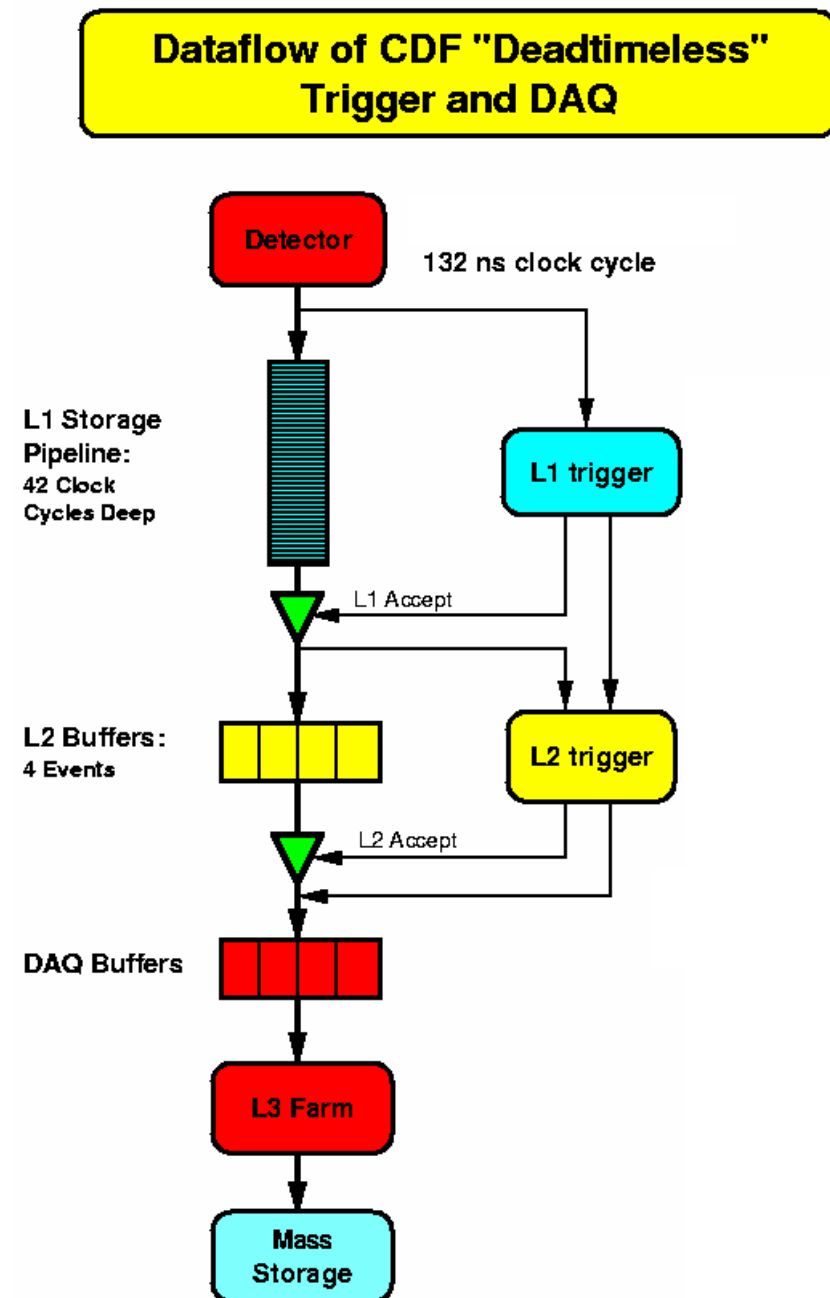
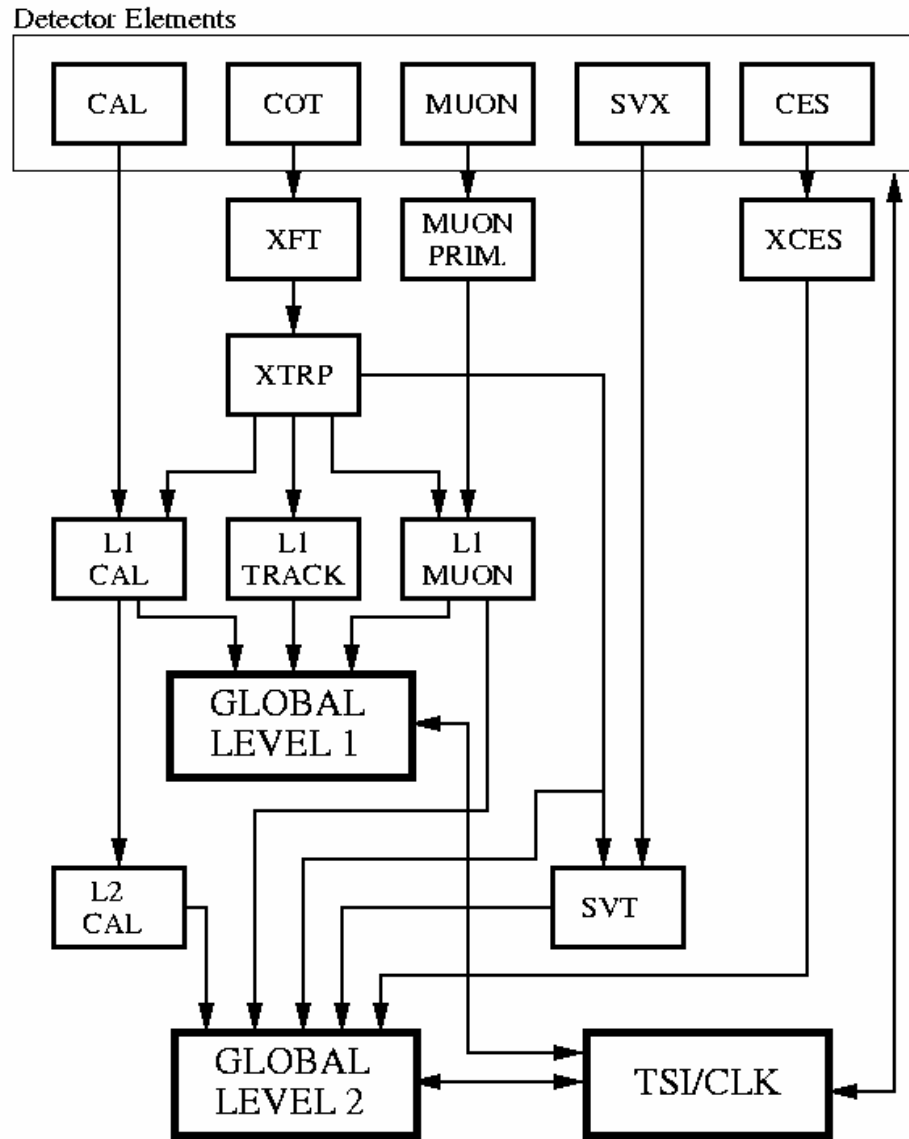


Figure 4.14: Functional block diagram of the CDF Run II data flow [43].



**Figure 4.15:** Block diagram of the CDF Run IIa trigger system [43].

To accommodate increasing instantaneous luminosity, several DAQ subsystems (including Level-2 trigger, Level-3 farm/Event Builder, TDC and XFT) have been upgraded since 2004. Table 4.2 compares DAQ specification before and after the upgrade. The upgraded DAQ system is able to accommodate a 30 kHz Level-1 accept rate, a 1000 Hz Level-2 accept rate and a 100 Hz rate at Level-3.

**Table 4.2:** DAQ and trigger specification, Run IIa vs IIb [44].

	<b>Run IIa Specification</b>	<b>Run IIa Achieved</b>	<b>Run IIb Specification</b>
<b>Luminosity</b>	$8.6 \times 10^{31}$	$9.0 \times 10^{31}$	$30 \times 10^{31}$
<b>L1 Accept</b>	45 kHz	25 kHz	30 kHz
<b>L2 Accept</b>	300 Hz	350 Hz	1000 Hz
<b>Event Builder</b>	75 MB/s	75 MB/s	500 MB/s
<b>L3 Accept</b>	75 Hz	80 Hz	100 Hz
<b>Rate to Storage</b>	20 MB/s	20 MB/s	40 MB/s
<b>Deadtime Trigger</b>	5%	10%	5% + 5% †

## 4.4 Chapter Summary

The CDF detector collects proton-antiproton collision data at a center of mass energy of 1.96 TeV. The  $p\bar{p}$  collisions produce particles such as  $e^\pm$ ,  $\mu^\pm$ ,  $\nu$ ,  $\gamma$ , pions and B hadrons, which are identified and measured using various components of the CDF detector. The  $p\bar{p}$  collision rate is 2.5 MHz and the CDF trigger system selects 100 events per second for further offline analysis. In the next chapter, a theory review of  $\gamma$ ,  $W^\pm$  and  $Z^0$  boson pair production at the Tevatron is presented. This is followed by a detailed description of the measurement of electrons, photons and Z bosons using the CDF detector.



## Chapter 5

# Gauge Boson Pair Production and Trilinear Couplings

Electroweak theory makes precise predictions for the couplings between the  $\gamma$ ,  $Z^0$  and  $W^\pm$  gauge bosons. Pair production of the bosons provides direct tests of the predicted triple gauge boson couplings. Any non Standard Model (anomalous) couplings enhance boson pair production cross-sections and would indicate contributions from new physics processes. In this chapter, a theoretical overview of diboson physics and triple gauge boson couplings is presented. The Standard Model prediction for  $Z\gamma$  production from  $p\bar{p}$  at  $\sqrt{s} = 1.96$  TeV is presented in Section 5.3.

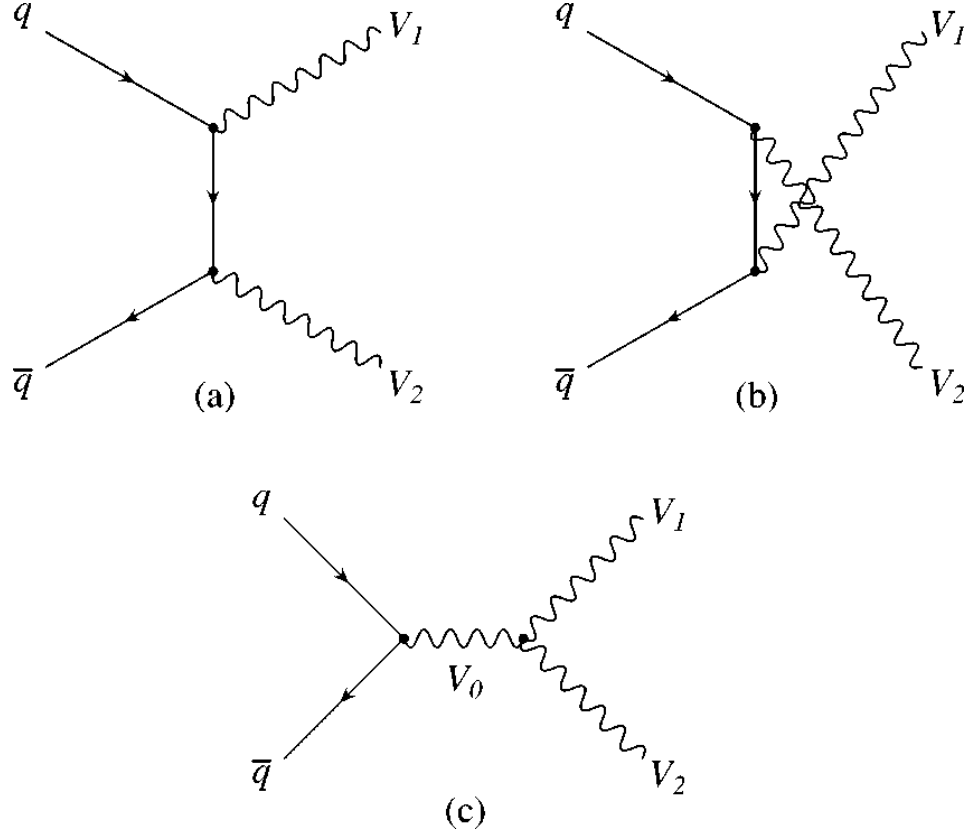
### 5.1 Triple Gauge Boson Couplings

Figure 5.1 shows the Feynman diagrams for gauge boson pair production from  $q\bar{q}$  collision. Figure 5.1 (a) and (b) are diagrams for quark - boson interactions and represent initial state radiation (ISR) from the incoming quarks. Figure 5.1 (c) shows diboson production from a trilinear gauge boson vertex.

The triple gauge boson vertices arise from the cubic terms in the gauge field Lagrangian. This can be obtained from [4]:

$$-\frac{1}{4}(F_{\mu\nu}^i)^2, \quad \text{where } F_{\mu\nu}^i = \partial_\mu A_\nu^i - \partial_\nu A_\mu^i + g\epsilon^{ijk}A_\mu^j A_\nu^k. \quad (5.1)$$

When we rewrite the cubic term in the basis of mass eigenstate fields (see Eqs. A.31



**Figure 5.1:** Feynman diagrams for gauge boson pair production.  $V_{0,1,2}$  are the photon, W or Z gauge boson [45].

in Appendix A), we get

$$\begin{aligned}
-\frac{1}{4}(F_{\mu\nu}^i)^2 &\rightarrow -\frac{1}{2}(\partial_\mu A_\nu^i - \partial_\nu A_\mu^i)g\epsilon^{ijk}A^{\mu j}A^{\nu k} \\
&= -g(\partial_\mu A_\nu^1 - \partial_\nu A_\mu^1)A^{\mu 2}A^{\nu 3} + g(\partial_\mu A_\nu^2 - \partial_\nu A_\mu^2)A^{\mu 1}A^{\nu 3} \\
&\quad - g(\partial_\mu A_\nu^3 - \partial_\nu A_\mu^3)A^{\mu 1}A^{\nu 2} \\
&= -ig[(\partial_\mu W_\nu^+ - \partial_\nu W_\mu^+)W^{\mu-}A^{\nu 3} - (\partial_\mu W_\nu^- - \partial_\nu W_\mu^-)W^{\mu+}A^{\nu 3} \\
&\quad + \frac{1}{2}(\partial_\mu A_\nu^3 - \partial_\nu A_\mu^3)(W^{\mu+}W^{\nu-} - W^{\mu-}W^{\nu+})].
\end{aligned} \tag{5.2}$$

Inserting  $A_\mu^3 = \cos\theta_w Z_\mu + \sin\theta_w A_\mu$  and  $g = e/\sin\theta_w$ , the couplings at the WWV vertex ( $V = \gamma$  or Z boson) can be obtained.

The possible trilinear couplings involving the W boson, the Z boson and the photon are WW $\gamma$ , WWZ, ZZZ, ZZ $\gamma$  and Z $\gamma\gamma$ . As shown in Equation 5.2, only the first two couplings have non-zero values in the Standard Model; all the neutral triple couplings vanish at tree level.

### 5.1.1 Charge Triple Gauge Boson Couplings

Under the assumption of electroweak gauge and Lorentz invariance, and including only CP conserving terms, the WW $\gamma$  vertex is described by the effective Lagrangian [46]:

$$\begin{aligned} L_{WW\gamma} = & -ie[(W_{\mu\nu}^+ W^\mu A^\nu - W_\mu^+ A_\nu W^{\mu\nu}) \\ & + \kappa_\gamma W_\mu^+ W_\nu F^{\mu\nu} + \frac{\lambda_\gamma}{M_W^2} W_{\lambda\mu}^+ W_\nu^\mu F^{\nu\lambda}], \end{aligned}$$

where  $F_{\mu\nu}$  is the photon tensor, and  $W_{\mu\nu} = \partial_\mu W_\nu - \partial_\nu W_\mu$ . In the SM at tree level,

$$\Delta\kappa_\gamma = \kappa_\gamma - 1 = 0, \quad \lambda_\gamma = 0.$$

The WWZ vertex is described by the effective Lagrangian [47]:

$$\begin{aligned} L_{WWZ} = & -ie \cot(\theta_w) g_1^Z [(W_{\mu\nu}^+ W^\mu Z^\nu - W_\mu^+ Z_\nu W^{\mu\nu}) \\ & + \kappa_Z W_\mu^+ W_\nu Z^{\mu\nu} + \frac{\lambda_Z}{M_W^2} W_{\lambda\mu}^+ W_\nu^\mu Z^{\nu\lambda}]. \end{aligned}$$

In the SM at tree level,

$$\Delta g_1^Z = g_1^Z - 1 = 0, \quad \Delta \kappa_Z = \kappa_Z - 1 = 0, \quad \lambda_Z = 0.$$

The production of  $W\gamma$  pairs and  $WZ$  pairs depends on the  $WW\gamma$  and  $WWZ$  triple couplings respectively, while  $WW$  production is sensitive to both  $WW\gamma$  and  $WWZ$  couplings. The status of measurements of  $W\gamma$ ,  $WZ$  and  $WW$  production from  $p\bar{p}$  collision at  $\sqrt{s} = 1.96$  TeV are summarized in Section 2.3.

### 5.1.2 Neutral Triple Gauge Boson Couplings

Under the assumption of electroweak gauge and Lorentz invariance, the neutral tri-linear boson vertex is described by [48]:

$$\begin{aligned} \Gamma_{Z\gamma V}^{\alpha\beta\mu}(q_1, q_2, P) &= \frac{i(P^2 - m_V^2)}{m_Z^2} \left\{ h_1^V (q_2^\mu g^{\alpha\beta} - q_2^\alpha g^{\mu\beta}) + \frac{h_2^V}{m_Z^2} P^\alpha [(Pq_2)g^{\mu\beta} - q_2^\mu P^\beta] \right. \\ &\quad \left. - h_3^V \epsilon^{\mu\alpha\beta\rho} q_{2\rho} - \frac{h_4^V}{m_Z^2} P^\alpha \epsilon^{\mu\beta\rho\sigma} P_\rho q_{2\sigma} \right\}, \\ \Gamma_{ZZV}^{\alpha\beta\mu}(q_1, q_2, P) &= \frac{i(P^2 - m_V^2)}{m_Z^2} [f_4^V (P^\alpha g^{\mu\beta} + P^\beta g^{\mu\alpha}) - f_5^V \epsilon^{\mu\alpha\beta\rho} (q_1 - q_2)_\rho], \end{aligned}$$

where  $V = Z$  or  $\gamma$ . The notation of the vertex is given in Figure 5.2 with  $P = q_1 + q_2$ . The  $Z\gamma V$  vertex (see Figure 5.3 (a)), where  $Z$  and  $\gamma$  are on-shell gauge bosons and  $V = Z$  or  $\gamma$  is off-shell, is described by 8 parameters  $h_i^V$  ( $i = 1 - 4$ ,  $V = Z$  or  $\gamma$ ). The  $ZZV$  vertex (see Figure 5.3 (b)), with two on-shell  $Z$  bosons and an off-shell  $V = Z$  or  $\gamma$ , is described by 4 parameters  $f_i^V$  ( $i = 5, 6$ ,  $V = Z$  or  $\gamma$ ). The couplings  $h_1^V$ ,  $h_2^V$  and  $f_4^V$  are CP-violating, while the couplings  $h_3^V$ ,  $h_4^V$  and  $f_5^V$  are CP-conserving.

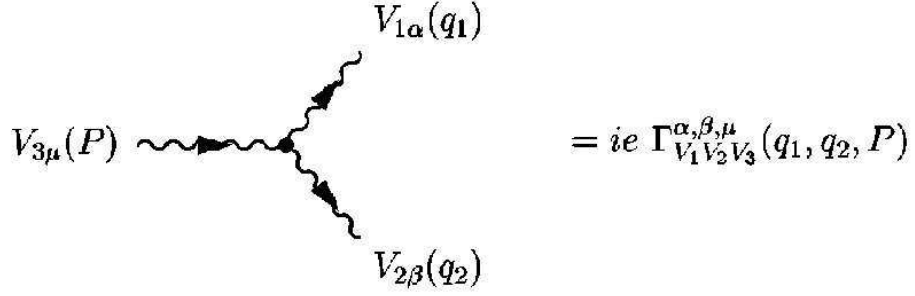


**Figure 5.2:** The general neutral gauge boson vertex  $V_1 V_2 V_3$  [49].

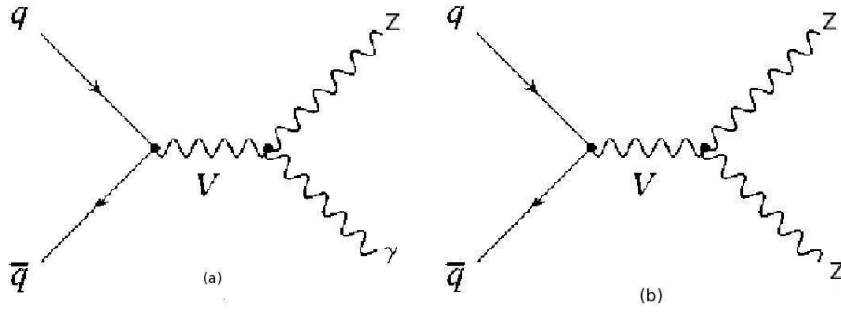


**Figure 5.3:** The neutral gauge boson vertex. (a)  $Z\gamma V$  vertex and (b)  $ZZV$  vertex ( $V = Z$  or  $\gamma$ ).

The effective Lagrangian for vertices  $ZZV$  and  $Z\gamma V$  is [48]

$$\begin{aligned}
L = & \frac{e}{m_Z^2} [-f_4^\gamma (\partial_\mu F^{\mu\beta}) + f_4^Z (\partial_\mu Z^{\mu\beta})] Z_\alpha (\partial^\alpha Z_\beta) + [f_5^\gamma (\partial^\sigma F_{\sigma\mu}) + f_5^Z (\partial^\sigma Z_{\sigma\mu})] \tilde{Z}^{\mu\beta} Z_\beta \\
& - [h_1^\gamma (\partial^\sigma F_{\sigma\mu}) + h_1^Z (\partial^\sigma Z_{\sigma\mu})] Z_\beta F^{\mu\beta} - [h_3^\gamma (\partial_\sigma F^{\sigma\rho}) + h_3^Z (\partial_\sigma Z^{\sigma\rho})] Z^\alpha \tilde{F}_{\rho\alpha} \\
& - \left\{ \frac{h_2^\gamma}{m_Z^2} [\partial_\alpha \partial_\beta \partial^\rho F_{\rho\mu}] + \frac{h_2^Z}{m_Z^2} [\partial_\alpha \partial_\beta (\square + m_Z^2) Z_\mu] \right\} Z^\alpha F^{\mu\beta} \\
& + \left\{ \frac{h_4^\gamma}{2m_Z^2} [\square \partial^\sigma F^{\rho\alpha}] + \frac{h_4^Z}{2m_Z^2} [(\square + m_Z^2) \partial^\sigma Z^{\rho\alpha}] \right\} Z_\sigma \tilde{F}_{\rho\alpha},
\end{aligned}$$

where  $Z_{\mu\nu} = \partial_\mu Z_\nu - \partial_\nu Z_\mu$ ,  $\tilde{Z}_{\mu\nu} = 1/2 \epsilon_{\mu\nu\rho\sigma} Z^{\rho\sigma}$  and similarly for the photon tensor  $F_{\mu\nu}$ .

The relations of the couplings to physical quantities are as follows [49]:

$$\begin{aligned}\mu_Z &= \frac{-e}{\sqrt{2}m_Z} \frac{E_\gamma^2}{m_Z^2} (h_1^Z - h_2^Z) & Q_Z^e &= \frac{2\sqrt{10}e}{m_Z^2} h_1^Z \\ d_Z &= \frac{-e}{\sqrt{2}m_Z} \frac{E_\gamma^2}{m_Z^2} (h_3^Z - h_4^Z) & Q_Z^m &= \frac{2\sqrt{10}e}{m_Z^2} h_3^Z\end{aligned}$$

where  $\mu$  and  $d$  are the magnetic and electric dipole moments of the Z boson respectively.  $Q^m$  and  $Q^e$  are the quadrupole moments of the Z boson.

The contributions from the anomalous couplings rise as the center-of-mass energy ( $\hat{s}$ ) increases and eventually the cross section violates tree-level unitarity (conservation of probability). This can be avoided by introducing form factors that decrease with  $\hat{s}$ :

$$h_i^V(\hat{s}) = \frac{h_{i0}^V}{(1 + \frac{\hat{s}}{\Lambda})^n} \quad (5.3)$$

where  $\Lambda$  is the energy scale of new physics contributing to the anomalous couplings and  $\hat{s}$  is the center-of-mass energy of the process.  $\Lambda = 1.2$  TeV,  $n = 3$  for  $h_{1,3}^V$  and  $n = 4$  for  $h_{2,4}^V$  are chosen for our measurement [50].

## 5.2 $p\bar{p} \rightarrow \mathbf{Z} \gamma + X$ Production

The  $ZZ\gamma$  and  $Z\gamma\gamma$  couplings, involving the interaction of the neutral Z boson and the photon, are studied using  $Z\gamma$  production, where the Z boson decays to electron or muon pairs. The final state of  $Z\gamma$  production contains two leptons (e or  $\mu$ ) and one photon. Figure 5.4 shows the Standard Model Leading Order (LO) processes contributing to  $p\bar{p} \rightarrow l^+l^-\gamma$  production. Drell-Yan production (see Figure 5.4 c and d), where a photon radiates off one lepton, also contributes to this final state. Fig 5.5 shows the anomalous gauge coupling contributions to  $Z\gamma$  production. These vanish

in the SM at Leading Order.

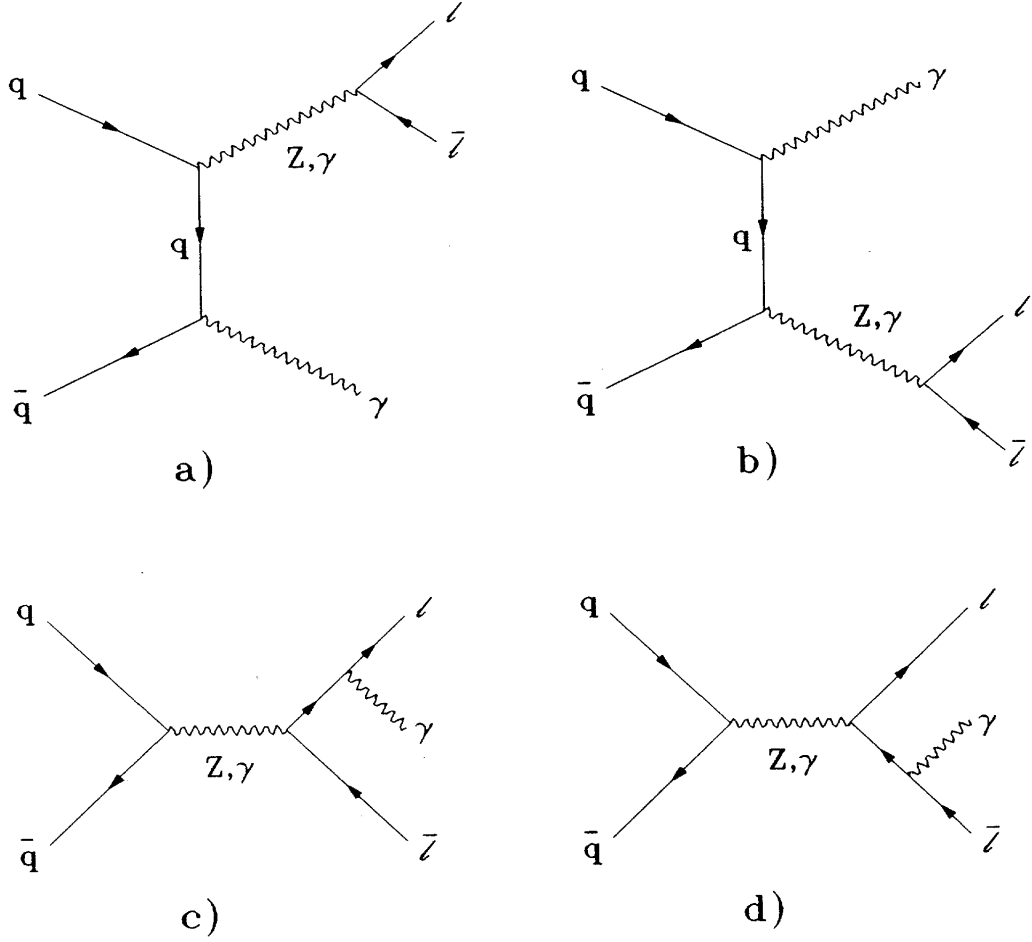


**Figure 5.4:** The leading order Feynman diagrams for  $p\bar{p} \rightarrow l\bar{l}\gamma$  production in the SM. [50]

### 5.3 $p\bar{p} \rightarrow l^+l^-\gamma$ Production Calculation

An event generator ZGAMMA, written by Baur and Berger [50], is used to produce  $p\bar{p} \rightarrow l^+l^-\gamma$  events. The ZGAMMA generator is interfaced to PYTHIA [51] to provide initial state gluon radiation, hadronization and underlying event simulation.

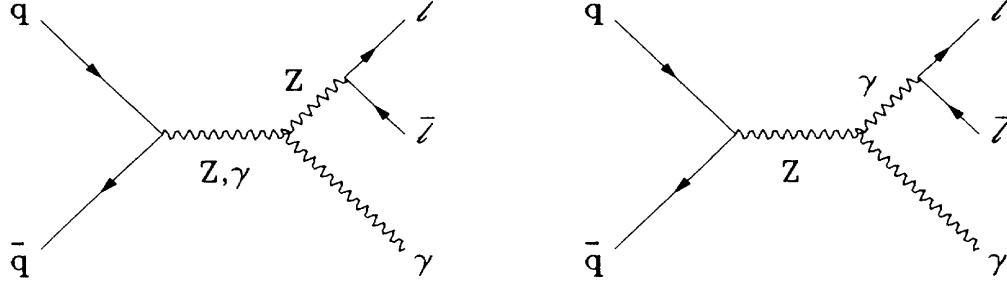


**Figure 5.5:** Anomalous  $ZZ\gamma$  and  $Z\gamma\gamma$  contributions to  $p\bar{p} \rightarrow l\bar{l}\gamma$  production. [50]

After that, the generated events are passed through a full realistic CDF detector simulation. The result of the simulation provides the expected detector response to the generated events.

### 5.3.1 Leading Order (LO) Cross Section

The cross section for  $p\bar{p} \rightarrow l^+l^-\gamma$  production at Leading Order, predicted from the ZGAMMA program, is  $3.4 \pm 0.2$  pb. This is calculated for the following phase space:

- Photon  $E_t$ :  $E_t^\gamma > 7\text{GeV}$
- Lepton-photon separation:  $\Delta R_{l\gamma} = \sqrt{(\Delta\phi_{l\gamma})^2 + (\Delta\eta_{l\gamma})^2} > 0.7$
- Invariant mass of the lepton pair:  $M_{ll} > 40 \text{ GeV}/c^2$

The CTEQ 5L LO parton distribution function (PDF) is used in the calculation. To evaluate the variation in the LO cross section prediction from changing the parton distribution function, the initial CTEQ 5L PDF is changed to CTEQ 6L LHAPDF [52], which has 41 PDF sets. Figure 5.6 plots out cross sections calculated using CTEQ 6L LHAPDF. The green line is the cross section calculated from the CTEQ



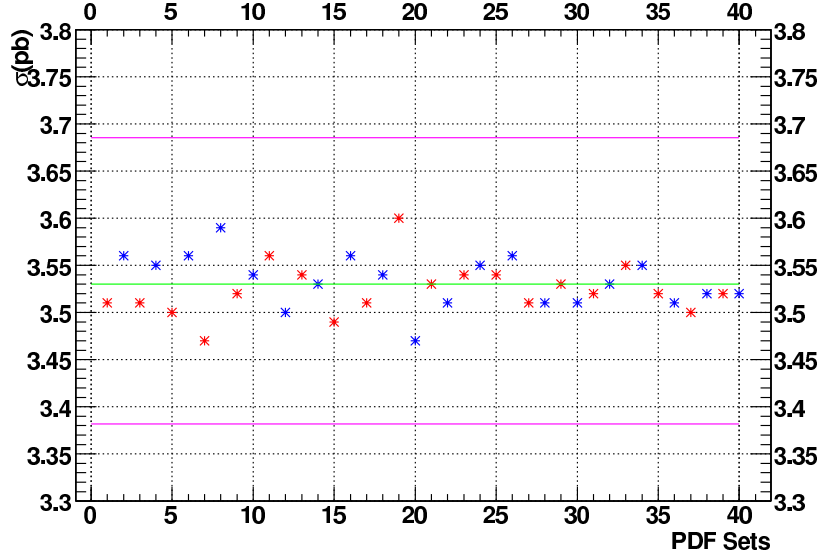


**Figure 5.6:** LHAPDF CTEQ 6L PDF sets and cross section. Green line is the cross section from the PDF central value, pink and light green lines are the uncertainties calculated from the 40 sets.

6L LHAPDF central value. The data points are calculated using the 40 PDF error sets. The PDF uncertainty on the cross section is estimated to be 4%.

The factorization scale,  $Q^2$ , is set to  $\hat{s}$  in the ZGAMMA program. The cross section is calculated using two other values,  $2\hat{s}$  and  $\hat{s}/2$ . The  $Q^2$  uncertainty on the cross section is found to be 1%. The error on the predicted LO SM cross section for  $p\bar{p} \rightarrow l^+l^-\gamma$  production is calculated as the quadrature sum of the estimated PDF and  $Q^2$  uncertainties.

Figure 5.7 shows the  $ll\gamma$  three-body mass distribution from the three contributions to  $Z\gamma$  production [50]. The dashed line is the contribution from the final state radiation (FSR) process, the dotted line is the initial state radiation (ISR) contribution and the solid curve is the total SM (FSR + ISR) contribution. The contribution from anomalous couplings for one illustration example is plotted as the dash-dotted curve. It shows that the high mass region is most sensitive to anomalous couplings. The

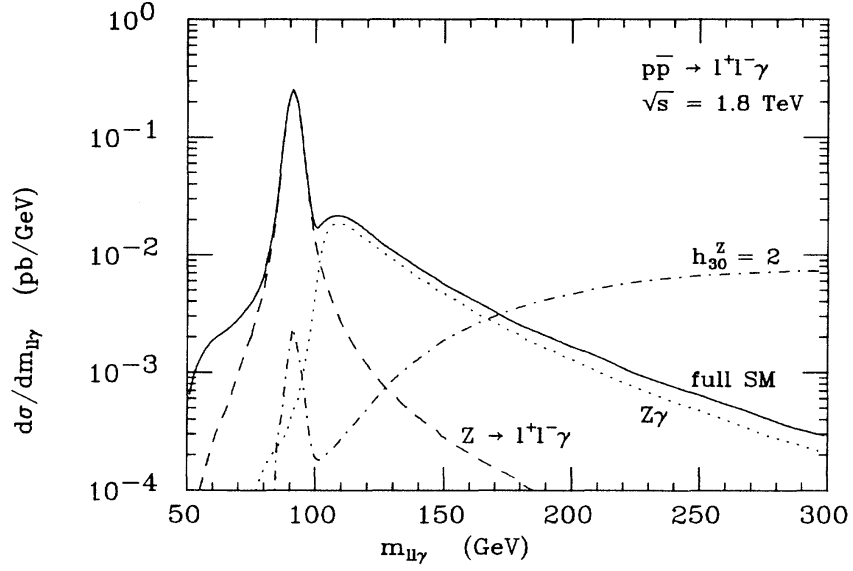


**Figure 5.7:**  $ll\gamma$  Mass distribution in  $Z\gamma$  production [50]. High mass region is most sensitive to anomalous couplings. Solid curve: SM; dash-dotted curve: anomalous couplings.

$ll\gamma$  sample is divided into two regions: FSR dominant region (  $M_{ll\gamma} \leq 100 \text{ GeV}/c^2$  ) and ISR dominant region (  $M_{ll\gamma} > 100 \text{ GeV}/c^2$  ). The high mass region is used to probe anomalous couplings. The LO SM cross section for the ISR dominant region is  $0.91 \pm 0.05 \text{ pb}$ .

### 5.3.2 Next-to-Leading Order (NLO) Corrections

Anomalous couplings at the triple gauge boson vertex will enhance the cross section at large invariant mass. Higher-order ( $O(\alpha_s)$ ) QCD corrections will also enhance the cross section, these corrections must be taken into account in the calculation. Figure 5.8 shows the higher-order contributions to the  $Z\gamma$  production.

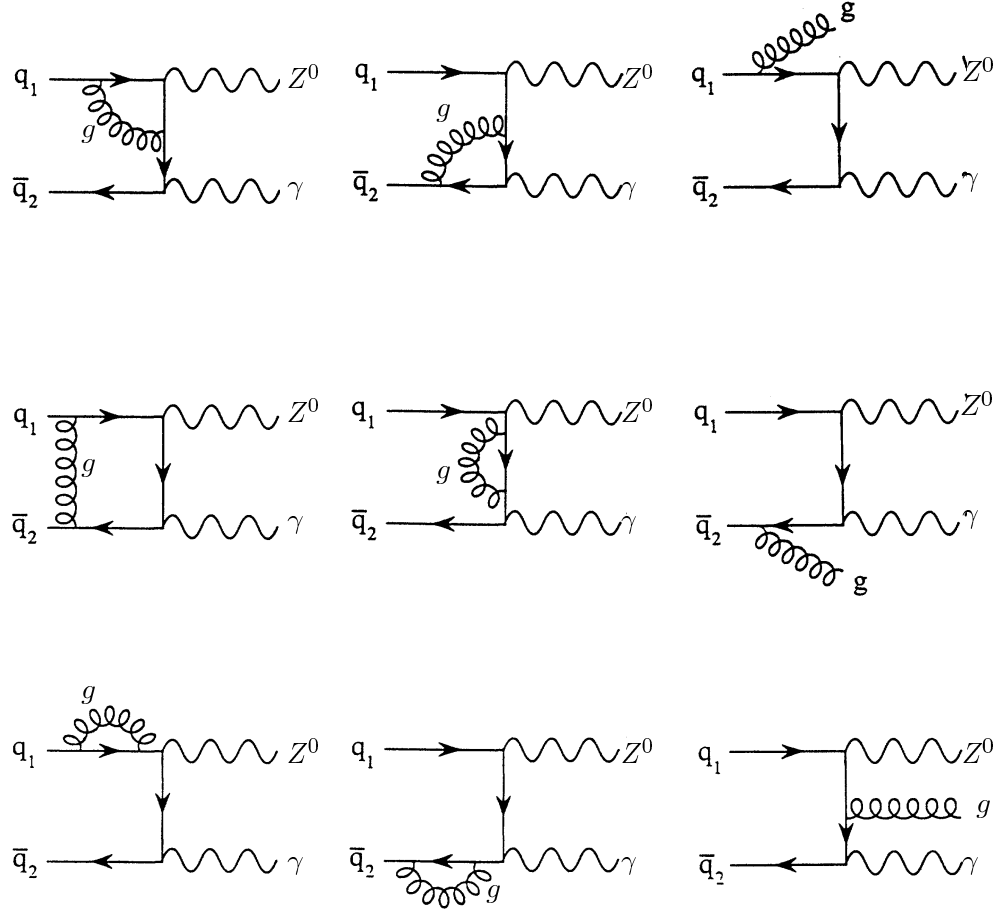


**Figure 5.8:** Higher order QCD corrections (virtual and real gluon emissions) to  $p\bar{p} \rightarrow Z\gamma + X$  production [53]. The diagrams obtained by interchanging the  $Z$  and the  $\gamma$  are not shown.

## K Factor

To take into account the higher-order QCD correction, a k-factor is defined as the ratio of the NLO cross section to the LO cross section:

$$k = \frac{\sigma_{NLO}}{\sigma_{LO}} \quad (5.4)$$

For events generated with LO  $Z\gamma$  program, each event is weighted by this k-factor.

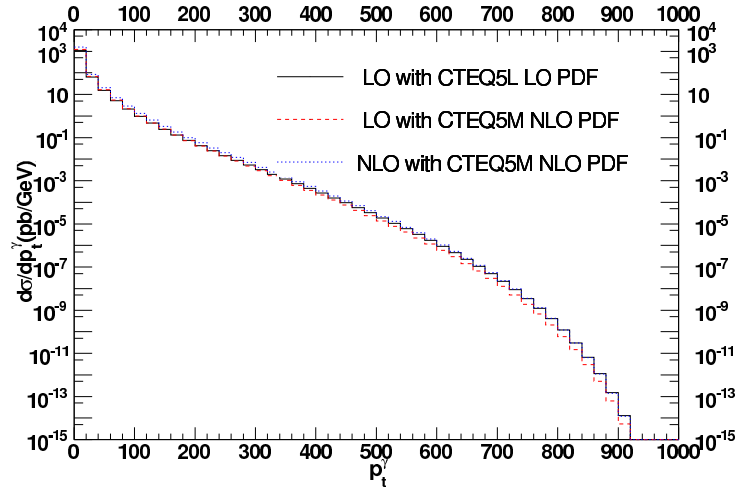
Unlike the LO  $Z\gamma$  program, which includes both the ISR and FSR contributions, the NLO  $Z\gamma$  program does not include the FSR diagrams. For FSR events ( $M_{u\gamma} \leq 100$  GeV/ $c^2$ ), the NLO correction of 1.36 for the inclusive Z production is applied [54].

For ISR events, a  $E_t^\gamma$  dependent k-factor is applied. To match the CTEQ5L [55] PDF used in the LO event generation, the k-factor is calculated as following:

$$k = \frac{\sigma_{NLO}(\text{CTEQ 5M})}{\sigma_{LO}(\text{CTEQ 5L})} \quad (5.5)$$

where the NLO cross section is calculated using the CTEQ5M [55] NLO PDF, and the LO cross section is the Born cross section calculated by the NLO program using CTEQ5L LO PDF.

Figure 5.9 shows the LO and NLO differential cross section distributions as a function of photon  $E_t$ . The solid curve is LO prediction with a LO PDF, and the dashed curve is the LO prediction with a NLO PDF.



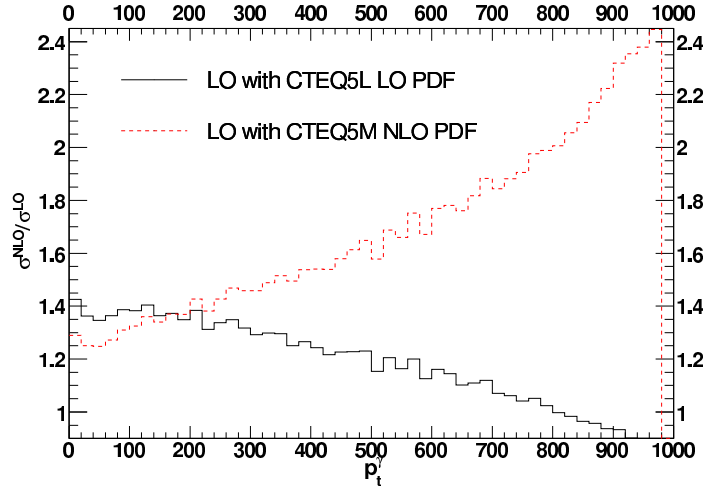
**Figure 5.9:** Photon  $E_t$  distribution. The solid curve is calculated with LO PDF, the dashed curve is with NLO PDF.

Figure 5.10 shows the k-factor as a function of photon  $E_t$ . The solid curve is

calculated as defined in Equation 5.5. For comparison, the dashed line shows a k-factor calculated as following:

$$k = \frac{\sigma_{NLO}(\text{CTEQ5M})}{\sigma_{LO}(\text{CTEQ5M})}, \quad (5.6)$$

which is dramatically different. It is of critical importance that the PDF used in the k-factor calculation match that used in the LO generation of the simulation samples. CTEQ 5L is used in generating all the simulation samples, and thus the k-factor should be calculated as in Equation 5.5.



**Figure 5.10:** The k-factor curves calculated with LO PDF for LO cross section (solid curve) vs NLO PDF for LO cross section (dashed curve).

The k-factor for the SM  $Z\gamma$  production is shown in Figure 5.11 and the functional fit to the k-factor is shown below:

- Fitting function:  $k = p_0 + p_1 * E_t + p_2 * E_t^2$
- $p_0 = 1.33195$ ;
- $p_1 = 7.1025\text{e-}05$ ;

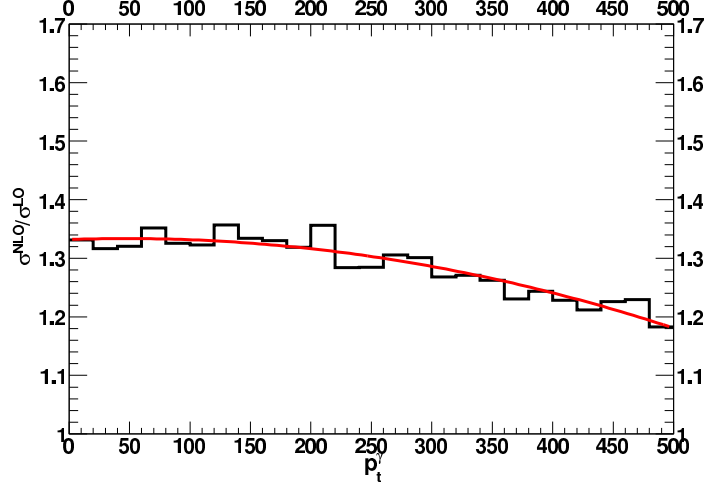


**Figure 5.11:** K-factor. SM:  $h_3^Z=0$  and  $h_4^Z=0$ .

- $p_2 = -7.46387\text{e-}07$ ;

The average k factor is 1.33 for ISR events compared to 1.36 for FSR events. The predicted NLO cross section for the ISR region ( $M_{l\gamma} > 100 \text{ GeV}/c^2$ ) is  $1.2 \pm 0.1 \text{ pb}$ . For the FSR region ( $M_{l\gamma} \leq 100 \text{ GeV}/c^2$ ), the predicted NLO cross section is  $3.3 \pm 0.3 \text{ pb}$ . The total NLO cross section (FSR + ISR) is  $4.5 \pm 0.4 \text{ pb}$ .

Figure 5.12 shows k factor curves from different anomalous gauge couplings. The difference is assigned as a systematic uncertainty on the k factor (see Chapter 10).

## 5.4 Chapter Summary

The triple gauge boson couplings are discussed in this chapter. The cross section for  $p\bar{p} \rightarrow l^+l^-\gamma + X$  is calculated using a LO SM prediction with NLO corrections. The resulting SM cross section for  $p\bar{p} \rightarrow l^+l^-\gamma + X$  at  $\sqrt{s} = 1.96 \text{ TeV}$  is  $4.5 \pm 0.4 \text{ pb}$ . Our measured cross section of  $Z\gamma$  production is compared to this SM prediction in Chapter 9.

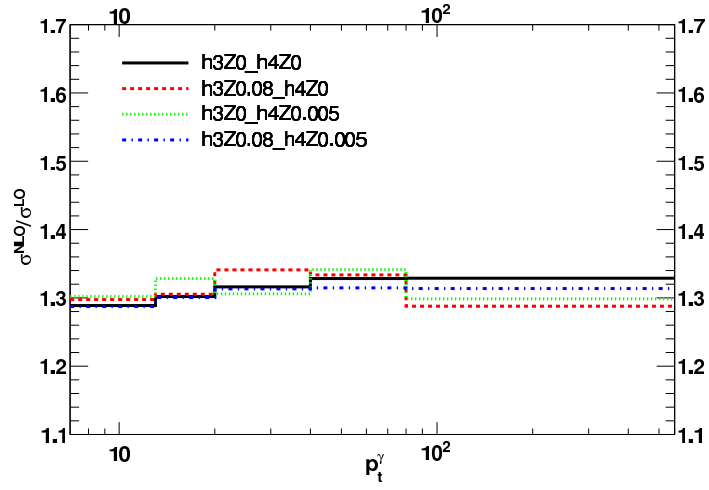


**Figure 5.12:** K factor curves from different anomalous gauge couplings. SM:  $h_3^Z=0$  and  $h_4^Z=0$ . Assign the difference as systematic uncertainty.

# Chapter 6

## Z Boson Event Selection

Z bosons with leptonic decays (with a branch ratio of 3.36% for  $Z \rightarrow ee$  decay) can be selected with very low backgrounds if tight lepton selection cuts are used. However for studies that are limited by statistics, the analyses are better optimized with looser lepton selection cuts, allowing increased backgrounds, but significantly increasing the number of accepted Z bosons. In this chapter, we describe loose electron selection criteria that significantly increase the sample of  $Z \rightarrow ee$  with modest increases in backgrounds. Section 6.1 presents the strategy used for the Z cross section measurement. The datasets selected for this analysis are specified in Section 6.2. Section 6.3 describes electron identification selection cuts. Section 6.4 presents the  $Z \rightarrow ee$  acceptance in the detector. The electron selection efficiency measurement is discussed in Section 6.5. The trigger efficiency measurement is described in Section 6.6. Finally the determination for the QCD background is discussed in Section 6.7. The inclusive Z cross section is measured to validate the Z selection criteria (see Chapter 7). This will be used for the study of  $p\bar{p} \rightarrow e^+e^- + \gamma + X$  production.

### 6.1 Overview of the Measurement of $Z \rightarrow ee$ Cross Section

The signature of high  $E_t$  electrons from Z boson decay is very distinctive in the collider environment. We measure the inclusive Z cross section as a validation of our loose Z selection criteria and various efficiency measurements. The inclusive Z cross section is calculated as described in equation 6.1.



$$\sigma(p\bar{p} \rightarrow Z/\gamma^* + X) \cdot Br(Z/\gamma^* \rightarrow ll) = \frac{N_Z^{\text{obs}} - N_Z^{\text{bck}}}{A_Z \cdot \epsilon_Z \cdot \epsilon_{\text{trig}} \cdot \epsilon_{\text{vtx}} \cdot \int \mathcal{L} dt} \quad (6.1)$$

where:

- $N_Z^{\text{obs}}$  is the number of observed  $Z \rightarrow ee$  candidates in the data.
- $N_Z^{\text{bck}}$  is the number of expected QCD background events where a jet is mis-identified as an electron.
- $A_Z$  is the Z acceptance of the  $Z \rightarrow ee$  decays, defined as the fraction of  $Z \rightarrow ee$  events that satisfy the fiducial and geometric requirements of our detector. This is measured from the SM generation of  $Z \rightarrow ee$  production followed by the CDF detector simulation.
- $\epsilon_Z$  is the total Z selection efficiency, defined as the total efficiency to select two electrons to form a Z boson. This is measured from the data.
- $\epsilon_{\text{trig}}$  is the total trigger efficiency. This is measured from the data.
- $\epsilon_{\text{vtx}} \cdot \int \mathcal{L} dt$  is the effective integrated luminosity.

In this chapter, measurements of the quantities in the above equation are described.

## 6.2 Selection of Datasets

### 6.2.1 High $P_t$ Electron Datasets and Good Run List

The Z boson samples are collected with triggers requiring at least one high  $P_t$  electron candidate in the event. The total integrated luminosity of the data used in this

analysis is  $1.07 \text{ fb}^{-1}$ , collected from February 2002 to February 2006. The datasets and luminosity are listed in table 6.1. Data is processed and analyzed with offline software in a Ntuple data format developed at Duke.

**Table 6.1:** High  $P_t$  electron datasets and the integrated luminosities.

dataset	run range	date	Offline Version	Luminosity( $\text{pb}^{-1}$ )
bhel0d	138425 - 186598	Feb 2002 - Aug 2004	5.3.1	373 +/- 21
bhel0h	190697 - 203799	Dec 2004 - Sep 2005	6.1.2	428 +/- 24
bhel0i	203819 - 212133	Sep 2005 - Feb 2006	6.1.4	274 +/- 16

Events are required to be marked "good" in the Data Quality Monitor good run list (version 13 for Top/EWK/Exotics electron no silicon) [56]. Data collected during the COT compromised period (from Feb 2004 to May 2004) is not included in this analysis.

All selected events are required to fire either the ELECTRON\_CENTRAL\_18 trigger or the Z\_NOTRACK trigger. The definition of the triggers and measurements of the trigger efficiencies are discussed in section 6.6.

## 6.2.2 Detector Simulation Samples

Inclusive  $Z \rightarrow ee$  detector simulation samples ( listed in Table 6.2) are used in the measurements of the Z acceptance, the electron identification efficiencies and scale factors.

**Table 6.2:** Pythia  $Z \rightarrow ee$  MC samples.

dataset	run range	Offline Version	Mee	Number of Events
zewk6d	141544 - 186598	Pythia 5.3.3	$> 20 \text{ GeV}$	3.2 M
zewkad	190753 - 212133	Pythia 6.1.4c	$> 30 \text{ GeV}$	6.7 M

## 6.3 Electron Selection

In this section, the electron selection for the inclusive  $Z \rightarrow ee$  sample is discussed. The requirements for the central ( $|\eta| < 1.1$ ) and plug ( $|\eta| > 1.1$ ) electron identification (ID) are given in section 6.3.1 and 6.3.2, respectively. The energy corrections for the electrons are discussed in section 6.3.3. The measurement of the electron ID efficiency is described in Section 6.5.

### 6.3.1 Central Electron Identification

#### Charged Track Selection

Beam-constrained COT tracks are used in the analysis, where the beam line position is included as an additional constraint in the track fitting. A set of minimum hit criteria is applied to ensure that only high quality tracks are assigned to the electron candidates. Table 6.3 lists the track selection criteria. The COT tracks are required to have at least three axial superlayers and two stereo superlayers, each must have at least five out of twelve possible point measurements. In addition, the interception of the track with the beam axis, called  $z_0$ , must lie within 60 cm of the center of the detector. Figure 6.1 shows the  $z_0$  distribution of the second electron leg in the  $Z \rightarrow ee$  candidate events, where the  $Z$  mass is within the window of (66, 116) GeV, and the first electron is required to pass all the loose central electron identification cuts (see Table 6.4).

#### Central Electron Selection

Table 6.4 lists the selection criteria for a loose central electron (LCE). We apply the loose central electron standard baseline cuts [57], with some modifications. In Table 6.4, the text in bold shows the cut that is different to the standard baseline cut. A

**Table 6.3:** Central electron selection: track quality requirements

Variables	Cut	variable in Duke Ntuple
All COT Tracks:		
# Axial SLs	$\geq 3$ with $\geq 5$ hits per SL	TRACK_trk_nonbc_numHitSL
# Stereo SLs	$\geq 2$ with $\geq 5$ hits per SL	
BC $ z_0 $	$\leq 60$ . cm	TRACK_trk_cotbc_z0

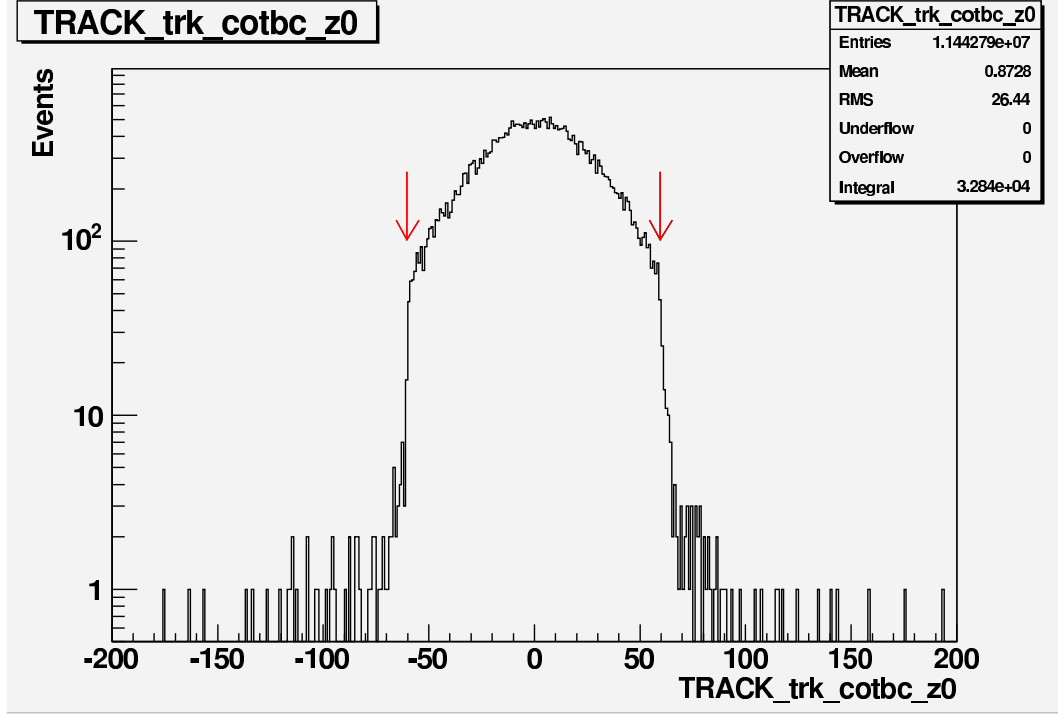


**Figure 6.1:** Track  $z_0$  of the second electron legs in the  $Z \rightarrow ee$  candidate events, with  $66 \text{ GeV}/c^2 < M_Z < 116 \text{ GeV}/c^2$ , and the first electron legs satisfy all the loose central electron identification cuts (see Table 6.4). The arrows show the cuts applied to the  $z_0$  variable.

Lshr cut and a  $\Delta z$  cut are added to the identification cuts so that the loose central electron is a trigger-able object in our Z selection (see section 6.6.1 for more details.). The isolation cut is loosened from 0.1 to 0.3.

The candidate electron clusters are required to lie within the well instrumented central calorimeter regions, corresponding to detector  $|\eta| < 1.1$ . The candidate electrons must have  $E_t \geq 20 \text{ GeV}$  and the COT beam-constrained track  $P_t \geq 10$

GeV/ $c$  (with track curvature corrections [58]).

Details on the electron variables are given below:

- Electron Object:

An electron object is formed from energy clusters in the calorimeter. An electron cluster is made from a seed tower in the electromagnetic calorimeter and a neighboring tower (in  $\eta$ ) in the same calorimeter  $\phi$  wedge.

- $E$  (in GeV):

The total amount of energy is the sum of the electromagnetic and hadronic energy components.

- $E_t$  (in GeV):

$E_t$  is the energy component transverse to the beam line.

- $E_{had}/E_{em}$ :

The electrons deposit most of their energy in the electromagnetic calorimeter, while hadronic particles spread energies into the hadronic calorimeter. To select electron candidates, we require the ratio of the hadronic energies to the electromagnetic energies,  $E_{had}/E_{em} < 0.055 + 0.00045 \cdot E$ , where  $E$  (in GeV) is the total energy in the cluster.

- CES fiducial:

The electrons are required to be reconstructed within the well-instrumented region of the calorimeter. The position of the energy cluster is determined by the CES shower location. The electrons must lie within  $9 \text{ cm} < |Z_{CES}| < 230 \text{ cm}$  and  $|X_{CES}| < 21 \text{ cm}$  for the shower to be fully contained in the active region, where  $X_{CES}$  and  $Z_{CES}$  are the shower's  $x$  and  $z$  positions measured by the CES detector in the CES local coordinate system.

- Calorimeter Isolation Energy (Iso(R=0.4)):

The calorimeter isolation energy is the  $E_t$  sum in a cone of  $\Delta R = \sqrt{\Delta\phi^2 + \Delta\eta^2} < 0.4$  around the electron's seed position of the energy cluster. The energy cluster of the electron is excluded in the calculation of the isolation energy.

- Calorimeter Isolation Energy Ratio (IsoR = Iso/ $E_t$ ):

A cut is applied to the ratio of the isolation energy to the electron  $E_t$  to suppress jet background. For the loose central electron selection, we require  $\text{IsoR} \leq 0.3$ . For the tight central electron selection,  $\text{IsoR} \leq 0.1$  is required.

- Track  $P_t$ :

The highest beam-constrained  $P_t$  of the COT tracks associated with the cluster is required to be larger than 10 GeV/ $c$ .

- $L_{shr}$ , the lateral shower profile:

This variable compares the energy profile of adjacent CEM towers in the cluster to that measured from electron test beam.  $L_{shr} < 0.4$  is required.

- $\Delta z$ :

This is a track-shower matching variable, defined as the distance between the  $z$  position of the CES cluster to the  $z$  position of the extrapolated beam-constrained COT track.  $\Delta z < 8$  cm is required.

To maximize the Z acceptance, the loose central electron identification cuts are used to select  $Z \rightarrow ee$  candidate events in this analysis. For comparison, Table 6.5 lists the selection criteria for tight central electrons(TCE).

### 6.3.2 Plug Electron Identification

In this section, the electron selection in the forward region is discussed.

**Table 6.4:** Event selection: loose central electron(LCE) identification cuts. The text in bold shows the cut that is different to the standard central electron identification cut.

Variables	Cut	variable in Duke Ntuple
Region	CEM ( $ \eta  < 1.1$ )	EMCLST_ele_det==0
COT track	Table 6.3	
$E_t$	$\geq 20$ GeV	EMCLST_ele_std_Et
$TrackP_t$	$\geq 10$ GeV/ $c$	
$E_{had}/E_{em}$	$\leq 0.055 + 0.00045 \cdot E$	EMCLST_ele_std_hadEm
Conversion	not equal 1	CEMCLST_cem_convflag
CES fiducial	= 1	EMCLST_ele_fidEleShrMax
Iso(R=0.4)/ $E_t$	$\leq 0.1$ (standard cut ) $\leq \mathbf{0.3}$ (Loose Isolation cut )	EMCLST_ele_std_calIsoRatio
Lshr	$\leq 0.4$	CEMCLST_cem_std_lshr
$ \Delta z $	$\leq 8$ <b>cm</b>	CEMCLST_cem_std_deltaZ

**Table 6.5:** Electron selection: tight central electron (TCE) identification cuts

Variables	Cut	variable in Duke Ntuple
All COT Tracks:		
# Axial SLs	$\geq 3$ with $\geq 5$ hits per SL	TRACK_trk_nonbc_numHitSL
# Stereo SLs	$\geq 2$ with $\geq 5$ hits per SL	
BC $ z_0 $	$\leq 60$ .	TRACK_trk_cotbc_z0
Region	CEM ( $ \eta  < 1.1$ )	EMCLST_ele_det==0
$E_t$	$\geq 20$ GeV	EMCLST_ele_std_Et
$TrackP_t$	$\geq 10$ GeV/ $c$	
$E_{had}/E_{em}$	$\leq 0.055$ $+ 0.00045 \cdot E$	EMCLST_ele_std_hadEm
Conversion	not equal 1	CEMCLST_cem_convflag
CES fiducial	= 1	EMCLST_ele_fidEleShrMax
Iso(R=0.4)/ $E_t$	$\leq 0.1$	EMCLST_ele_std_calIsoRatio
Lshr	$\leq 0.2$	CEMCLST_cem_std_lshr
$E/p$ (for $P_t < 50$ )	$\leq 2.0$	CEMCLST_cem_std_EOverP
$ \Delta z $	$\leq 3$ cm	CEMCLST_cem_std_deltaZ
$Q \cdot \Delta x$	$\geq -3.0$ cm, $\leq 1.5$ cm	CEMCLST_cem_std_qDeltaX
$\chi^2_{strips}$	$\leq 10.0$ cm	CEMCLST_cem_std_cesStripChi

## Plug Electron identification Variables

The standard loose plug electron identification cuts are listed in Table 6.6.

In the loose plug electron selection(LPE) used in this analysis, the PEM 3x3 chi2 cut is loosed from 10 to 25 (see [59] for more details). And  $\eta$  coverage is extended from 2.0 to 2.8. The selection criteria is listed in Table 6.7.

**Table 6.6:** The standard loose plug electron identification cuts.

Variables	Cut	variable in Duke Ntuple
Region	PEM ( $1.1 \leq  \eta  < 3.6$ )	EMCLST_ele_det==1
PES 2D Eta	$1.2 \leq  \eta  \leq 2.0$	PEMCLST_pem_pes2dGlobalEta
$CorrE_t$	$\geq 20$ GeV	
$E_{had}/E_{em}$	$\leq 0.05$	EMCLST_ele_std_hadEm
PEM 3x3 chi2	$\leq 10.$	PEMCLST_pem_std_pem3x3Chi
Iso(R=0.4)/ $E_t$	$\leq 0.1$	EMCLST_ele_std_calIsoRatio

**Table 6.7:** The loose plug electron (LPE) identification cuts in this analysis, the text in bold shows the cut that is different to the standard electron identification cut.

Variables	Cut	variable in Duke Ntuple
Region	PEM ( $1.1 \leq  \eta  < 3.6$ )	EMCLST_ele_det==1
PES 2D Eta	$1.2 \leq  \eta  \leq \mathbf{2.8}$	PEMCLST_pem_pes2dGlobalEta
$CorrE_t$	$\geq 20$ GeV	
$E_{had}/E_{em}$	$\leq 0.05$	EMCLST_ele_std_hadEm
PEM 3x3 chi2	$\leq \mathbf{25.}$	PEMCLST_pem_std_pem3x3Chi
Iso(R=0.4)/ $E_t$	$\leq 0.1$ (Standard cut )	EMCLST_ele_std_calIsoRatio
	$\leq \mathbf{0.3}$ ( loose isolation cut )	

Details on the plug electron variables are given below:

- E: Plug Electron Energy (in GeV)

The energy is calculated with 2x2 clustering algorithm.



- CorrE: Corrected Plug Electron Energy (in GeV)

The position dependent face correction, the energy deposited in the Plug Pre-Radiate detector (PPR) and the leakage energy into the neighboring towers are added to the 2x2 energy to get the total energy. More details on reconstructing plug electron energy are given in [60].

- PES 2D  $\eta$

The detector  $\eta$  of the electron shower measured by the Plug Electromagnetic ShowerMax detector (PES).

- PEM 3x3  $\chi^2$

This is a  $\chi^2$  comparison of the energy distribution of the electron cluster in the 3x3 blocks of towers around the seed tower to the distribution measured from test beam data.

- PES 5x9 U/V

The two layers (called U and V) of the PES detector provide two-dimensional position measurement. A 5x9 ratio is used to describe the shape of the energy cluster. The ratio is measured as the energy deposited in a 5 wire window to that in a 9 wire window ( the 5 wire plus two additional wires in each side). The PES 5x9 ratio is required to be more than 0.65 for both the U and V wires.

- $\Delta R$

This is the distance between the 2d position measured by the PES detector to that measured by the PEM calorimeter. This is calculated as:

$$\Delta R = \sqrt{(pes_x - pem_x)^2 + (pes_y - pem_y)^2}$$

**Table 6.8:** Tight plug electron(TPE) identification cuts used in this analysis , the text in bold shows the cut that is different to the standard electron identification cut.

Variables	Cut	variable in Duke Ntuple
Region	PEM ( $1.1 \leq  \eta  < 3.6$ )	EMCLST_ele_det==1
PES 2D Eta	$1.2 \leq  \eta  \leq \mathbf{2.8}$	PEMCLST_pem_pes2dGlobalEta
$CorrE_t$	$\geq 20$ GeV	
$E_{had}/E_{em}$	$\leq 0.05$	EMCLST_ele_std_hadEm
PEM 3x3 $\chi^2$	$\leq \mathbf{25.}$	PEMCLST_pem_std_pem3x3Chi
PES 5x9 U	$\geq 0.65$	PEMCLST_pem_pesU5x9ProfRat
PES 5x9 V	$\geq 0.65$	PEMCLST_pem_pesV5x9ProfRat
$\Delta R$	$\leq 3.0$ cm	$\sqrt{(pes_x - pem_x)^2 + (pes_y - pem_y)^2}$
Iso(R=0.4)/ $E_t$	$\leq 0.1$	EMCLST_ele_std_callIsoRatio

**Table 6.9:** Standard tight plug electron identification cuts.

Variables	Cut	variable in Duke Ntuple
Region	PEM ( $1.1 \leq  \eta  < 3.6$ )	EMCLST_ele_det==1
PES 2D Eta	$1.2 \leq  \eta  \leq 2.0$	PEMCLST_pem_pes2dGlobalEta
$CorrE_t$	$\geq 20$	
$E_{had}/E_{em}$	$\leq 0.05$	EMCLST_ele_std_hadEm
PEM 3x3 $\chi^2$	$\leq 10.$	PEMCLST_pem_std_pem3x3Chi
PES 5x9 U	$\geq 0.65$	PEMCLST_pem_pesU5x9ProfRat
PES 5x9 V	$\geq 0.65$	PEMCLST_pem_pesV5x9ProfRat
$\Delta R$	$\leq 3.0$	$\sqrt{(pes_x - pem_x)^2 + (pes_y - pem_y)^2}$
Iso(R=0.4)/ $E_t$	$\leq 0.1$	EMCLST_ele_std_callIsoRatio

The tight plug electron (TPE) identification cuts used in this analysis are listed in table 6.8. For comparison, the standard Tight Plug Electron identification cuts are listed in Table 6.9.

### 6.3.3 Electron energy correction

In this section, the electron energy corrections are discussed.

The invariant di-lepton mass plots for data and event simulation are shown in Figure 6.2. The events are normalized, such that there are the same number of

events within the mass window  $86\text{--}98\text{ GeV}/c^2$ . As can be seen from the plots, the Z mass peak of data and simulation are not at  $91\text{ GeV}/c^2$  (the Z boson mass). We apply energy correction factors to both the data and the simulation, to bring the Z mass peak positions to  $91\text{ GeV}/c^2$ . To get a clean data sample, the electrons are required to satisfied the tight selection cuts listed in table 6.5 and table 6.8. A Gaussian fit with a window of  $86\text{--}98\text{ GeV}/c^2$  is used. Energy correction factors are extracted so that the mean values of the Gaussian fits are at the Z mass of  $91\text{ GeV}/c^2$ . There are small variations for the three datasets (0d, 0h and 0i) and we scale them differently. Figure 6.3 compares the scaled mass spectra of data and simulation, both now are peaked at  $91\text{ GeV}/c^2$ .

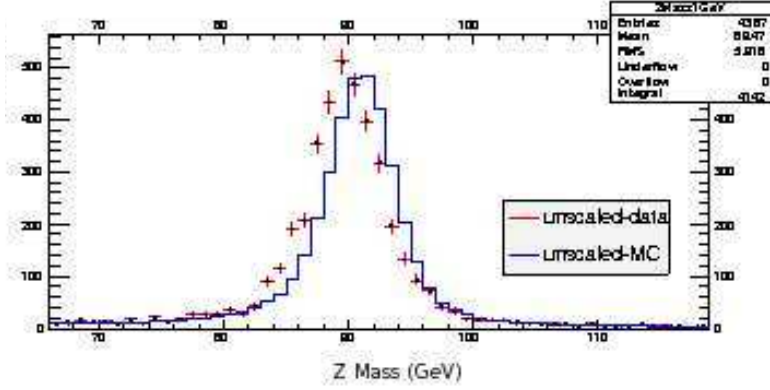


**Figure 6.2:** Unscaled di-electron mass spectra, data vs simulation.

The Z peak positions from the unscaled data (dataset bhe0d) and simulation samples (dataset zewk6d) are listed in table 6.10. The energy scale factors are listed in table 6.11. Details on the energy scale factors are given in reference [60].

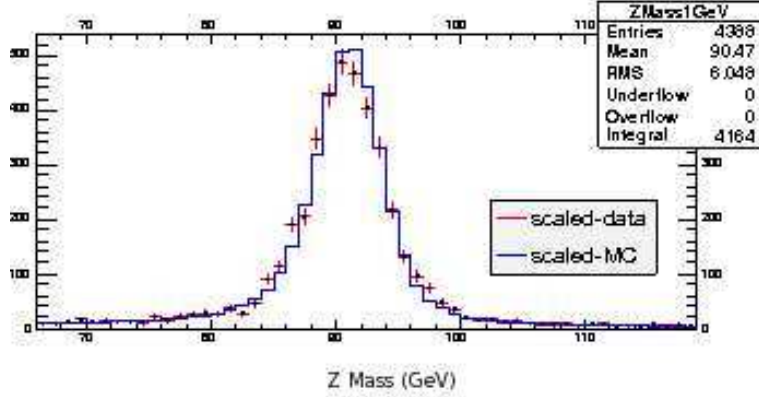


**Figure 6.3:** Scaled di-electron mass spectra, data vs simulation.

**Table 6.10:** Z Peak positions from the unscaled data and simulation samples

Region	Data	Simulation
Central-Central	$91.01 \pm 0.04$	$91.44 \pm 0.01$
Central-Plug		
West( $ \eta  < 1.78$ )	$89.92 \pm 0.07$	$91.01 \pm 0.01$
West( $ \eta  \geq 1.78$ )	$89.76 \pm 0.09$	$90.51 \pm 0.02$
East( $ \eta  < 1.78$ )	$89.67 \pm 0.09$	$90.98 \pm 0.01$
East( $ \eta  \geq 1.78$ )	$89.54 \pm 0.10$	$90.54 \pm 0.02$
Plug-Plug	$88.36 \pm 0.11$	$90.35 \pm 0.01$

**Table 6.11:** Energy scale factors

Region	Data	MC
Central	no correction	0.995
Plug		
West( $ \eta  < 1.78$ )	1.024	1.005
West( $ \eta  \geq 1.78$ )	1.028	1.016
East( $ \eta  < 1.78$ )	1.030	1.005
East( $ \eta  \geq 1.78$ )	1.033	1.015

## 6.4 Acceptance

In this section, the  $Z \rightarrow ee$  acceptance in different detector regions is discussed.

### 6.4.1 Detector Simulation Samples

The  $Z \rightarrow ee$  detector simulation samples are used to study the signal acceptance. The datasets and run ranges are listed in table 6.2.

### 6.4.2 Acceptance in the CC Region

We measure the fraction of  $Z$  events that pass the geometry and kinematic requirements in the CC channel, where both electron legs from the  $Z$  boson decay are in the central region ( $|\eta| \leq 1.1$ ). Events with the primary event vertex outside 60.0 cm of the detector origin along the beam line, are removed from both the numerator and denominator. The selection efficiency of the event vertex requirement is measured separately (see Section 7.2).

We measure the inclusive  $\gamma^*/Z \rightarrow ee$  cross-section in the invariant mass range  $66 \text{ GeV}/c^2 \leq M_{ee} \leq 116 \text{ GeV}/c^2$ . The simulated  $Z \rightarrow ee$  samples used to measure the acceptance are generated with a minimum invariant mass of  $20 \text{ GeV}/c^2$  ( $30 \text{ GeV}/c^2$  for zewkad dataset). The invariant mass of the di-lepton at the generator level is required to lie within the mass range  $66 \text{ GeV}/c^2 \leq M_{ee}(\text{Gen}) \leq 116 \text{ GeV}/c^2$ . Events generated outside our allowed range do not contribute to the denominator, but can contribute to the numerator due to the effects of radiative and detector resolution. Therefore, the invariant mass requirement at the generator level is only applied to the denominator, not the numerator.

Table 6.12 gives the acceptance of  $Z \rightarrow ee$  events in the CC region for 0d dataset. Events are required to have at least two EM clusters in the central region that satisfies the corresponding selection criteria listed in the table 6.12. The reconstructed invariant mass is required to lie within the mass window  $66 \text{ GeV}/c^2 \leq M_{ee}(\text{Rec}) \leq 116 \text{ GeV}/c^2$ .

In addition, the reconstructed electrons are required to match the electrons at the generator level. The matching requirement is:  $\Delta R(e_{Gen}, e_{Rec}) < 0.05$ .

**Table 6.12:**  $Z \rightarrow ee$  CC channel Selection Acceptance. zewk6d MC

Selection Criteria	Number of Events	Net Acceptance
Total Events	3.22568e+06	-
Good Run	3.11168e+06	-
$ Z_{vtx}  \leq 60$ cm	3.01684e+06	-
$66 \text{ GeV}/c^2 \leq M_{ee}(\text{Gen}) \leq 116 \text{ GeV}/c^2$ (Gen Mass cut on denominator only)	1.54163e+06	-
Central EM Cluster ( det = 0)	1.85913e+06	1.206
Calorimeter Fiducial Cuts	1.62556e+06	1.054
Electron Track $P_t \geq 10 \text{ GeV}/c$	1.16091e+06	0.753
EM Cluster $E_t \geq 20 \text{ GeV}$	873291	0.5665
Second Central EM Cluster ( det = 0)	592372	0.3843
Second Calorimeter Fiducial Cuts	412936	0.2679
Second Electron Track $P_t \geq 10 \text{ GeV}/c$	229857	0.1491
Second EM Cluster $E_t \geq 20 \text{ GeV}$	189263	0.1228
Two EM Cluster	189263	0.1228
$66 \text{ GeV}/c^2 \leq M_{ee}(\text{Rec}) \leq 116 \text{ GeV}/c^2$	176386	0.1144
OS	173441	0.1125
$ VertexZ  \leq 60$ cm	173310	0.1124
Matching HEPG( $\Delta R \leq 0.05$ )	172339	0.1118
Trigger Efficiency Weighted ( $\epsilon = 100\%$ )	172332	0.1118

The dataset zewkad is used to calculate acceptance for 0h and 0i dataset. The acceptance for selecting  $Z \rightarrow ee$  events with two central electrons is  $0.1118 \pm 0.0002$ .

### 6.4.3 Acceptance in the CP Region

We measure the fraction of  $Z$  events that pass the geometry and kinematic requirements in the CP channel, where the first electron leg from the  $Z$  boson decay is in the central region( $|\eta| \leq 1.1$ ) and the second electron leg is in the plug region( $1.2 \leq |\eta| \leq 2.8$ ).

Table 6.13 gives the acceptance of  $Z \rightarrow ee$  events in CP region for 0d dataset.

Events are required to have at least one EM cluster in central region and one EM cluster in plug region that satisfies the corresponding selection criteria listed in the table 6.13.

**Table 6.13:**  $Z \rightarrow ee$  CP channel Selection Acceptance. Statistical uncertainties are shown. Using zewk6d MC sample, 0d dataset run range.

Selection Criteria	Number of Events	Net Acceptance
Total Events	3225677	-
Good Run	3111683	-
$ Z_{vtx}  \leq 60$ cm	3016836	-
$66 \text{ GeV}/c^2 \leq M_{ee}(\text{Gen}) \leq 116 \text{ GeV}/c^2$ (Gen Mass cut on denominator only)	1541630	-
Central EM Cluster ( det = 0)	1859126	$1.2059 \pm \text{nan}$
Calorimeter Fiducial Cuts	1625563	$1.0544 \pm \text{nan}$
Electron Track $P_t \geq 10 \text{ GeV}/c$	1160908	$0.7530 \pm 0.0003$
EM Cluster $E_t \geq 20 \text{ GeV}$	873291	$0.5665 \pm 0.0004$
Plug EM Cluster ( det = 1)	534530	$0.3467 \pm 0.0004$
PES2dGlobalEta ( $1.20 \leq  \eta  \leq 2.80$ )	431764	$0.2801 \pm 0.0004$
Plug EM Cluster $E_t \geq 20 \text{ GeV}$	378551	$0.2456 \pm 0.0003$
Plug EM Cluster $Had/EM \leq 0.125$	377399	$0.2448 \pm 0.0003$
Two EM Cluster	377399	$0.2448 \pm 0.0003$
$66 \text{ GeV}/c^2 \leq M_{ee}(\text{Rec}) \leq 116 \text{ GeV}/c^2$	362040	$0.2348 \pm 0.0003$
$ VertexZ  \leq 60$ cm	361707	$0.2346 \pm 0.0003$
Matching HEPG( $\Delta R \leq 0.05$ )	354255	$0.2298 \pm 0.0003$
Trigger Efficiency Weighted ( $\epsilon = 99.6\%$ )	352802	$0.2288 \pm 0.0003$

The acceptance for selecting  $Z \rightarrow ee$  events with one central and one plug electron is  $0.2288 \pm 0.0003$ .

#### 6.4.4 Correction for slow trigger efficiency turning on at low $P_t$

There is a slow turn-on of the trigger efficiency at the low  $P_t$  region. To correct for the effect of this slow turn-on, a trigger efficiency weight is applied to detector simulation event by event when calculating the signal acceptance. See section 6.6 for details of the correction.

## 6.5 Electron identification Efficiency Measurement

### 6.5.1 Central Electron Identification Efficiencies

The central electron identification efficiency is measured from data following the method described in in CDF note 7950, "Electron Identification in Offline Release 6.1.2" [61].

We measure the central electron identification efficiency as the fraction of electrons passing the central electron identification selection cuts (table 6.4). All electrons are required to satisfy the acceptance requirements listed in table 6.12. The electron identification efficiency is defined as:

$$\epsilon = \frac{\text{electrons passing detection selection cuts}}{\text{electrons within detector fiducial and geometric region}}$$

To reduce background in our sample, we require at least one central electron in the event passing the tight selection cuts listed in table 6.5. Events with more than two central electrons are vetoed. To further reduce background, a tight invariant mass cut of  $75 \text{ GeV}/c^2 \leq M_{ee} \leq 105 \text{ GeV}/c^2$  is applied. The two electrons in the events must have opposite sign charges.

The electron counting method [61] is used to select an unbiased electron sample. This method looks for probe electrons which makes a Z with an electron that passes the identification and trigger requirements. If both electrons of the Z event pass the trigger and loose central electron(LCE) requirements, both are counted as probe electrons. If only one pass the trigger and LCE requirements, only the probe electron it makes a Z with is counted. Let  $N_{probe}$  be the number of probe electrons, and  $N_{lid}$  the number of electrons passing the loose central electron identification requirements, the efficiency for the loose central electron selection is given as:



$$\epsilon_{lid} = \frac{N_{lid}}{N_{probe}}$$

We measure the efficiency in the following order: loose identification efficiency  $\epsilon_{lid}^{cen}$ ; loose isolation (IsoR < 0.3) efficiency  $\epsilon_{liso}^{cen}$ ; tight isolation (IsoR < 0.1) efficiency  $\epsilon_{tiso}^{cen}$ ; and tight identification efficiency  $\epsilon_{tid}^{cen}$ . The electron candidates used to measure each group of selection efficiency are required to pass all the selection requirements ordered prior the one being measured. For example, to measure the efficiency of the tight central electron (TCE) identification requirement, the probe electrons must pass the loose central electron identification requirements and the tight isolation requirement.

Assuming the signs of background electrons are uncorrelated, the number of background events can be determined from the number of same sign events. However, the same sign events include contribution from the trident events where a hard photon is radiated off an electron and then converts into an electron-positron pair, thus the events appear to have two same sign electrons. The same-sign Z events with trident correction are used to determine the background. The background is given as:

$$N^{bkg} = N_{Data}^{SS} - N_{Data}^{OS} \times N_{MC}^{SS}/N_{MC}^{OS},$$

where  $N_{MC}^{SS}$  ( $N_{MC}^{OS}$ ) is number of same-sign (opposite-sign) events in the  $Z \rightarrow ee$  simulation sample. The ratio  $N_{MC}^{SS}/N_{MC}^{OS}$  is the fraction of trident events in the  $Z \rightarrow ee$  sample.

The efficiency with background subtraction is then:

$$\epsilon_{lid} = \frac{N_{lid} - N_{lid}^{bkg}}{N_{probe} - N_{probe}^{bkg}}$$

Table 6.14 lists the input parameters to central electron identification and isolation efficiency measurements using CC  $Z \rightarrow ee$  candidate events for one dataset (bhel0d). The scale factor, defined as the ratio of the efficiency measured in the data to that in the simulation sample, is presented. All scale factors are very close to 1.00, indicating the high quality of the CDF detector simulation.

**Table 6.14:** Input parameters to central electron identification and isolation efficiency measurements using number of electrons in central-central  $Z \rightarrow ee$  candidates. bhel0d dataset

Data						
Efficiency Measurement	Symbol	# of Probe	# passing Selection	Probe Ele Bkg	Passing Ele Bkg	Eff Data
Loose ID	$\epsilon_{\text{lid}}^{\text{cen}}$	18516	17704	143.9	40.3	0.961
Loose Iso	$\epsilon_{\text{liso}}^{\text{cen}}$	17651	17598	37.9	35.4	0.997
Tight Iso	$\epsilon_{\text{tiso}}^{\text{cen}}$	17249	16900	34.7	33.9	0.980
Tight ID	$\epsilon_{\text{tid}}^{\text{cen}}$	15007	13114	23.6	13.1	0.874
MC						
Efficiency Measurement	Symbol	# of Probe	# passing Selection	Efficiency MC	SF(Data/MC)	
Loose ID	$\epsilon_{\text{lid}}^{\text{cen}}$	305308	292748	0.959	1.003	
Loose Iso	$\epsilon_{\text{liso}}^{\text{cen}}$	291989	291230	0.997	1.000	
Tight Iso	$\epsilon_{\text{tiso}}^{\text{cen}}$	285757	280284	0.981	0.999	
Tight ID	$\epsilon_{\text{tid}}^{\text{cen}}$	250807	221330	0.882	0.991	

The total isolation cut efficiency for a central electron with  $\text{IsoR} < 0.1$  is:

$$\epsilon_{\text{liso}}^{\text{Cen}} * \epsilon_{\text{tiso}}^{\text{Cen}} (\text{Data}) = 0.977$$

$$\epsilon_{\text{liso}}^{\text{Cen}} * \epsilon_{\text{tiso}}^{\text{Cen}} (\text{MC}) = 0.978$$

The total selection efficiency for a tight central electron is :

$$\epsilon_{\text{lid}}^{\text{Cen}} * \epsilon_{\text{liso}}^{\text{Cen}} * \epsilon_{\text{tiso}}^{\text{Cen}} * \epsilon_{\text{tid}}^{\text{Cen}} (\text{Data}) = 0.821$$

$$\epsilon_{\text{lid}}^{\text{Cen}} * \epsilon_{\text{liso}}^{\text{Cen}} * \epsilon_{\text{tiso}}^{\text{Cen}} * \epsilon_{\text{tid}}^{\text{Cen}} (\text{MC}) = 0.828$$

And total scale factor for a tight central electron is :

$$SF_{\text{lid}}^{\text{Cen}} * SF_{\text{liso}}^{\text{Cen}} * SF_{\text{tiso}}^{\text{Cen}} * SF_{\text{tid}}^{\text{Cen}} = 0.992$$

The electron identification uncertainties and effects on cross section measurements are discussed in Chapter 9.

### Central Electron identification Efficiency, $1\text{ fb}^{-1}$

The efficiencies and scale factors for the full  $1\text{ fb}^{-1}$  dataset are summarized in table 6.5.1. The full dataset is further divided into three periods (bhel0d/0h/0i datasets) to look at the time variation of the scale factors. The efficiencies measured from data and simulation samples are listed. As can be seen in the table, the efficiencies predicted from the detector simulation agree well with the efficiencies measured from data. The efficiency correction factors are close to 1.00.

**Table 6.15:** The efficiencies and scale factors for central electron, bhel0d/0h/0i dataset.

dataset	Efficiency	Data	MC	Scale Factor
bhel0d	Loose ID	0.961	0.959	1.003
	Loose Iso	0.997	0.997	1.000
	Tight Iso	0.980	0.981	0.999
	Tight ID	0.874	0.882	0.991
bhel0h	Loose ID	0.957	0.958	0.999
	Loose Iso	0.997	0.997	1.000
	Tight Iso	0.977	0.979	0.998
	Tight ID	0.871	0.884	0.985
bhel0i	Loose ID	0.953	0.957	0.996
	Loose Iso	0.997	0.997	1.000
	Tight Iso	0.978	0.977	1.001
	Tight ID	0.868	0.883	0.983

### 6.5.2 Plug Electron identification Efficiency

We measure the plug electron identification efficiency as the fraction of electrons passing the plug electron identification selection cuts (Table 6.7). All electrons are

required to satisfy the acceptance requirements listed in Table 6.13. To reduce background in our sample, we require the central electron in the event passing the tight selection cuts listed in Table 6.5. Events with more than one central and one plug electron are vetoed. To further reduce background, a tight invariant mass cut of  $75 \text{ GeV}/c^2 \leq M_{ee} \leq 105 \text{ GeV}/c^2$  is applied. As in the central identification efficiency measurement, we measure the plug identification efficiency in the following order: loose identification, loose iso, tight iso and tight identification. The efficiency is determined as:

$$\epsilon_i = \frac{N_{\text{TCEM}_i}}{N_{\text{TCEM}_P}},$$

where:

- $N_{\text{TCEM}_A}$  is the number of events that satisfy the requirements mentioned above, where there is a tight central electron in the event, and the plug electron passes the acceptance requirement, and the invariant mass lies within the window of  $75 \text{ GeV}/c^2 \leq M_{ee} \leq 105 \text{ GeV}/c^2$ .
- $N_{\text{TCEM}_i}$  is a subset of events from  $N_{\text{TCEM}_A}$ . In addition, the plug electron satisfies the  $i$ th selection criteria.
  - $i=0$ : plug loose ID (table 6.7)
  - $i=1$ : loose isolation cut ( $\text{IsoR} < 0.3$ )
  - $i=2$ : tight isolation cut ( $\text{IsoR} < 0.1$ )
  - $i=3$ : plug tight ID (table 6.8)
- $N_{\text{TCEM}_P}$  is a subset of events from  $N_{\text{TCEM}_A}$ ,

- i=0:  $N_{\text{TCEM.P}} = N_{\text{TCEM.A}}$ ;
- i=1, 2, 3:  $N_{\text{TCEM.P}} = N_{\text{TCEM.(i-1)}}$ .

### Total Plug identification Efficiency for one dataset (bhel0d)

Table 6.16 lists the input parameters to plug electron ID and isolation efficiency measurements using CP  $Z \rightarrow ee$  candidate events for one dataset (bhel0d). The scale factor of data to detector simulation, SF(Data/MC) is also presented in Table 6.16.

**Table 6.16:** Input parameters to plug electron identification and isolation efficiency measurements using central-plug  $Z \rightarrow ee$  candidates for one dataset (bhel0d) .

Data						
Efficiency Measurement	Symbol	# of Probe	# passing Selection	Probe Ele Bkg	Passing Ele Bkg	Eff
Loose ID	$\epsilon_{\text{lid}}^{\text{plug}}$	17554	15829	468.1	93.9	0.921
Loose Iso	$\epsilon_{\text{liso}}^{\text{plug}}$	15829	15797	93.9	94.2	0.998
Tight Iso	$\epsilon_{\text{tiso}}^{\text{plug}}$	15797	15438	94.2	81.8	0.978
Tight ID	$\epsilon_{\text{tid}}^{\text{plug}}$	15438	14898	81.8	73.4	0.965
MC						
Efficiency Measurement	Symbol	# of Probe	# passing Selection	Efficiency	SF(Data/MC)	
Loose ID	$\epsilon_{\text{lid}}^{\text{plug}}$	287108	269665	0.939	0.981	
Loose Iso	$\epsilon_{\text{liso}}^{\text{plug}}$	269665	269355	0.999	0.999	
Tight Iso	$\epsilon_{\text{tiso}}^{\text{plug}}$	269355	265652	0.986	0.992	
Tight ID	$\epsilon_{\text{tid}}^{\text{plug}}$	265652	260565	0.981	0.984	

The total isolation cut efficiency for a plug electron with  $\text{IsoR} < 0.1$  is:

$$\epsilon_{\text{liso}}^{\text{plug}} * \epsilon_{\text{tiso}}^{\text{plug}} (\text{Data}) = 0.976, \quad \epsilon_{\text{liso}}^{\text{plug}} * \epsilon_{\text{tiso}}^{\text{plug}} (\text{MC}) = 0.985$$

The total selection efficiency for a tight plug electron is :

$$\epsilon_{\text{lid}}^{\text{plug}} * \epsilon_{\text{liso}}^{\text{plug}} * \epsilon_{\text{tiso}}^{\text{plug}} * \epsilon_{\text{tid}}^{\text{plug}} (\text{Data}) = 0.868$$

$$\epsilon_{\text{lid}}^{\text{plug}} * \epsilon_{\text{liso}}^{\text{plug}} * \epsilon_{\text{tiso}}^{\text{plug}} * \epsilon_{\text{tid}}^{\text{plug}} (\text{MC}) = 0.908$$

And the total scale factor for a tight plug electron is : 0.956

Side-band subtraction method is used to determine the background in the CP event selection. Detail of the method is discussed in 6.7.2.

### Total Plug identification Efficiency, $1\text{fb}^{-1}$

The efficiencies and scale factors for the full  $1\text{fb}^{-1}$  dataset are summarized in table 6.5.2. As in the central electron measurement, the full dataset is further divided into three periods (bhel0d/0h/0i datasets) to look at the time variation of the scale factors. The efficiencies predicted from the detector simulation agree well with the efficiencies measured from data. The efficiency scale factors are close to 1.00.

**Table 6.17:** The efficiencies and scale factors for plug electron, bhel0d/0h/0i dataset.

dataset	Efficiency	Data	MC	Scale Factor
bhel0d	Loose ID	0.921	0.939	0.981
	Loose Iso	0.998	0.999	0.999
	Tight Iso	0.978	0.986	0.992
	Tight ID	0.965	0.981	0.984
bhel0h	Loose ID	0.912	0.930	0.981
	Loose Iso	0.999	0.999	1.000
	Tight Iso	0.970	0.983	0.987
	Tight ID	0.970	0.978	0.992
bhel0i	Loose ID	0.905	0.927	0.977
	Loose Iso	0.998	0.999	1.000
	Tight Iso	0.969	0.980	0.988
	Tight ID	0.968	0.978	0.990

## 6.6 Trigger Efficiency

Two triggers, ELECTRON\_CENTRAL\_18 trigger and Z\_NOTRACK trigger, are used in the analysis. In the inclusive Z and  $Z\gamma$  event selection, either ELEC-

TRON\_CENTRAL\_18 trigger or Z\_NOTRACK trigger is required to be fired.

Details on the ELECTRON\_CENTRAL\_18 trigger efficiency measurement are given in section 6.6.1. The Z\_NOTRACK trigger efficiency measurement is given in section 6.6.2. In section 6.6.3, the total trigger efficiencies in the Z and  $Z\gamma$  event selection are calculated. The total trigger efficiencies from the data are found to be very close to 100%.

### 6.6.1 ELECTRON\_CENTRAL\_18 Trigger Efficiency

We assume that the calorimeter requirements of the ELECTRON\_CENTRAL\_18 trigger are 100% efficiency. The efficiency of the tracking requirements of the ELECTRON\_CENTRAL\_18 trigger is measured using the W\_NOTRACK trigger, which is based solely on the calorimeter quantities. The trigger efficiency can then be determined from the fraction of W events that satisfies the tracking requirements.

#### ELECTRON\_CENTRAL\_18 and W\_NOTRACK Trigger Path

Table 6.18 lists the requirements of ELECTRON\_CENTRAL\_18 trigger and W\_NOTRACK trigger. Details are given below:

- Level-1: cuts on  $E_t$  of a single CEM tower and  $P_t$  of the XFT track extrapolated to it.  $E_t > 8$  GeV and  $P_t > 8.34$  GeV/ $c$  are required.
- Level-2: require a CEM cluster. The XFT track should extrapolate to the seed tower. Had/Em cut of 0.125 is applied.  $E_t > 16$  GeV and  $P_t > 8$  GeV/ $c$  are required.
- Level-3: require a central EM offline cluster with  $E_t \geq 18$  GeV and a COT track with  $P_t \geq 9$  GeV/ $c$  extrapolated to the EM cluster.

**Table 6.18:** ELECTRON\_CENTRAL\_18 trigger path, PHYSICS\_3\_00[3]

Trigger	Level	Calorimeter	Tracking
ELECTRON_CENTRAL_18	L1	$E_t\text{\_CENTRAL} \geq 8 \text{ GeV}$ $\text{HAD\_EM\_CENTRAL} \leq 0.125$	$\text{XFT\_}P_t \geq 8.34 \text{ GeV}/c$
	L2	$ \eta  \leq 1.317$ $E_t \geq 16 \text{ GeV}$ $\text{HAD\_EM} \leq 0.125$	$\text{XFT\_}P_t \geq 8 \text{ GeV}/c$
	L3	$\text{CalorRegion} = 0 \text{ (CENTRAL)}$ $\text{cen}E_t \geq 18 \text{ GeV}$  $\text{cenHadEM} \leq 0.125$  From run 159603 $\text{LShr} \leq 0.4$ $\text{cenDeltaz} \leq 8$ $\text{ZVert} = 2^2$ $\text{nTowersHadEm} = 3^2$	$\text{cenTrack}P_t \geq 9 \text{ GeV}/c$
W_NOTRACK	L1	$E_t \geq 8 \text{ GeV}$ $\cancel{E}_t \geq 15 \text{ GeV}$	none
	L2	$E_t \geq 20 \text{ GeV}$ $\cancel{E}_t \geq 15 \text{ GeV}$	none
	L3	$E_t \geq 25 \text{ GeV}$ $\cancel{E}_t \geq 25 \text{ GeV}$	none

- Lshr, cenDeltaz, ZVert = 2 and nTowersHadem = 3 requirements are added after Jan. 2005 Shutdown, after run number 159603.

We assume 100% efficiency of the calorimeter cluster requirements at each level. To measure the efficiencies of the tracking requirements of the electron trigger path, we select events from the W\_NOTRACK trigger path, that satisfies the selection

---

<sup>2</sup>If ZVert = 2, the transverse energy will be calculated using the angle of the track, instead of using the z0 of the track and the calorimeter cluster centroid. If nTowersHadEm = 3, the cenHadEm will be calculated using three hadronic towers.



criteria of  $W \rightarrow e\nu$  Events (table 6.19). The fraction of events that satisfies the tracking requirements of the electron trigger path at each level, gives the efficiency for the corresponding tracking requirement at that level. The efficiencies of the tracking requirements at each level and the total efficiency are calculated as:

- $\epsilon(L1\_P_t8) = \frac{\# \text{ of Candidates Passing } L1\_P_t8}{\text{number of W Candidates}}$
- $\epsilon(L2\_P_t8) = \frac{\# \text{ of Candidates Passing } L1\_P_t8 \text{ \& } L2\_P_t8}{\# \text{ of W Candidates Passing } L1\_P_t8}$
- $\epsilon(L3\_P_t9) = \frac{\# \text{ of Candidates Passing } L1\_P_t8 \text{ \& } L2\_P_t8 \text{ \& } L3\_P_t9}{\# \text{ of W Candidates Passing } L1\_P_t8 \text{ \& } L2\_P_t8}$
- $\epsilon(ELECTRON\_CENTRAL\_18) = \frac{\# \text{ of Candidates Passing } L1\_P_t8 \text{ \& } L2\_P_t8 \text{ \& } L3\_P_t9}{\# \text{ of W Candidates}}$

## W Event Selection

Electron candidates are required to satisfy the selection criteria listed in table 6.3 (track selection) and table 6.4 (electron ID). The W event selection criteria is listed in Table 6.19. The  $\cancel{E}_t$  is calculated using the electron beam-constrained ZVertex as the event vertex.

**Table 6.19:**  $W \rightarrow e\nu$  Event selection

Variables	Cut	variable in Duke Ntuple
Loose Central Electron	table 6.3 (track selection) table 6.4 (electron ID)	
Electron $E_t$	$\geq 25$	EMCLST_ele_std_Et
$\cancel{E}_t$	$\geq 25$	TRKDET_trkdet_cotbc_met

## Trigger Efficiency for Loose Central Electron

A Lshr and a  $\Delta z$  requirement are added to L3 trigger of the ELECTRON\_CENTRAL\_18 trigger path after run 159603 (see section 6.6.1). Table 6.20 and 6.21 show the trigger

efficiencies for data collected before and after run 159603, respectively. In both tables, no Lshr and  $\Delta z$  are applied to the loose central electron selection. As shown in these tables, the measured trigger efficiency drops from 96% to 91% for data collected after run 159603 because the trigger requirements are tighter than the loose electron ID requirements. This suggests that a Lshr and a  $\Delta z$  requirements should be added to the loose central electron (LCE) ID cuts (see table 6.4). The efficiency is measured again with these two cuts added to the LCE ID. The result is listed in table 6.22, the total trigger efficiency is now 96% for the full run range in the dataset (bhel0d).

**Table 6.20:** ELECTRON\_CENTRAL\_18 trigger Efficiency, data collected before run 159603. No Lshr and  $\Delta z$  cuts in the loose central electron selection.

	Trigger	Events	Efficiency
0:	total	26282449	
1:	GoodRun	6529513	
2:	W-NOTRACK	575218	
3:	WEvent	61089	
4:	L1CEM8 $P_t$ 8	59583	0.9753
5:	L2CEM16 $P_t$ 8	59301	0.9953
6:	L3CEM18 $P_t$ 9	58601	0.9882
7:	Total trigger efficiency	58601	0.9593

**Table 6.21:** ELECTRON\_CENTRAL\_18 trigger efficiency, data collected after run 159603. No Lshr and  $\Delta z$  cuts in the loose central electron selection.

	Trigger	Events	Efficiency
0:	total	26282449	
1:	GoodRun	13203061	
2:	W-NOTRACK	1505206	
3:	WEvent	196509	
4:	L1CEM8 $P_t$ 8	190656	0.9702
5:	L2CEM16 $P_t$ 8	189663	0.9948
6:	L3CEM18 $P_t$ 9	178516	0.9412
7:	Total trigger efficiency	178516	0.9084

Figure 6.4 shows the trigger efficiency distribution as a function of the electron

**Table 6.22:** ELECTRON\_CENTRAL\_18 trigger efficiency, with Lshr and  $\Delta z$  cuts in the loose central electron selection for one dataset (bhel0d).  $P_t > 9$  GeV/ $c$ .

	Trigger	Events	Efficiency
0:	total	26294253	
1:	GoodRun	19714810	
2:	W-NOTRACK	2078383	
3:	WEvent	239944	
4:	L1CEM8 $P_t$ 8	232986	0.971
5:	L2CEM16 $P_t$ 8	232255	0.9969
6:	L3CEM18 $P_t$ 9	230416	0.9921
7:	Total trigger efficiency	230416	0.9603

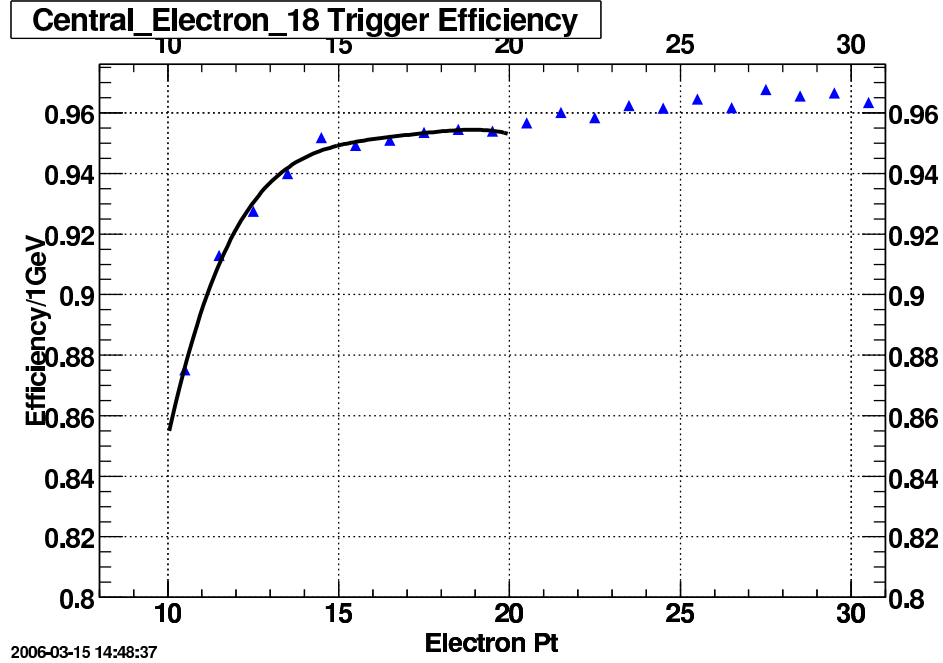


**Figure 6.4:** Electron\_Central\_18 trigger efficiency as a function of electron  $P_t$  (GeV/ $c$ ). Slow turn on at low  $P_t$ , apply trigger Efficiency weight to MC event by event for one dataset (bhel0d) .

$P_t$ . There is a slow turn-on of the efficiency at the low  $P_t$  region. To correct for the effect of this slow turn-on, a trigger efficiency weight is applied to simulation samples event by event when calculating the signal acceptance. For bhel0d dataset,

a polynomial fitting function is used, the fitting range is  $10 \leq P_t \leq 20$  GeV/ $c$ . For events with  $20 < P_t \leq 80$  GeV/ $c$ , the average efficiency 0.9603 (see Table 6.22) is used. For events with  $P_t > 80$  GeV/ $c$ , an efficiency of 1.00 is assigned to the events. There are small variations for the three datasets (0d, 0h and 0i). Details on the trigger efficiencies for the other two datasets (bhel0h and bhel0i datasets) are given in reference [60]. The trigger efficiency uncertainties and effects on cross section measurements are discussed in Chapter 9.

### Total Trigger Efficiency in Z and $Z\gamma$ Event Selection

The total ELECTRON\_CENTRAL\_18 trigger efficiency in Z or  $Z\gamma$  event selection can be determined as following:

- CC Z events: either electron can fire the trigger. The total trigger efficiency equals (1 - efficiency that neither electron fires the trigger).

$$- \epsilon^{Ele18} = 1 - (1 - \epsilon(P_{t1})) \times (1 - \epsilon(P_{t2}))$$

- CP Z events:  $\epsilon^{Ele18} = \epsilon(P_t)$

where,

- $P_t$  is the central electron track  $P_t$
- $\epsilon(P_t)$  is the ELECTRON\_CENTRAL\_18 trigger efficiency as a function of the central electron  $P_t$ .

### 6.6.2 Z\_NOTRACK Trigger Efficiency

A second trigger, the Z\_NOTRACK trigger, is also used in selecting  $Z \rightarrow ee$  event sample. This trigger requires two electromagnetic clusters with  $E_t > 18$  GeV in either

the central or forward detector regions.  $Z \rightarrow ee$  events with two central electrons (CC), or two plug electrons (PP), or one central and one plug electron (CP) can be selected through this trigger. Table 6.23 lists the requirements of the Z\_NOTRACK trigger path at each level.

**Table 6.23:** Z\_NOTRACK trigger path, from Physics Table: PHYSICS.2.05[17]

Trigger	Level	Calorimeter
Z_NOTRACK	L1_TWO_EM8	$E_t\text{-CENTRAL} \geq 8 \text{ GeV}$ $\text{HAD\_EM\_CENTRAL} \leq 0.125$ $E_t\text{-PLUG} \geq 8 \text{ GeV}$ $\text{HAD\_EM\_PLUG} \leq 0.125$
	L2_TWO_EM16	$ \eta  \leq 3.6$ $E_t \geq 16 \text{ GeV}$ $\text{HAD\_EM} \leq 0.125$ $\text{NUMBER} = 2$
	L3_TWO_ELECTRON18	$\text{CalorRegion} = 2$ (both CENTRAL and PLUG ) $\text{cen}E_t \geq 18 \text{ GeV}$ $\text{plug}E_t \geq 18 \text{ GeV}$ $\text{ZVert} = 2$ $\text{nTowersHadEm} = 3$ $\text{nEmObj} = 2$

To measure the Z\_NOTRACK trigger efficiency, we select events using the ELECTRON\_CENTRAL\_18 trigger. For each selected event, there must be two electrons, passing central or plug electron identification cuts. To reduce backgrounds, the electrons must pass the tight ID cuts (Table 6.5 and 6.8), and the di-lepton invariance mass must be within the mass window: 75-105 GeV/ $c^2$ . The  $E_t$  of the first central electron's is required to be greater than 28 GeV, where the ZNOTRACK trigger is fully efficient. The Z\_NOTRACK trigger efficiency is measured as a function of the second electron  $E_t$ . For CC events, the two electrons must have opposite-sign

charges.

The Z\_NOTRACK trigger efficiencies for central and plug electrons, are listed in table 6.24 and 6.25, respectively.

**Table 6.24:** Z\_NOTRACK Efficiency from CC Z events for one dataset (bhel0d).

Cuts	Events	Efficiency
$E_t \geq 28$ GeV	6547	
L1-CC	6547	1
L2-CC	6546	0.9998
L3-CC	6488	0.9911
Total L1-L3	6488	0.991

**Table 6.25:** Z\_NOTRACK Efficiency from CP Z events, bhel0d dataset

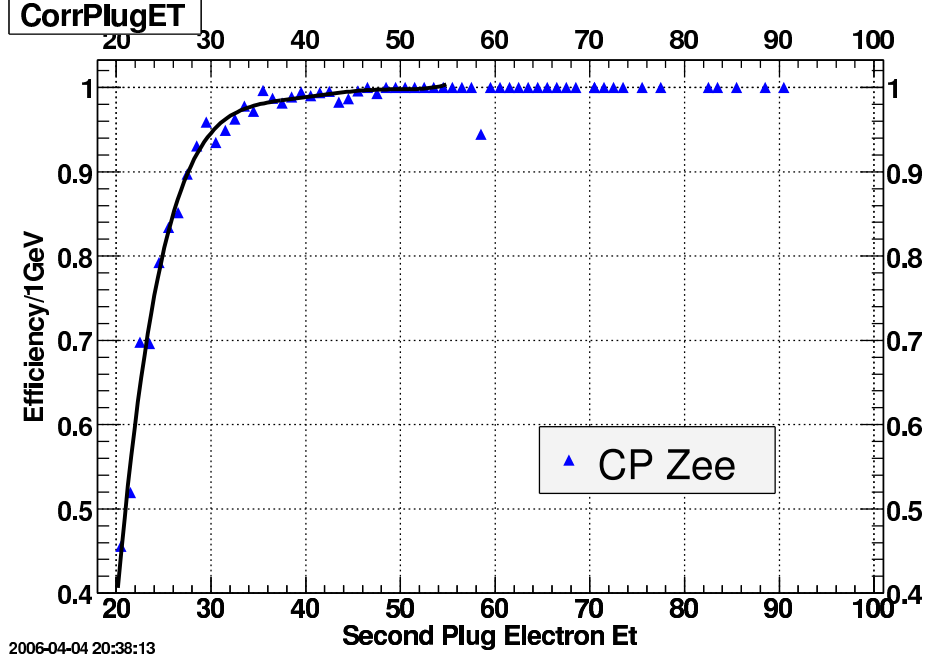
Cuts	Events	Efficiency
$E_t \geq 28$ GeV	11200	
L1-CP	11200	1
L2-CP	10779	0.9624
L3-CP	10651	0.9881
Total L1-L3	10651	0.951

Figure 6.5 shows the trigger efficiency as a function of the second electron  $E_t$  from CP Z events. A slow turn-on is observed at the low  $E_t$  region. To correct for the effect of this slow turn-on, a trigger efficiency weight is applied to detector simulation event by event when calculating the signal acceptance. More details on trigger efficiency are given in [60].

### Total Trigger Efficiency in Z and $Z\gamma$ Event Selection

The total Z\_NOTRACK trigger efficiency in Z event selection can be determined as following:

- CC Z events:  $\epsilon^{Z\_NOTRACK} = \epsilon_{Cen}(E_{t1}) \cdot \epsilon_{Cen}(E_{t2})$



**Figure 6.5:** ZNOTRACK trigger efficiency in the plug region (for one dataset bhe10d), as a function of the second Electron  $E_t$  (GeV), 28 GeV  $E_t$  cut on the first electron. Slow turn on at low  $E_t$ , a trigger efficiency weight is applied to MC event by event.

- CP Z events:  $\epsilon^{Z\_NOTRACK} = \epsilon_{Cen}(E_{t1}) \cdot \epsilon_{Plug}(E_{t2})$
- $E_{t1}$  and  $E_{t2}$  are the  $E_t$  of the two electrons.

For  $Z\gamma$  events, the ZNOTRACK trigger could be fired by either ee or  $e\gamma$ . The photon must be included in the trigger efficiency calculation. The total trigger efficiency for  $Z\gamma$  events with a central photon, is determined as following:

- Calculate efficiencies  $\epsilon_i(E_{ti})$ ,  $i = e_1, e_2, \gamma$   
where  $E_{ti}$  is the  $E_t$  of the electrons or photon.
- $\epsilon^{Z\_NOTRACK} = 1 - (1 - \epsilon_1 \cdot \epsilon_2) \times (1 - \epsilon_1 \cdot \epsilon_3) \times (1 - \epsilon_2 \cdot \epsilon_3)$

### 6.6.3 Total Trigger Efficiency

The total trigger efficiency in the inclusive Z or  $Z\gamma$  event selection is then given as:

$$\epsilon_{trig} = 1 - (1 - \epsilon^{Ele18}) \times (1 - \epsilon^{Z\_NOTRACK})$$

For CC Z events, the total trigger efficiency is 100% (see table 6.12). For CP Z events, the total trigger efficiency is 99.6% (see table 6.13).

The trigger efficiency uncertainties and effects on cross section measurements are discussed in Chapter 9.

## 6.7 Background Estimation

Hadronic jets can sometimes be selected as electrons in the detector. We refer to this as QCD background to the Z signal events. In this section, side-band subtraction method for QCD background prediction is discussed. The shape of the background is determined using electron+jets data.

### 6.7.1 QCD background shape

The main background source in the Z selection is QCD events, where a jet is misidentified as an electron. To get a shape of the QCD background, we use the high  $P_t$  electron datasets, requiring that there is one and only one electron in the events. The central electron must satisfy the loose electron selection criteria listed in table 6.4. The plug electron must satisfy the loose plug electron selection criteria listed in table 6.7. To identify a jet, we use cuts in the loose electron selection, but veto the HadEm and Isolation cuts (see table 6.26 and 6.27). The mass spectra of  $M_{ej}$  provide a measure of the shape of the QCD background events in our selected Z boson sample.



**Table 6.26:** Central loose electron ID Cuts and central jet selection cuts

Variables	Central Loose Electron ID	Central Jet Selection
All COT Tracks:		
# Axial SLs	$\geq 3$ with $\geq 5$ hits per SL	$\geq 3$ with $\geq 5$ hits per SL
# Stereo SLs	$\geq 2$ with $\geq 5$ hits per SL	$\geq 2$ with $\geq 5$ hits per SL
BC $ z_0 $	$\leq 60$ .	$\leq 60$ .
Region	CEM ( $ \eta  < 1.1$ )	CEM ( $ \eta  < 1.1$ )
$E_t$	$\geq 20$ GeV	$\geq 20$ GeV
$TrackP_t$	$\geq 10$ GeV/ $c$	$\geq 10$ GeV
Conversion	not equal 1	not equal 1
CES fiducial	= 1	= 1
$E_{had}/E_{em}$	$\leq 0.055$ + $0.00045 \cdot E$	$> 0.055$ + $0.00045 \cdot E$
Iso(R=0.4)/ $E_t$	$\leq 0.3$ ( loose isolation cut )	$> 0.3$
Lshr	$\leq 0.4$	—
$ \Delta z $	$\leq 8$ cm	—

**Table 6.27:** Plug loose electron ID cuts and plug jet selection cuts

Variables	Plug Electron ID Cuts	Plug Jet Selection Cuts
Region	PEM ( $1.1 \leq  \eta  < 3.6$ )	PEM ( $1.1 \leq  \eta  < 3.6$ )
PES 2D Eta	$1.2 \leq  \eta  \leq 2.8$	$1.2 \leq  \eta  \leq 2.8$
$CorrE_t$	$\geq 20$ GeV	$\geq 20$ GeV
$E_{had}/E_{em}$	$\leq 0.05$	$> 0.05$
PEM 3x3 chi2	$\leq 25$ .	—
Iso(R=0.4)/ $E_t$	$\leq 0.3$ ( loose isolation cut )	$> 0.3$

### 6.7.2 QCD Background Estimation – Side-band Subtraction Method

The QCD background is determined using the side-band subtraction method. The mass spectra of the Z boson simulation sample ( $M_{MC}$ ) provide a measure of the shape of the Z signal events. The mass spectra in the selected Z boson data sample ( $M_{data}$ ) is fitted to the signal prediction ( $M_{MC}$ ) and background prediction  $M_{ej}$ . The  $Z \rightarrow ee$  signal is subtracted from the data. The fraction of background in the

data is determined by comparing the residual side-band (outside Z mass window) distribution to the background distribution. The background is determined with the following procedure:

- Step 1: normalize the simulation spectrum from  $Z \rightarrow ee$  (blue curve in Figure 6.6 (a)) to the data spectrum (red curve in Figure 6.6 (a) ) in a tight Z mass window  $86-98 \text{ GeV}/c^2$ .
- Step 2: get the difference:  $\text{Diff}(M_{ee}) = \text{Data (red)} - \text{MC (blue)}$  over the full  $ee$  mass range. The difference is shown as the pink curve in Figure 6.6 (b).
- Step 3: normalize the background shape spectrum  $M_{ej}$  (green curve in Figure 6.6 (b) ) in the upper sideband ( $116 \leq M_{ee} \leq 220 \text{ GeV}/c^2$ ) to the spectrum  $\text{Diff}(M_{ee})$  from step 2.
- Step 4: get background prediction using integral of bin  $66-116 \text{ GeV}/c^2$  in the background shape spectrum  $M_{ej}$  (green region in Figure 6.6 (c) ).
- Step 5: subtract the background in the normalization described in step 1:
  - normalize simulation spectrum to (Data- QCD Bkg) in the mass window  $86-98 \text{ GeV}/c^2$
  - repeat step 2-4. Figures 6.6 (d) - (f) show the distributions in the second iteration.

Figure 6.6 shows the background prediction in the CP channel for one dataset (bhel0h). The QCD background in the CC Z sample is  $0.89\% \pm 0.34\%$  (see Table 6.28). The QCD background in the CP Z sample is  $7.7\% \pm 1.0\%$  (see Table 6.29).

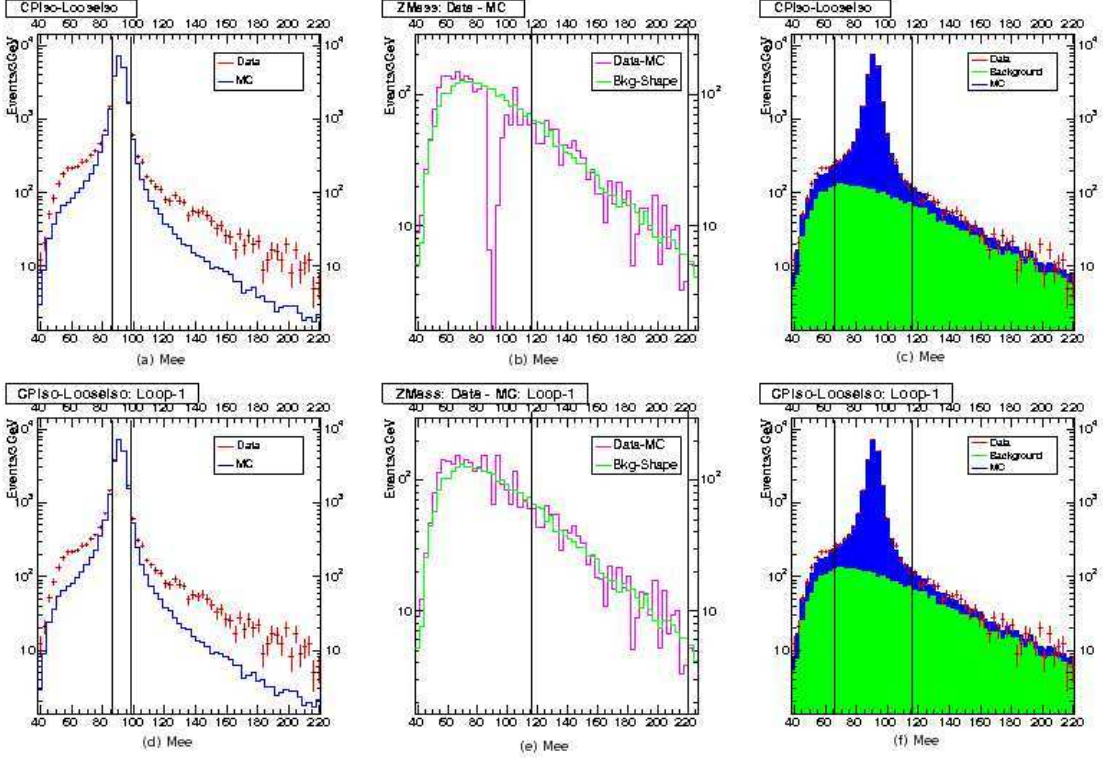


**Figure 6.6:** Di-lepton mass distribution ( $\text{GeV}/c^2$ ) in Zee CP background subtraction for one dataset (bhel0h).

### 6.7.3 Systematic Uncertainties

#### Systematic Uncertainties – CC Channel

For the central region, by assuming that the signs of the electrons for QCD background are uncorrelated, the number of QCD background events can be determined using same-sign method. The QCD background equals the number of same-sign events observed in data, corrected for trident events:

$$N^{bkg} = N_{Data}^{SS} - N_{Data}^{OS} \times N_{MC}^{SS}/N_{MC}^{OS}$$

Table 6.28 compares the background prediction using the side-band subtraction method and the same-sign method. The result from the side-band subtraction method is taken as the prediction of the QCD background. The systematic error

on the QCD background prediction is taken to be the difference between the two methods.

**Table 6.28:** CC Z QCD background prediction for one dataset (bhel0d).

Dataset	Z region	Signal	Side-band method	Same-sign method	Difference
bhel0d	CC	9403	0.89%	0.55%	0.34%

### Systematic Uncertainties – CP Channel

In the side-band subtraction method, either the upper side-band ( $116 \leq M_{ee} \leq 220$ ) or the lower side-band ( $40 \leq M_{ee} \leq 66$ ) can be used for normalization. The result from the upper side-band subtraction is taken as the prediction of the QCD background. The difference in the results is assigned as the systematic uncertainty for the QCD background prediction in the CP channel (see table 6.29).

**Table 6.29:** CP Z QCD background prediction for one dataset (bhel0d).

Dataset	Z region	Signal	upper side-band normalization	lower side-band normalization	Difference
bhel0d	CP	20236	7.7%	8.7%	1.0 %

## 6.8 Chapter Summary

The  $Z \rightarrow ee$  signal acceptance is measured from the generation of events with a detector simulation. The Z acceptance with two central electrons is  $0.1118 \pm 0.0002$  and the Z acceptance with one central and one forward electron is  $0.2288 \pm 0.0003$ . The electron identification efficiencies and scale factors are summarized in Table 6.5.1 and 6.5.2. The predictions from the simulation agree very well to the data. The scale

factors are close to 1.00. The trigger efficiencies are measured from data. These triggers are highly efficient, with efficiencies close to 100%. The QCD background to the selected Z boson sample is determined from data. The QCD background is  $0.89\% \pm 0.34\%$  in the CC Z sample and  $7.7\% \pm 1.0\%$  in the CP Z sample. The measured acceptance, efficiency scale factors, trigger efficiencies and QCD background will be used in calculating the inclusive Z cross section in the next chapter.

# Chapter 7

## Inclusive Z Cross Section Measurement

The cross section for Z boson production from  $p\bar{p}$  collision at  $\sqrt{s} = 1.96$  TeV is calculated for the loose Z selection described in Chapter 6. This is compared to both the SM prediction and previous inclusive Z cross section measurements. This serves as a cross check of the Z selection for our  $p\bar{p} \rightarrow Z \gamma + X$  measurement.

### 7.1 Previous measurements

The previous published result [62] for the inclusive Z cross section in the invariant di-lepton mass range between 66 GeV/ $c^2$  and 116 GeV/ $c^2$  is

$$\sigma(p\bar{p} \rightarrow Z/\gamma^* + X) \cdot Br(Z/\gamma^* \rightarrow ll) = \\ 254.9 \pm 3.3(stat.) \pm 4.6(syst.) \pm 15.2(lum.) \text{ pb}$$

This was measured with 72  $pb^{-1}$  of  $p\bar{p}$  integrated luminosity.

Since then, a new measurement [63] using 337  $pb^{-1}$  of data for the  $Z \rightarrow \mu\mu$  channel has been made. The cross section is measured to be:

$$\sigma(p\bar{p} \rightarrow Z/\gamma^* + X) \cdot Br(Z/\gamma^* \rightarrow \mu\mu) = \\ 261.2 \pm 2.7(stat.) \pm_{-6.9}^{+5.8}(syst.) \pm 15.1(lum.) \text{ pb}$$

The SM prediction for the inclusive Z boson cross section in the invariant di-lepton mass range between 66 GeV/ $c^2$  and 116 GeV/ $c^2$  is  $251.3 \pm 5.0$  pb [62].

## 7.2 The Inclusive Z Cross Section in the Channel with Two Central Electrons

In this section, we describe the measurement of the Z cross section where both electrons are in the central region (CC).

The Z selection in the CC Channel are listed below:

- For each event, there must be at least two high  $E_t$  ( $E_t > 20$  GeV) electrons:
  - Both electrons must pass the central loose electron ID cuts (table 6.4)
- Both electrons must satisfy the loose isolation cut(  $\text{IsoR} < 0.3$  )
- At least one electron must satisfy the tight isolation cut(  $\text{IsoR} < 0.1$  )
- The invariant mass of the di-lepton must be in the range of  $66 < M_{ee} < 116$  GeV/ $c^2$
- The two electrons must have opposite-signed charges.

The inclusive  $Z \rightarrow ee$  cross section is calculated as following:

$$\sigma(p\bar{p} \rightarrow Z/\gamma^* + X) \cdot Br(Z/\gamma^* \rightarrow ll) = \frac{N_Z^{\text{obs}} - N_Z^{\text{bck}}}{A_Z \cdot \epsilon_Z \cdot \int \mathcal{L} dt} \quad (7.1)$$

where:

- $\int \mathcal{L} dt$  is the integrated luminosity
- $A_Z$  is the Z acceptance
- $\epsilon_Z$  is the total Z selection efficiency
- $N_Z^{\text{obs}}$  is the number of opposite-signed CC  $Z \rightarrow ee$  events

- $N_Z^{\text{bck}}$  is the number of the QCD background events where a jet fakes an electron

The following efficiencies are included in the total Z selection efficiency calculation:

1. Vertex efficiency  $\epsilon_{\text{vtx}}$  [64], which measures the fraction of events that occur within 60 cm of the center of the detector. The vertex requirement ( $Z_{\text{vtx}} \leq 60$  cm) limits the selected events to a fraction of the full luminous region. The efficiencies are:
  - $0.951 \pm 0.003$  ( bhel0d dataset)
  - $0.960 \pm 0.003$  ( bhel0h dataset)
  - $0.966 \pm 0.003$  ( bhel0i dataset)
2. The tracking efficiency  $\epsilon_{\text{trk}}$ , which is the efficiency for reconstructing the high  $P_T$  track in the COT tracking chamber. The tracking efficiency  $\epsilon_{\text{trk}}(\text{Data})$  is  $0.996 \pm 0.004$  [62]. The efficiency measured from the detector simulation sample  $\epsilon_{\text{trk}}(\text{MC})$  is  $0.997 \pm 0.002$ . Since this in-efficiency is already accounted for in the Z acceptance calculation using the simulated sample (see Section 6.4), to avoid doubling counting, the ratio of the tracking efficiency measured in data to that measured in the simulation sample is applied as a final net tracking efficiency.  $\epsilon_{\text{trk}} = 1.000 \pm 0.004$  is used in the total Z efficiency calculation.
3. The reconstructing efficiency  $\epsilon_{\text{rec}}$ , which is the efficiency of reconstructing real electrons by offline algorithms. This efficiency is measured to be  $0.998 \pm 0.004$  [62].
4. The electron identification efficiency:
  - The loose electron identification efficiency  $\epsilon_{\text{lid}} = 0.961$  (bhel0d dataset, Table 6.14).



- The loose isolation efficiency  $\epsilon_{\text{Liso}} = 0.997$  (bhel0d dataset, Table 6.14 )
- The tight isolation efficiency  $\epsilon_{\text{Tiso}} = 0.980$  (bhel0d dataset, Table 6.14 )
- The tight electron identification efficiency  $\epsilon_{\text{tid}} = 0.874$  (bhel0d dataset, Table 6.14 )
- The total efficiency for identifying tight electrons can then be calculated as:

$$\epsilon = \epsilon_{\text{lid}} \cdot \epsilon_{\text{Liso}} \cdot \epsilon_{\text{Tiso}} \cdot \epsilon_{\text{tid}} = 0.961 \cdot 0.997 \cdot 0.980 \cdot 0.874 = 0.821$$

5. The total efficiency for Z selection:

- The total efficiency for selecting LCE-LCE Z events is:

$$\epsilon_{\text{tot}}^{\text{LL}} = \epsilon_{\text{vtx}} \times \epsilon_{\text{trk}}^2 \times \epsilon_{\text{rec}}^2 \times \epsilon_{\text{lid}}^2 = 0.876$$

- total event selection efficiency for TCE-TCE Z events:

$$\epsilon_{\text{tot}}^{\text{TT}} = \epsilon_{\text{tot}}^{\text{LL}} \times \epsilon_{\text{Liso}}^2 \times \epsilon_{\text{Tiso}}^2 \times \epsilon_{\text{tid}}^2 = 0.639$$

The efficiency to select a Z boson drops from 0.876 to 0.639 when the tight electron identification requirements are applied. The Z selection efficiencies for requiring two isolated loose central electrons ( $\text{IsoR} < 0.1$  for at least one electron) are listed in Table 7.1. This Z boson sample will be used for the study of  $p\bar{p} \rightarrow ee + \gamma + X$  production.

### 7.2.1 Measure Inclusive Z Cross Section in CP Channel

In this section, we describe the measurement of the Z cross section where one electron is in the central region and the other one is in the forward (plug) detector region (CP). The Z selection in the CP channel are listed below:

- For each event, there must be at least two high  $E_t$  ( $E_t > 20$  GeV) electrons:

- One is a central loose electron (table 6.4)
- The other is a loose plug electron (LPE) (table 6.7)
- Both electrons must satisfy the loose isolation cut(  $\text{IsoR} < 0.3$  )
- At least one electron must satisfy the tight isolation cut(  $\text{IsoR} < 0.1$  )
- The invariant di-lepton mass must be in the range of  $66 < M_{ee} < 116 \text{ GeV}/c^2$

### 7.3 Measurement of the Inclusive Z Cross Section – $1 \text{ fb}^{-1}$

In this section, we summarize the inclusive Z cross section measured with  $1 \text{ fb}^{-1}$  of data. The results (see Table 7.1) are in good agreement with the SM prediction and previous measurements at CDF. This inclusive Z sample will be used for the  $Z\gamma$  study.

**Table 7.1:** Cross-section calculation for  $\sigma(p\bar{p} \rightarrow Z/\gamma^* + X) \cdot Br(Z/\gamma^* \rightarrow ee)$ .

dataset	Z	Signal	Bkg	Bkg/Signal	$\epsilon_Z$	$A_Z$	$\sigma(p\bar{p} \rightarrow Z/\gamma^* + X) \cdot Br(Z/\gamma^* \rightarrow ll) \text{ (pb)}$
bhel0d	CC	9403	83.9	0.009	0.870	0.112	$257.0 \pm 2.7 \text{ (stat)} \pm 14.6 \text{ (lum)}$
$373 \text{ pb}^{-1}$	CP	20236	1563.4	0.077	0.836	0.229	$262.0 \pm 2.0 \text{ (stat)} \pm 14.9 \text{ (lum)}$
bhel0h	CC	10696	135.6	0.013	0.870	0.112	$253.5 \pm 2.5 \text{ (stat)} \pm 14.4 \text{ (lum)}$
$428 \text{ pb}^{-1}$	CP	23187	1735.0	0.075	0.833	0.231	$261.1 \pm 1.9 \text{ (stat)} \pm 14.9 \text{ (lum)}$
bhel0i	CC	6840	111.2	0.016	0.868	0.112	$253.9 \pm 3.1 \text{ (stat)} \pm 14.5 \text{ (lum)}$
$274 \text{ pb}^{-1}$	CP	14467	1084.2	0.075	0.827	0.230	$257.7 \pm 2.3 \text{ (stat)} \pm 14.7 \text{ (lum)}$

# Chapter 8

## Photon Selection, Identification and Background Study

In this chapter, photon selection and identification are discussed. The precision of the measurement of  $Z\gamma$  production is limited by the understanding of the selected photon candidates. The photon detection efficiency must be measured from data using either "pure" electron or photon sources. A new method using a photon source from the final state radiation in  $Z \rightarrow l^+l^- + \gamma$  events is described in Section 8.2. The background due to jets passing the photon selection criteria must be evaluated. To estimate the background, the jet  $\rightarrow \gamma$  fake rate is measured from a sample of jets passing the photon selection criteria. This fake rate is applied to jets in Z+jet events to determine the background to Z+ $\gamma$  events.

### 8.1 Photon Selection Criteria

Photons are selected with  $E_t \geq 7$  GeV and  $|\eta| < 1.1$  using the central detector. The photon is required to separate from any primary electron or muon by  $\Delta R(l-\gamma) > 0.4$ . The central photon selection cuts are summarized in Table 8.1.

The variables used in selecting central photon are the following [65]:

- Event vertex in z along colliding beam:

For our  $Z\gamma$  analysis, there will be two electrons in the events from the Z boson decay. The vertex information from the central electrons is used to determine the vertex z for the central photons. If there is an "event vertex" within 5cm of the central electrons in the events, that vertex is used as the photon vertex.

**Table 8.1:** Central photon identification cuts.

Variables	Cut
EtCorr	$\geq 7$
$ cesx $	$< 21$ cm
$ cesz $	$9 <  cesZ  < 230$ cm
Had/Em	$< 0.125 \parallel < 0.055 + 0.00045 * \text{E} \text{Corr}$
IsoEtCorr	EtCorr $< 20$ : $< 0.1 * \text{EtCorr}$
	EtCorr $\geq 20$ : $< 2.0 + 0.02 * (\text{EtCorr} - 20.0)$
Chi2(Strips + Wires)/2	$< 20$
N track(N3D)	$\leq 1$
Track $P_t$	$< 1.0 + 0.005 * \text{EtCorr}$
Cone 0.4 Track Iso	$< 2.0 + 0.005 * \text{EtCorr}$
2nd CES cluster	(both strip and wire E individually)
$E * \sin(\theta)$	EtCorr $< 18$ : $< 0.14 * \text{EtCorr}$
	EtCorr $\geq 18$ : $< 2.4 + 0.01 * \text{EtCorr}$

Otherwise the vertex z of the highest  $E_t$  central electron is used.

- ces x and ces z:

The photon position inside an electromagnetic calorimeter tower. This is measured by the CES detector.

- raw energy:

The total amount of energy for a photon is obtained directly from the EM cluster (using 2-tower sum).

- Corrected E:

The energy is then corrected for the CES x and z positions (face corrections).

- $E_t$  :

The transverse component of E (=  $E \sin\theta$ ), from the event vertex z.

- Had/Em:

Ratio of the hadronic/electromagnetic energy.

- IsoEtCorr:

The calorimeter isolation energy is the  $E_t$  sum in a cone of  $\Delta R = \sqrt{\Delta\phi^2 + \Delta\eta^2} < 0.4$  around the photon's seed position of the energy cluster. The isolation energy is corrected to the event vertex  $z$ . It is then corrected for leakage energy and number of additional  $p\bar{p}$  interaction vertices.

- Chi2:

A  $\chi^2$  fit of the CES shower profile (strip or wire) to the profile from test beam electrons.

- Track  $P_t$ :

The highest transverse momentum track, pointing to the photon energy cluster.

- N track (N3D):

The number of tracks, pointing to the photon energy cluster. A maximum of one track is allowed, and the track  $P_t$  must be less than  $1.0 + 0.005 * E_t$  (GeV).

- Cone 0.4 track Iso

Track isolation energy is sum of the transverse momentum over all tracks within 5 cm of the photon vertex in a 0.4 cone.

- Second CES cluster  $E \cdot \sin(\theta)$ :

Energy of any second strip (wire) cluster.

See Table 8.1 for the selection cuts on these variables.

## 8.2 Photon identification efficiency

In this section, the efficiency measurement is described for photons with  $E_t \geq 7$  GeV and  $|\eta| < 1.1$ . The photons are selected using the CEM detector with the

cuts described in Section 8.1. The photon identification efficiency is based upon the selection of a very pure photon source from final state radiation in  $Z \rightarrow l^+l^- + \gamma$  events (see Figure 8.1) . The electron data has a total luminosity of  $\sim 1 \text{ fb}^{-1}$ . The muon data has a total luminosity of  $\sim 1.6 \text{ fb}^{-1}$ . The photon efficiency for detector simulation samples is measured from the  $Z(\text{ee})\gamma$  simulation sample.

**Table 8.2:** Central photon denominator cuts for identification efficiency measurement.

Variables	Cut
EtCorr	$\geq 7$
$ cesX $	$< 21 \text{ cm}$
$ cesZ $	$9 <  cesZ  < 230 \text{ cm}$
Had/Em	$\leq 0.125$
IsoEtCorr	$\leq 5$
Track $P_t$	$< \text{EtCorr} / 2$
Cone 0.4 Track Iso	$\leq 5$

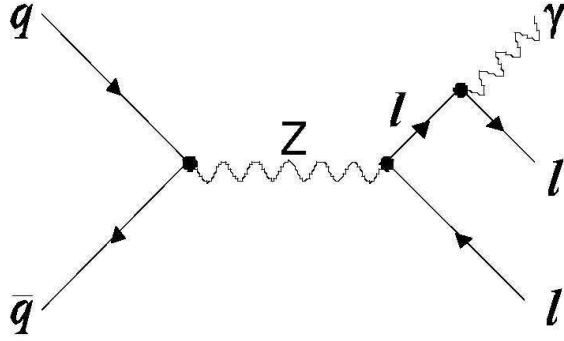


**Figure 8.1:**  $Z\gamma$  Final State Radiation (FSR).

The identification efficiency of photons is determined using the CDF detector simulation with corrections (scale factors) measured from data. Photons can fail the selection criteria given in Table 8.1 due to conversions before reaching the calorimeter, calorimeter electromagnetic shower fluctuations, or general underlying event activity

that causes isolation failures. The latter depends on the environment in which the photon is produced. For the study of  $p\bar{p} \rightarrow l^+l^- + \gamma + X$  events it is desirable to measure the photon detection using a "pure" sample of photons isolated in these events. Z boson production with hard final state radiation off the decay leptons (see Figure 8.1) are identified, and the  $l^+l^- + \gamma$  system is required to have an invariant mass near the Z boson mass. In this section this method for measuring photon detection efficiencies is described, and the determination of the required detector simulation scale factors is presented. Events are required to have two and only two leptons with  $P_t > 20 \text{ GeV}/c$ . The leptons must pass the standard tight-lepton selection cuts. Muon pairs and CEM-CEM electron pairs are required to have opposite signs, and CEM-PEM and PEM-PEM electron pairs are also included. The PEM electrons are required to pass the silicon detector tracking requirements. A subset of these events is selected by requiring one and only one photon object in the central region. The specific criteria for the photon objects are given in Table 8.2. These are chosen with very loose cuts on the variables used to identify photons, but require the shower position to be in a central fiducial region.

Having identified events with two tight leptons and a "loose" photon object, cleanup cuts are applied to suppress background events. The events are required to have:

- $\cancel{E}_t < 10 \text{ GeV}$  and  $P_t(Z\gamma) < 10 \text{ GeV}/c$  to suppress WW/WZ/ZZ events
- $M_{ll} < 80 \text{ GeV}/c^2$  to suppress Z + jet events

The invariant mass distribution of the three-body system is plotted in Figure 8.2 for the  $ee\gamma$  data, showing the progressive effect of each of the cleanup cuts on the selection of the  $Z \rightarrow l^+l^- + \gamma$  events. Finally, the photons used for the detection efficiency measurement are selected by requiring:

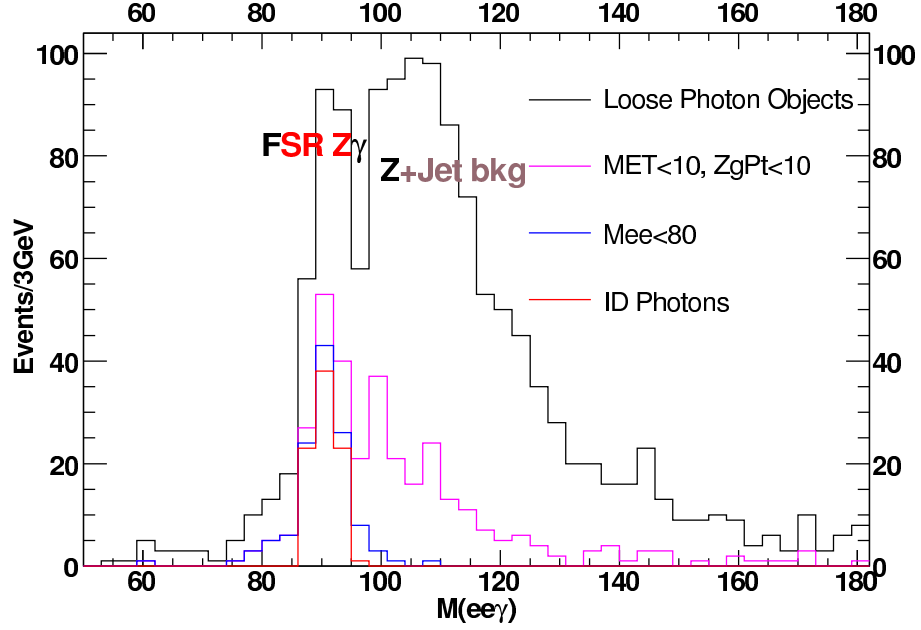


**Figure 8.2:** The invariant mass ( $\text{GeV}/c^2$ ) distribution of the  $ee\gamma$  three-body system with  $1 \text{ fb}^{-1}$  electron data.

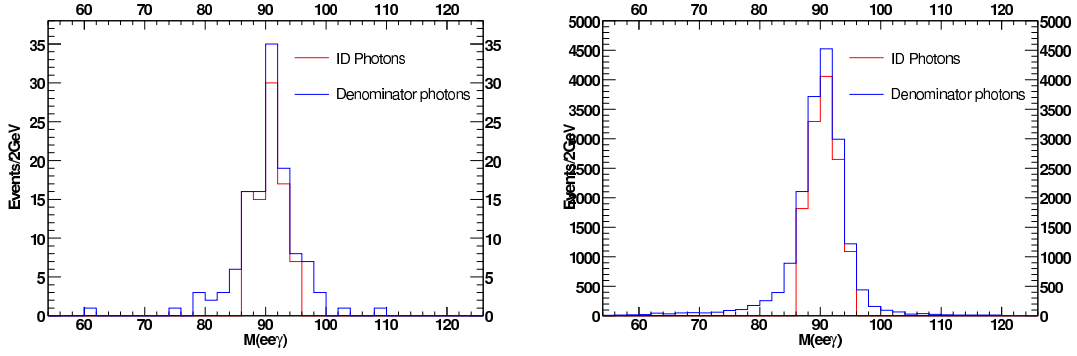


**Figure 8.3:** Three body mass ( $\text{GeV}/c^2$ ) distribution of the  $Z\gamma$  events used in photon detection efficiency measurement.  $Z\gamma$  1fb electron data (left),  $Z(ee)\gamma$  detector simulation sample *reuk33* (right).

- $86 < M_{u\gamma} < 96 \text{ GeV}/c^2$

Figure 8.3 shows the distribution of the three-body mass of the  $Z\gamma$  events used for the photon detection efficiency measurement. Table 8.3 summarizes the number of



$l\bar{l}\gamma$  events surviving all selection cuts, with the number of photons candidates in the central detector.

The above photon sample is then subjected to the photon selection cuts shown in Table 8.1. The resulting photon detection efficiencies from the data are compared to those predicted from the detector simulation where identical selection cuts are used. The data are divided into subsets depending on the lepton pair selection to test the consistency of the measurements. The photon detection efficiency is defined as following:

- Photon detection efficiency:
  - fraction of photon candidates passing the photon selection cuts
  - Denominator: photon candidates passing the detector acceptance cuts
  - Numerator: photon candidates passing the photon selection cuts
- Photon N-1 detection efficiency:
  - Efficiency for one selection cut
  - Denominator: photon candidates passing all but the Nth selection cut
  - Numerator: photon candidates passing the photon selection cuts

The efficiencies measured from the  $Z\gamma$  simulation sample are listed in table 8.4.

Figs. 8.4 - 8.5 show the distributions of photon detection efficiency as a function of photon  $E_t$  and detector  $\eta$ . The efficiencies are slightly dependent on the photon  $E_t$  for central photons. Figure 8.6 shows the distribution of photon detection efficiencies a function of photon  $E_t$ , where the efficiencies for data and simulation are plotted in black and blue respectively. The photon detection efficiencies for data and detector

**Table 8.3:** Muon+Electron Channel Central Photon total detection efficiency and N-1 detection efficiency from data

	Events	Efficiency
ID Photon	196	$0.86 + 0.02 - 0.02$
2ndCesE	200	$0.98 + 0.01 - 0.01$
Chi2	197	$0.99 + 0.00 - 0.01$
IsoEt	204	$0.96 + 0.01 - 0.02$
N3D	198	$0.99 + 0.01 - 0.01$
TrackIso	201	$0.98 + 0.01 - 0.01$
Track $P_t$	199	$0.98 + 0.01 - 0.01$
Candidates	229	

**Table 8.4:** Electron Channel Central Photon total detection efficiency and N-1 detection efficiency for detector simulation samples.

	Events	Efficiency
ID Photon	16780	$0.88 + 0.00 - 0.00$
2ndCesE	16996	$0.99 + 0.00 - 0.00$
Chi2	16841	$1.00 + 0.00 - 0.00$
IsoEt	17811	$0.94 + 0.00 - 0.00$
N3D	16871	$0.99 + 0.00 - 0.00$
TrackIso	17005	$0.99 + 0.00 - 0.00$
Track $P_t$	16917	$0.99 + 0.00 - 0.00$
Candidates	18984	

simulation agree well. The efficiency scale factor (SF), defined

$$SF = \frac{\epsilon(\text{Data})}{\epsilon(\text{Simulation})}$$

is plotted in red in Figure 8.6. The scale factors in each  $E_t$  bin are listed in table 8.5.

**Table 8.5:** Central photon efficiency scale factor.

$E_t^\gamma$ (GeV)	Scale Factor
7 - 12	$0.95 \pm 0.04$
12 - 20	$1.00 \pm 0.04$
20 - 40	$0.95 \pm 0.06$

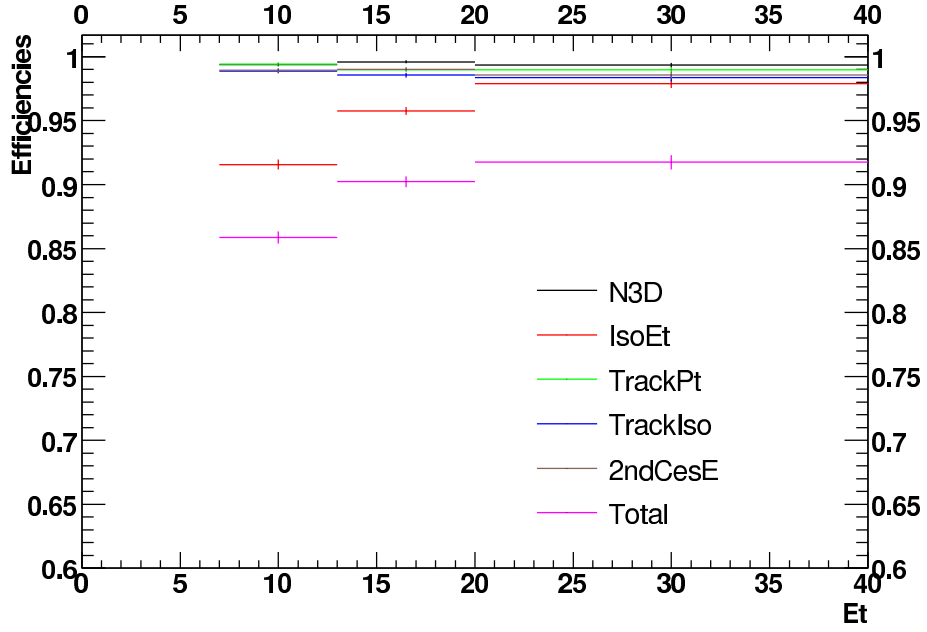


**Figure 8.4:** Central Photon N-1 detection efficiency as a function of photon  $E_t$  (GeV) measured from  $Z\gamma$  simulation sample.

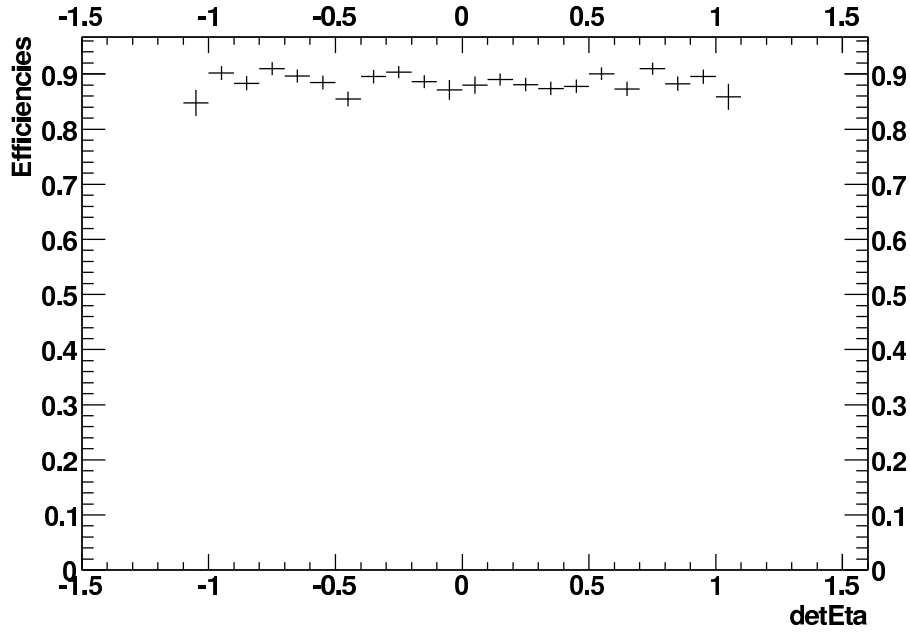


**Figure 8.5:** Central Photon detection efficiency as a function of  $\eta$  measured from  $Z\gamma$  simulation sample.

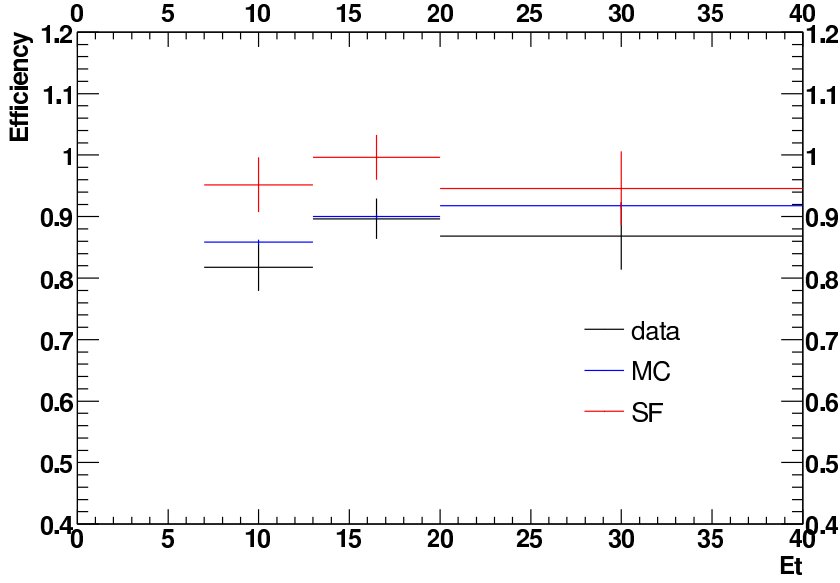


**Figure 8.6:** Central Photon detection efficiencies as a function of photon  $E_t$  (GeV), data vs simulation.

For reference, the result [66] measured from electron samples are listed in Table 8.6. This is measured in a different kinematic range ( $E_t > 15\text{GeV}$ ), and a small difference in the efficiencies is observed. The scale factors measured from both methods are consistent.

**Table 8.6:** Old method. Photon detection efficiencies and scale factors using Zee samples [66].  $E_t^\gamma > 15\text{ GeV}$ ,  $|\eta| < 1.1$ .

Eff(%)	Data	Simulation	Scale Factor
Central	$90.85 \pm 0.73$	$92.61 \pm 0.16$	$0.98 \pm 0.01$ (stat) $\pm 0.01$ (syst)

In summary, a new method has been developed to measure the photon detection efficiency directly from a pure FSR  $Z\gamma$  photon sample. The result is given in Table 8.7. The simulation agrees quite well with the data. This method is currently limited by statistics. The statistical uncertainty on the scale factor is 2% and the systematic uncertainty is 1%.

**Table 8.7:** Photon detection efficiencies and scale factors using FSR photon samples.  $E_t^\gamma > 7$  GeV,  $|\eta| < 1.1$ .

Eff	Data	Simulation	Scale Factor
Central	$0.86 \pm 0.02$	$0.88 \pm 0.00$	$0.98 \pm 0.02$ (stat) $\pm 0.01$ (syst)

## 8.3 Photon Background

The precision of an analysis that requires the identification of an isolated high energy photon is inherently limited by the effectiveness of photon selection algorithms. These consist of the identification efficiency of real photons and corrections for the background rate at which high energy jets are misidentified as photons. In this section, we describe a measurement of the probability at which jets are mis-identified as photons by passing standard photon selection cuts. This jet-to-photon fake rate is measured for jets with  $E_t > 7$  GeV and  $|\eta| < 1.1$ . The general approach is to measure the photon fake rate from high statistics jet data and then after necessary corrections, apply it to the jets in  $Z + \text{jet}$  events to obtain a data-driven prediction of the fake photon backgrounds in the  $Z\gamma$  production.

### 8.3.1 Overview of the fake rate measurement

The jet-to-photon fake rate for isolated jets is measured from a sample of jet-triggered events. This fake rate is referred to as  $P_{raw}^{QCD}(E_t)$ . Several corrections are made to  $P_{raw}^{QCD}(E_t)$  to obtain the photon fake rate  $P_{true}^Z(E_t)$  that is applied to the jets associated with  $Z$  events. The corrections are summarized here.

1. The  $P_{raw}^{QCD}(E_t)$  must be corrected for the fraction of the accepted "jets" that are true hadronic quark/gluon showers and not a contamination from real photons.

This correction factor is referred to as  $F_{QCD}$  and is a function of jet  $E_t$ :

$$F_{QCD} = \frac{N(jets \rightarrow \gamma)}{N(jets \rightarrow \gamma) + N(\gamma)}$$

where the number of events refer to those passing the photon selection cuts.

This correction factor is then applied to obtain:

$$P_{true}^{QCD}(E_t) = F_{QCD}(E_t) \times P_{raw}^{QCD}(E_t)$$

2. The  $P_{true}^{QCD}(E_t)$  fake rate applies to the mixture of selected QCD jets. There are two corrections to be made in transforming this to the fake rate  $P_{true}^Z(E_t)$  to be applied to the jets in Z events to obtain the desired photon backgrounds in the  $Z\gamma$  events.

- (a) The fake rate of quark jets is approximately ten times that of gluon jets based upon Monte Carlo studies [67]. The measured fake rate is sensitive to the quark/gluon mixture on the selected jet samples. Under the assumption that the quark jets dominate the fake rate the correction factor is simplified to

$$F_{q/g}(E_t) = R_{ZJet}(q/g)/R_{QCD}(q/g),$$

where  $R(q/g)$  is the fraction of quark jets in the samples.  $R_{ZJet}$  is the fraction of quark jets in the Z + jet sample, and  $R_{QCD}$  in the QCD jet sample. Therefore:

$$P_{true}^{ZJet}(E_t) = F_{q/g}(E_t) \times P_{true}^{QCD}(E_t)$$

(b) The fake rate  $P_{true}^{Z,Jet}(E_t)$  is applied to each jet in the Z + jet data sample.

This predicts the number of fake photons versus the  $E_t$  of the jets that cause these faked photon. This is not the same as the  $E_t^\gamma$  of the photon that would have been measured if it was detected as a photon and would be mostly electromagnetic energy. To predict the photon background in the  $Z\gamma$  events versus  $E_t^\gamma$ , a transfer function is applied to convert jet  $E_t$  to  $E_t^\gamma$ .

For further discussions of the method see references [67,68].

### 8.3.2 Raw Fake Rate Measurement

#### Selection of QCD jets

The measurement uses jets from the Jet20, Jet50, Jet70, and Jet100 triggered data sets, filtered by the electron/muon no-silicon good run list version 13. These data sets, which range from runs 138425 to 212133, contain  $\approx 1 \text{ fb}^{-1}$  of integrated luminosity, or roughly five times the data collected in the previous fake rate analysis [68]. The raw jet  $E_t$  is calculated using 0.4 cone size clustering.

The QCD events are filtered by requiring that the  $\Delta R$  separation between the two highest energy jets is at least 0.7. In this subset of events only those jets that are separated from all other jets by  $\Delta R > 0.7$  are considered. The jets are further subdivided into three groups from highest to lowest jet  $E_t$ : 1st jet, 2nd jet, and 3 or more jets (referred to as jet category "345th"). The highest energy jet category is rejected to avoid trigger bias. Either the 2nd or 345th category could be used for the raw fake photon measurement. However, the 345th jet energy spectrum most closely matches the jet energy spectra in the  $Z\gamma$  events, and therefore we choose this jet mixture for the  $P_{raw}^{QCD}(E_t)$  measurement. Jets with  $E_t > 7 \text{ GeV}$  and  $|\eta| < 1.1$  are

considered for the central photon raw fake rate measurement.

### Measurement of $P_{raw}^{QCD}(E_t)$

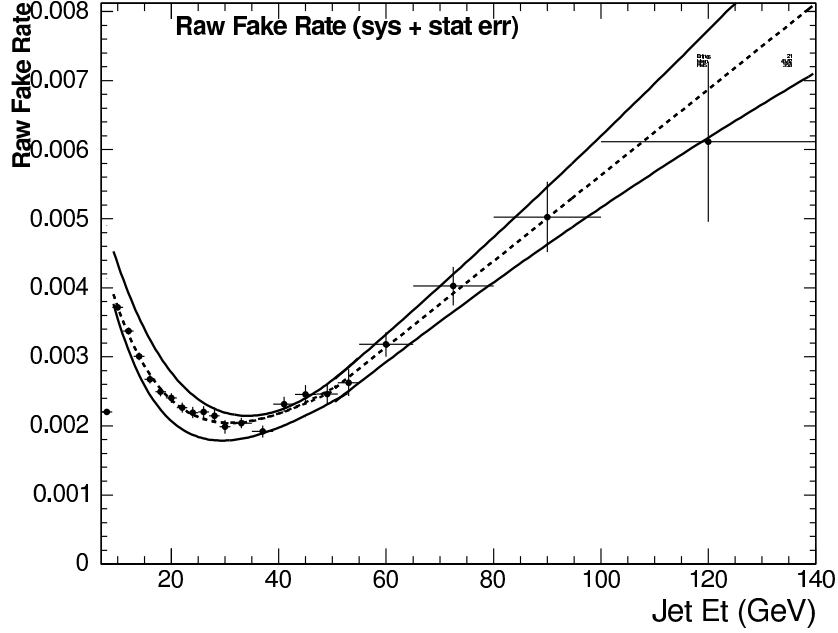


**Figure 8.7:** Raw fake rate with error bands and central fit.

Using the above QCD jet sample, for each event, the separation between the closest matching electromagnetic (EM) object to the selected jet is calculated. If the separation has  $\Delta R < 0.1$ , the EM object is accepted as a candidate for faking a photon. The photon selection cuts (listed in Table 8.1) are applied to the matched EM objects to determine the number of candidates accepted as central photons.  $P_{raw}^{QCD}$  is measured as a function of the jet  $E_t$ . Figure 8.7 shows this raw fake rate as a function jet  $E_t$  using the combined 345th jet sample. An  $E_t$ -dependent shape is observed as the photon selection cuts depend on  $E_t$ . The value of  $P_{raw}^{QCD}$  is  $\approx 0.4\%$  at the lowest jet  $E_t$  and decrease to  $\approx 0.2\%$  at 35 GeV. At this point the ability of the CES becomes to resolve single and multiple photons is lost and the fake rate slowly



risks to  $\approx 0.6\%$  at  $\approx 100$  GeV.

As a measure of the systematic errors separate analyses are made using the different jet data sets (JEt20, JEt50, JEt70, and JEt100). The difference in the fake rate measured from these datasets is assigned as a systematic error. Combining the statistical and systematic errors in quadrature leads to the upper and lower error bands (solid curves) shown in Figure 8.7 with the dashed curve the fit to the fake rate from the combined 345 jet sample. The parameterization of these curves is given in reference [69].

### 8.3.3 Real Photon Correction

The decay of  $\pi^0$  and  $\eta^0$  mesons, originating from final state quark or gluon showers result in photons not associated with the process of interest. In this analysis, we call the photons from these decays "fake" photons, whereas prompt photons created via direct production or radiated off a final state quark or lepton make up the "real" photon signal.

The jet samples used to measure the raw fake rate contain "real" photons from direct production or bremsstrahlung radiation. The real photons have a high probability to pass the photon selection and thus increase the measured fake rate. A correction factor,  $F_{QCD}$ , is applied to the raw fake rate to correct for prompt photon contamination. Correcting the raw fake for prompt photon contamination must be accomplished by statistical methods, because particle by particle identification is not possible. In this section, we describe three methods that are used to measure the  $F_{QCD}$ .

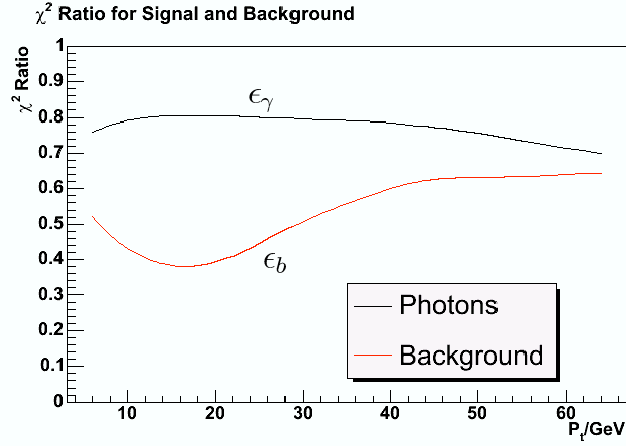


**Figure 8.8:** The signal ( $\epsilon_{\gamma}$ ) and background ( $\epsilon_b$ ) templates for the CES method [54].

### CES Weighting Method

This method uses the Central Electromagnetic Shower (CES) detector, a strip and wire chamber, that is embedded in the Central Electromagnetic Calorimeter (CEM) wedges. The CES detector provides high-precision position measurement of the electromagnetic shower inside the calorimeter. A single photon shower is typically narrower than showers from  $\pi \rightarrow \gamma\gamma$  decays. For a given sample, the fraction of pion events can be determined from the fraction of "wide" showers in the sample.

The transverse shower profile measured from electron test beam data is used to distinguish electrons/photons from pions. A CES  $\chi^2$  variable is defined to describe how well the measured shower profile matches to an electron shower profile. A  $\chi^2$  ratio variable is calculated as:

$$\epsilon = \frac{N^{\chi^2 < 4}}{N^{\chi^2 < 20}}$$

where  $N^{\chi^2 < 4}$  is the number of events with  $\chi^2 < 4$  and  $N^{\chi^2 < 20}$  is the number of events

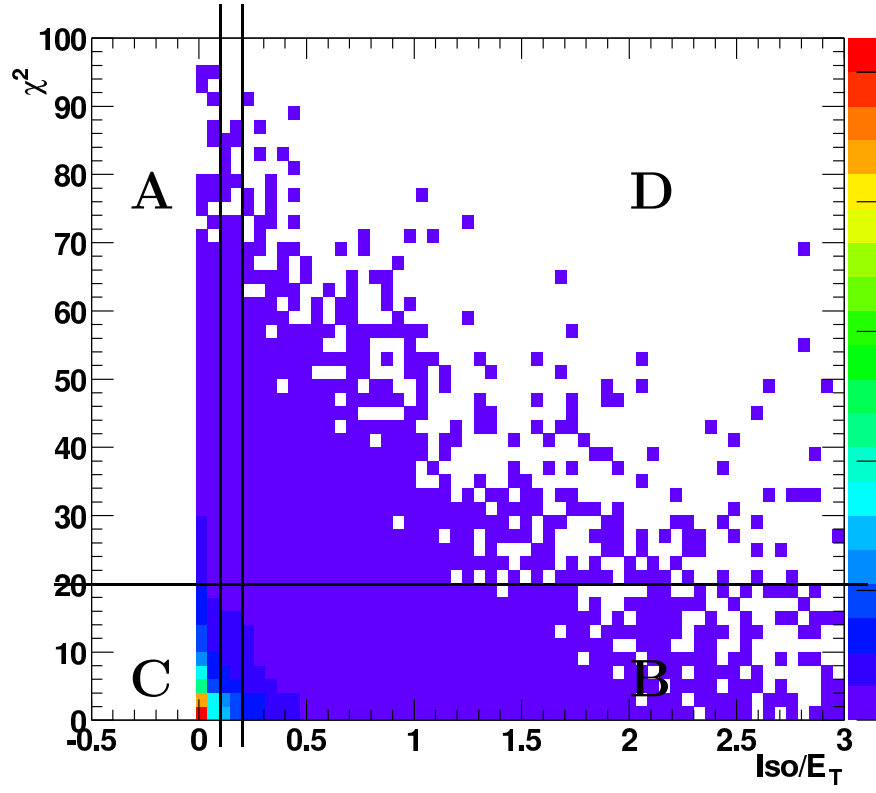


**Figure 8.9:**  $\text{Iso}/E_t$  vs  $\chi^2$ . Illustrated are the four regions A, B, C and D used for determining the QCD background fraction  $F_{QCD}$  [54].

with  $\chi^2 < 20$ . Background events, in general, have larger  $\chi^2$  values and the ratio  $\epsilon_b$  is smaller than  $\epsilon_\gamma$  of photon events (see Figure 8.8). This ratio in the data is equal to:

$$\epsilon_{data} = \frac{\epsilon_\gamma N_\gamma + \epsilon_b N_b}{N_{data}}$$

where,

$$N_{data} = N_\gamma + N_b$$

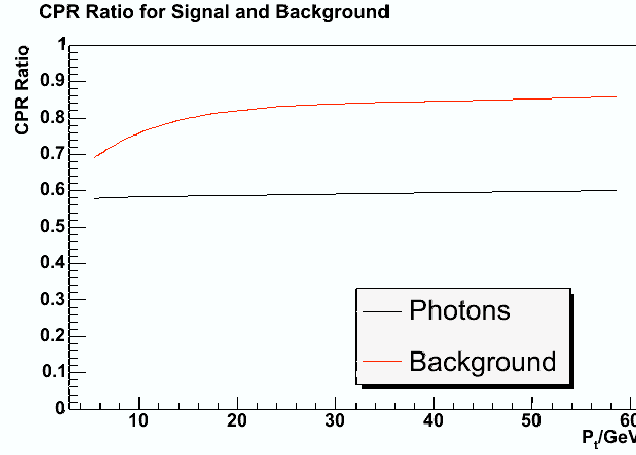


**Figure 8.10:** The conversion probabilities for signal prompt photons ( $P_{conv}^\gamma$ ) and background mesons ( $P_{conv}^{QCD}$ ) as a function of  $E_t$  [54].

and the background fraction can be calculated as:

$$F_{QCD} = \frac{N_b}{N_{data}} = \frac{\epsilon_{data} - \epsilon_\gamma}{\epsilon_b - \epsilon_\gamma}$$

### Isolation vs CES $\chi^2$ Method

In a 2-dimensional distribution of the calorimeter isolation variable and the CES  $\chi^2$  variable, signal events congregate in the low isolation and low  $\chi^2$  region, while background events have large isolation energy due to hadronic activity. The 2-dimensional plane of isolation vs.  $\chi^2$  can be divided into four regions (see Figure 8.9), where region C is the signal region and region D is entirely background. Assuming no correlation between the isolation energy and the CES  $\chi^2$  for background events, the background in region C can be determined as:

$$\frac{N_C^{BG}}{N_A} = \frac{N_B}{N_D}$$

and

$$F_{QCD} = \frac{N_C^{BG}}{N_C} = \frac{N_B N_A}{N_D N_C}$$

The CES  $\chi^2$  and the isolation vs.  $\chi^2$  method break down for events with  $E_t > 40$  GeV, where the two photons from pion decays are too close together and the two-photon showers become too similar to single prompt photon showers. In the high  $E_t$  region, the CPR method is used to evaluate  $F_{QCD}$ .

### CPR Weighting Method

This method uses the Central Pre-Radiator (CPR) detector that is mounted on the inner surface of the CEM wedges. The solenoid and the Central Outer Tracking (COT) detector are served as radiators for the CPR detector. The conversion rate of prompt photons and pions in the solenoid is measured by the charge deposited in the CPR detector. Let the conversion rate of a single photon be  $P_\gamma$ , the conversion probability of a pion ( $\pi^0 \rightarrow \gamma\gamma$ ), where both photons can convert, is equal to  $1 - (1 - P_\gamma)^2$ . If the single photon conversion rate is 60%, the conversion rate of a pion is then 84%. Background events, in general, have higher conversion rate than that of photon events (see Figure 8.10). By measuring the fraction of events that deposit significant charge in the CPR detector, the background fraction can be extracted.

### $F_{QCD}$ Measurement

Figure 8.11 shows the  $F_{QCD}$  measurement from the three methods described above. The difference between the three methods are assigned as systematic, the upper and lower error bands are showed in the solid lines. The central fit curve (dashed line) in the figure is the average of the two extremes. More details on  $F_{QCD}$  measurement

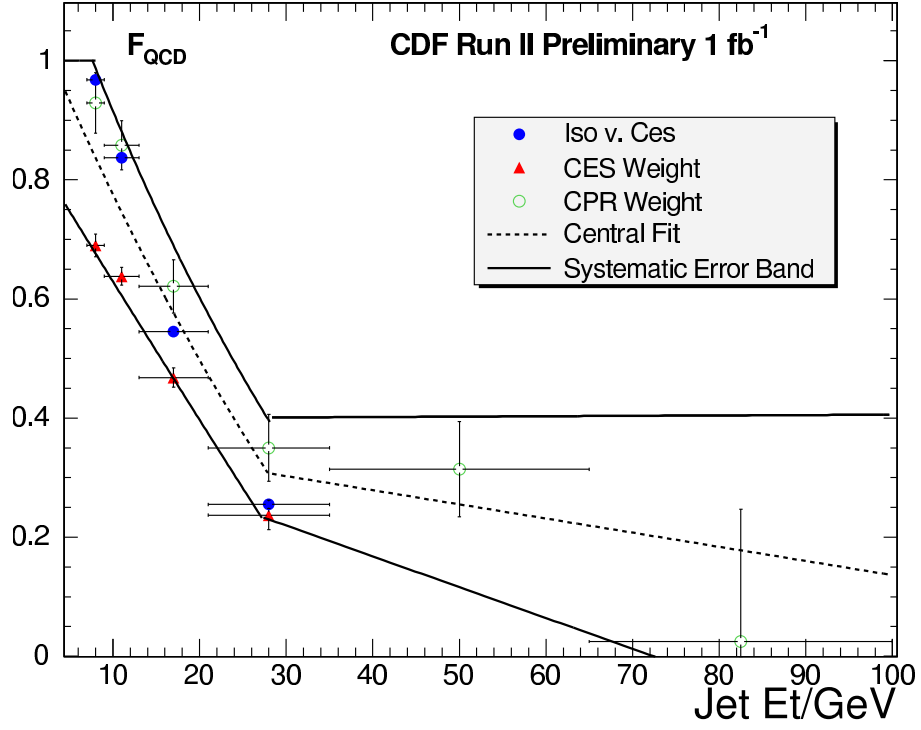


**Figure 8.11:**  $F_{QCD}$  using three methods: Iso vs CES  $\chi^2$ , CES weighting and CPR weighting. Solid lines are the upper and lower error bands and the dashed line is central fit curve.

are given in reference [69].

### 8.3.4 True Fake Rate

The raw fake rate is corrected by the “real” photon contamination to obtain the true fake rate for the QCD jet samples.

$$P_{true}^{QCD}(E_t) = F_{QCD}(E_t) \times P_{raw}^{QCD}(E_t)$$

Figure 8.12 shows  $P_{true}^{QCD}$  as a function of jet  $E_t$  with error bands (solid lines). The error includes the uncertainties in the raw fake rate measurement, in the “real” photon correction  $F_{QCD}$  and the statistical uncertainty. The dominant error is from the

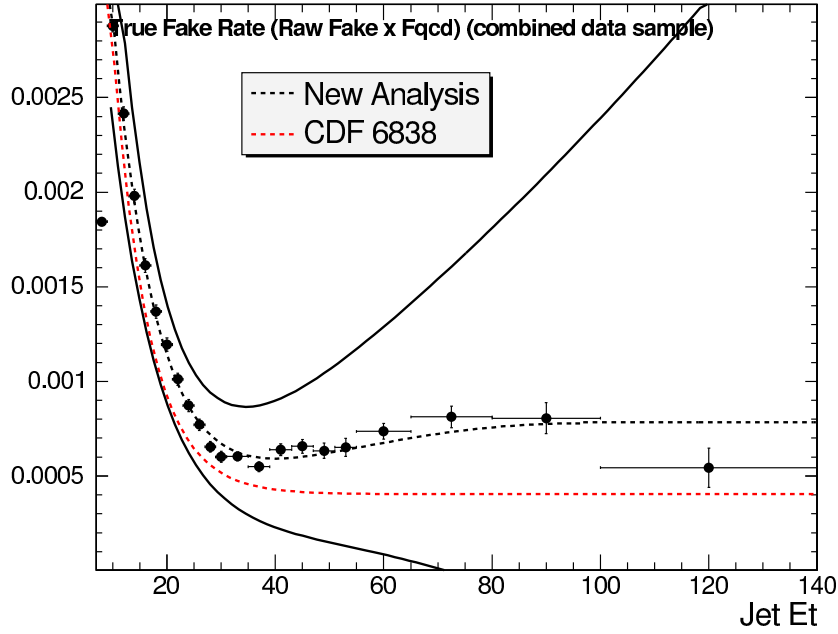


**Figure 8.12:** True fake rate  $P_{true}^{QCD}(E_t)$  as a function of jet  $E_t$  (GeV) for QCD jet sample with error bands(solid), central fit(dashed), and old measurement with 200  $\text{pb}^{-1}$  of data [68].

$F_{QCD}$  measurement, especially in the high  $E_t$  region, where the  $F_{QCD}$  measurement is statistical limited.

### 8.3.5 Quark/gluon Ratio Correction

Jets originating from quarks have a different fake rate than those from gluons. The fake rate depends on the quark-gluon composition in the sample studied. The quark-gluon composition in the QCD jet sample is different to the Z + jet sample. In order to apply the fake rate measured from QCD jet sample to the Z + jet sample, a correction factor  $F_{q/g}$ , defined as the ratio of the quark content in the Z + jet sample to that in the QCD jet sample, is applied to the  $P_{true}^{QCD}$  to obtain the true fake rate for the Z + jet sample. Figure 8.13 shows the corrected true fake rate, this is then

applied to jets in the  $Z + \text{jets}$  event to estimate the jet background contribution in the  $Z\gamma$  production. The probability to mis-identify a jet with  $E_t = 10$  GeV is about 0.3%. As the jet  $E_t$  increases, the mis-identified rate drops to about 0.1% for jets with  $E_t > 35$  GeV.

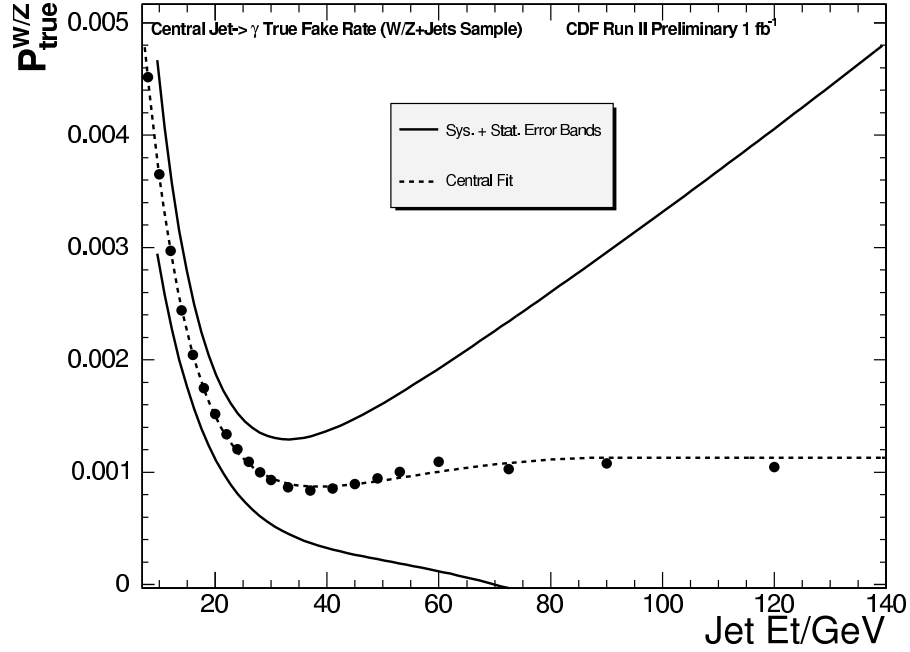


Figure 8.13: True fake rate for the  $Z + \text{jet}$  sample.

## 8.4 Chapter Summary

A new method to measure the photon detection efficiency from a pure photon sample is presented. The efficiency measured from the data agrees well with the prediction from the detector simulation. The probability for a jet to be misidentified as a photon is measured with jet triggered data. In the next chapter, this fake rate is applied to jets in  $Z + \text{jet}$  events to predict the QCD background to  $Z + \gamma$  events.



# Chapter 9

## Cross Section Measurement of $p\bar{p} \rightarrow e^+e^-\gamma + X$ Production

In this chapter, a measurement of the  $p\bar{p} \rightarrow e^+e^-\gamma + X$  production cross section is presented. Both  $Z\gamma$  production and single  $Z$  production with  $Z \rightarrow ee\gamma$  contribute to the  $e^+e^-\gamma$  final states. In this chapter, "Z $\gamma$  measurement" refers to measuring  $Z\gamma$  plus  $Z \rightarrow ee\gamma$ .

### 9.1 $Z\gamma$ Event Selection

The selection of the  $Z\gamma$  candidate events is described in this section. The  $Z\gamma$  samples are collected from  $p\bar{p}$  collisions with triggers requiring at least one high  $P_t$  electron candidate.

#### 9.1.1 Z Selection

The loose electron selection criteria described in Section 6.3 is used in selecting  $Z\gamma$  candidate events. Table 9.1 and 9.2 list the electron selection in the central and forward region, respectively. For more details on the electron selection and identification efficiency measurement, see Chapter 6.

To select  $Z$  candidate events, there must be at least two high  $E_t$  electrons with  $E_t > 20$  GeV for each event, one of the electron must be in the central detector region. If both electrons are in the central region (CC  $Z$  event), they must have opposite-sign charges. Both electrons are required to pass the loose isolation cut ( $\text{IsoR} < 0.3$ ), and at least one of the electron must pass the tight isolation cut ( $\text{IsoR} < 0.1$ ).

**Table 9.1:** Loose central electron identification cuts. The text in red shows the cut that is different to the standard central electron identification cut.

Variables	Cut
Region	CEM ( $ \eta  < 1.1$ )
COT track	satisfy loose track quality requirements
$E_t$	$\geq 20$
$TrackP_t$	$\geq 10$
$E_{had}/E_{em}$	$\leq 0.055 + 0.00045 \cdot EMCLST\_ele\_std.E$
Conversion	$\neq 1$
CES fiducial	$= 1$
$Iso(R=0.4)/E_t$	$\leq 0.3$ (Loose Isolation cut )
Lshr	$\leq 0.4$
$ \Delta Z $	$\leq 8$

**Table 9.2:** Loose plug electron identification cuts, the text in red shows the cut that is different to the standard plug electron identification cut.

Variables	Cut
Region	PEM ( $1.1 \leq  \eta  < 3.6$ )
PES 2D Eta	$1.2 \leq  \eta  \leq 2.8$
$CorrE_t$	$\geq 20$
$E_{had}/E_{em}$	$\leq 0.05$
PEM 3x3 chi2	$\leq 25.$
$Iso(R=0.4)/E_t$	$\leq 0.3$ ( loose isolation cut )

The electron and Z selection criteria is summarized below:

- For each event, there must be at least two high  $E_t$  electrons:
  - CC Z: two opposite-sign central loose electrons(table 9.1)
  - CP Z: one central loose electron (table 9.1) and one plug loose electron (table 9.2)
- Both electrons pass the loose isolation cut ( $IsoR < 0.3$ )
- At least one electron passes the tight isolation cut ( $IsoR < 0.1$ )

### 9.1.2 $Z\gamma$ Event Selection in the Central Photon Channel

With the Z sample selected, we further require there must be at least one photon in the central detector region with  $E_t > 7$  GeV. The photon is required to pass the central photon selection cuts (table 8.1) and it must be well separated from the two electrons in the events with a separation  $\Delta R(e, \gamma) > 0.7$ . The di-lepton invariant mass must be greater than  $40 \text{ GeV}/c^2$ . This  $Z\gamma$  sample can be further divided into two subsets depending on the three-body invariant mass  $M_{ee\gamma}$ . The low mass region ( $M_{ee\gamma} \leq 100 \text{ GeV}/c^2$ ) is dominated by final state radiation (FSR) contribution, and the high mass region ( $M_{ee\gamma} > 100 \text{ GeV}/c^2$ ) is an initial state radiation (ISR) dominant region. The ISR region is most sensitive to anomalous couplings (see Chapter 10). The cross sections for the full  $Z\gamma$  sample, as well as the ISR and FSR subsets are measured. The ISR sample is used to probe anomalous couplings of the photon to the Z boson.

## 9.2 Total $Z\gamma$ Event Selection Efficiency

The  $Z\gamma$  event selection efficiency in data is given by:

$$\epsilon_{Z\gamma}^{\text{Data}} = \epsilon_{Zid}^{\text{Data}} \times \epsilon_{\gamma id}^{\text{Data}}$$

where:

- $\epsilon_{Zid}$  is the Z selection efficiency.
- $\epsilon_{\gamma id}$  is the photon selection efficiency.

The  $Z\gamma$  total selection efficiency predicted by the detector simulation is given by:

$$\epsilon_{\text{tot}}^{\text{MC}} = \epsilon_{\text{Zid}}^{\text{MC}} \times \epsilon_{\gamma\text{id}}^{\text{MC}} \quad (9.1)$$

The efficiency scale factor used to correct imperfection in the detector simulation is given by:

$$SF = \epsilon_{\text{tot}}^{\text{Data}} / \epsilon_{\text{tot}}^{\text{MC}} = SF_{\text{Zid}} \times SF_{\gamma\text{id}} \quad (9.2)$$

The predictions from the simulation agree very well to the data. The scale factors are close to 1.00.

There are two more efficiencies that must be included for the data sample, but not for the simulation sample. The first one is the trigger efficiency, described in Section 6.6. The second one is the efficiency of the  $|Z_0| \leq 60\text{cm}$  vertex requirement. The measured luminosity is multiplied by this efficiency to obtain the corrected integrated luminosity for the measurement of  $Z\gamma$  production.

### 9.3 Background Estimation

The  $Z\gamma$  production channel is very clean, with only two significant background sources. The main background is from  $Z + \text{jet}$  events, where a jet is misidentified as a photon. A second background source is from  $\gamma + \text{fake } Z$  events, where a jet is misidentified as an electron. The  $Z + \text{jet}$  background is  $51.6 \pm 14.1$  events, and the  $\gamma + \text{fake } Z$  background  $13.9 \pm 7.1$  events in the final  $Z\gamma$  sample of 390 events.

### 9.3.1 Z + jet QCD Background

The estimation of the Z + jet QCD background is based on a data-driven measurement of the photon fake rate as described in Section 8.3.

#### Photon Fake Rate

The probability to mis-identify a jet as a photon is shown in Figure 8.13 in Section 8.3. The probability to mis-identify a jet with  $E_t = 10$  GeV is about 0.3%. As the jet  $E_t$  increases, the mis-identified rate drops to about 0.1% for jets with  $E_t > 35$  GeV.

#### Estimate Z + Jet QCD Background

We apply the jet  $\rightarrow$  photon fake rate to the Z + jet events in the electron-triggered data sample, where the jet has  $|\eta| < 1.1$  and  $\Delta R_{ej} > 0.7$ . The number of background events from jets faking photons is given as [54]:

$$\begin{aligned} N_{BG}(E_t^\gamma) &= \int_0^{N_{jet}(Z)} P_{jet \rightarrow \gamma}^Z(E_t^{jet}) \times dN_Z/dE_t^{jet} \times z(E_t^{jet}, E_t^\gamma) dE_t^{jet} \\ &= \int_0^{N_{jet}(Z)} P_{jet \rightarrow \gamma}^j(E_t^{jet}) \times \frac{dN_Z/dE_t^{jet}}{dN_{jet}/dE_t^{jet}} dN_{jet}/dE_t^{jet} \times z(E_t^{jet}, E_t^\gamma) dE_t^{jet} \end{aligned} \quad (9.3)$$

where,

- $P_{jet \rightarrow \gamma}^j(E_t^{jet})$ : probability of a jet faking a photon for jets in the jet sample
- $P_{jet \rightarrow \gamma}^Z(E_t^{jet})$ : probability of a jet faking a photon for jets in the Z sample
- $z(E_t^{jet}, E_t^\gamma)$ : probability of a jet of  $E_t^{jet}$  to be measured as  $E_t^\gamma$ .
- $dN_Z/dE_t^{jet}$ :  $E_t^{jet}$  distribution in Z sample
- $dN_{jet}/dE_t^{jet}$ :  $E_t^{jet}$  distribution in a jet triggered sample

- $\frac{dN_Z/dE_t^{jet}}{dN_{jet}/dE_t^{jet}}$  term cancels if the  $E_t$  distributions in the two samples are the same.
- "345th" jet sample is the sample of jets of the 3rd, 4th, 5th etc. highest  $E_t$  jets. The 345th jet in the jet samples has a very similar  $E_t^{jet}$  distribution as that in the Z sample. This sample is used to measure  $P_{jet \rightarrow \gamma}(E_t^{jet})$ .

The Z + jet QCD background is determined to be  $51.6 \pm 14.1$  events in a sample of 390  $Z\gamma$  candidate events (see Section 9.6.2).

### 9.3.2 $\gamma$ + Jet QCD Background

The second background source for  $Z\gamma$  production is the  $\gamma$  + fake Z events, where a jet is faking an electron. To estimate this background, we assume that the fake Z QCD background in the  $Z\gamma$  sample scales as in the inclusive Z sample. The fake Z QCD background in the  $Z\gamma$  sample can then be estimated as:

- $N_{Z\gamma}^{Bkg} = N_Z^{Bkg} * R$

where,

- $N_Z^{Bkg}$  is the estimated QCD background in the inclusive Z sample (see Section 6.7.2)
- R is the fraction of the fake Z QCD background events that has an additional photon.  $R = \frac{N_{FakeZ\gamma}}{N_{FakeZ}}$  is obtained from the fake Z background template (electron-antielelectron sample).

The number of  $\gamma$  + fake Z background is estimated to be  $13.9 \pm 7.1$  events, with  $1.8 \pm 1.3$  events in the CC Z region and  $12.1 \pm 5.8$  events in the CP Z region.

## 9.4 $Z\gamma$ Cross Section Calculation

The  $Z\gamma$  cross section is calculated as:

$$\sigma_{ee\gamma} = \frac{N^{\text{obs}} - N^{\text{bkg}}}{A \cdot \epsilon \cdot \int \mathcal{L} dt}$$

where,

- $N^{\text{obs}}$  is the number of observed  $Z\gamma$  events
- $N^{\text{bkg}}$  is the number of background events
- $A$  is the acceptance of the  $Z\gamma$  production, defined as the fraction of  $Z\gamma$  events that satisfy the fiducial and geometric requirements of our detector. This is measured from the SM generation of  $p\bar{p} \rightarrow e^+e^- + \gamma + X$  production followed by the CDF detector simulation.
- $\epsilon$  is the total  $Z\gamma$  event selection efficiency for events within the  $Z\gamma$  geometric acceptance,  $\epsilon = \epsilon_{Z\gamma} \cdot \epsilon_{\text{trig}} \cdot \epsilon_{|z|<60}$ .  $\epsilon_{Z\gamma}$  is the total  $Z\gamma$  event selection efficiency discussed in Section 9.2;  $\epsilon_{\text{trig}}$  is the trigger efficiency, very close to 100% (see Section 6.6.3);  $\epsilon_{|z|<60}$  is the efficiency of the  $|z_0| < 60$  cm cut (see Section 7.2).
- $\int \mathcal{L} dt$  is the integrated luminosity

The  $Z\gamma$  cross section will be quoted in a specific kinematic range, with  $E_t^\gamma > 7$  GeV,  $\Delta R_{e\gamma}(e, \gamma) > 0.7$ ,  $M_{ee} > 40$  GeV/ $c^2$ . The (acceptance  $\times$  efficiency) term is first measured using the detector simulation:

$$A \cdot \epsilon_{MC} = \frac{N_{ee\gamma}}{N_{\text{gen}}} \quad (9.4)$$

where,

- $N_{ee\gamma}$  is the number of events passing the  $ee\gamma$  event selection criteria using the detector simulation.
- $N_{gen}$  is the number of events generated in the above kinematic range.

This (acceptance  $\times$  efficiency) term  $A \cdot \epsilon_{MC}$  is then corrected to account for simulation imperfection:

$$A \cdot \epsilon_{data} = A \cdot \epsilon_{MC} \cdot SF \quad (9.5)$$

where, SF is the total efficiency scale factor (see Equation 9.2).

The number of expected  $ee\gamma$  events predicted by the SM is:

$$N_{SM}^{exp} = \sigma_{NLO} \cdot A \cdot \epsilon_{data} \cdot \int \mathcal{L} dt \quad (9.6)$$

where  $\sigma_{NLO}$  is the NLO cross-section in the above kinematic range.

The cross-section for the above kinematic range is then simplified to:

$$\sigma_{ee\gamma} = \frac{N^{obs} - N^{bkg}}{A \cdot \epsilon \cdot \int \mathcal{L} dt} = \frac{N^{obs} - N^{bkg}}{N_{SM}^{exp}} \cdot \sigma_{NLO} \quad (9.7)$$

Table 9.6.2 lists the input numbers to the cross section calculation using the above equation.

## 9.5 Systematic Uncertainties

In this section, the systematic errors and their effects on  $Z\gamma$  cross section are discussed.

To evaluate the uncertainties on  $Z\gamma$  cross section measurement, the cross section



calculation is written in the following form

$$\sigma = \frac{N_d - \Sigma N_{bi}}{D}$$

where:

- $N_d$  = number of selected  $Z\gamma$  candidate events (data)
- $N_{bi}$  = estimated background of type i
- $D = A \cdot \epsilon_{MC} \cdot SF \cdot \epsilon_{trig} \cdot \epsilon_{z < 60} \cdot \int \mathcal{L} dt$

The uncertainty on the cross section is obtained by propagating uncertainties in  $N_d$ ,  $N_{bi}$  and D:

$$\begin{aligned} \left(\frac{\Delta\sigma}{\sigma}\right)^2 &= \left(\frac{N_d}{N_d - \Sigma N_{bi}}\right)^2 \cdot \left(\frac{\Delta N_d}{N_d}\right)^2 \\ &\quad + \left(\frac{N_{bi}}{N_d - \Sigma N_{bi}}\right)^2 \cdot \left(\frac{\Delta N_{bi}}{N_{bi}}\right)^2 \\ &\quad + \left(\frac{\Delta D}{D}\right)^2 \end{aligned}$$

The error on the denominator can be furthered expanded as:

$$\begin{aligned} \left(\frac{\Delta D}{D}\right)^2 &= \left(\frac{\Delta(L\epsilon_{z < 60})}{L\epsilon_{z < 60}}\right)^2 + \left(\frac{\Delta A_{ee\gamma}}{A_{ee\gamma}}\right)^2 \\ &\quad + \left(\frac{\Delta\epsilon_{trig}}{\epsilon_{trig}}\right)^2 + \left(\frac{\Delta ID_{SF}}{ID_{SF}}\right)^2 \end{aligned}$$

where:

- $\frac{\Delta(L\epsilon_{z < 60})}{L\epsilon_{z < 60}}$  is the uncertainty due to the efficiency of the  $|z_0| \leq 60$  cm cut
- $\frac{\Delta A_{ee\gamma}}{A_{ee\gamma}}$  is the uncertainty in the  $Z\gamma$  acceptance calculation
- $\frac{\Delta\epsilon_{trig}}{\epsilon_{trig}}$  is the uncertainty in the trigger efficiency measurement

- $\frac{\Delta ID_{SF}}{ID_{SF}}$  is the uncertainty in the total efficiency scale factor measurement

Finally, the uncertainty on the acceptance term can be expanded to:

$$\left(\frac{\Delta A_{ee\gamma}}{A_{ee\gamma}}\right)^2 = \left(\frac{\Delta A_{ee\gamma}}{A_{ee\gamma}}\right)_{QCD}^2 + \left(\frac{\Delta A_{ee\gamma}}{A_{ee\gamma}}\right)_{PDF}^2 + \left(\frac{\Delta A_{ee\gamma}}{A_{ee\gamma}}\right)_{EM}^2$$

where:

- $\left(\frac{\Delta A_{ee\gamma}}{A_{ee\gamma}}\right)_{QCD}^2$  is the uncertainty due to the parton level generation difference from the LO program versus the NLO program
- $\left(\frac{\Delta A_{ee\gamma}}{A_{ee\gamma}}\right)_{PDF}^2$  is the uncertainty from PDF
- $\left(\frac{\Delta A_{ee\gamma}}{A_{ee\gamma}}\right)^2$  is uncertainty due to central/plug EM energy scale

Table 9.5 summaries all the uncertainties considered for the  $Z\gamma$  cross section. The main source of uncertainties on the cross section is signal statistics, luminosity measurement and background estimation.

## 9.6 $Z\gamma$ Cross Section Measurement

### 9.6.1 Previous measurement

The previous CDF measurement of  $Z\gamma$  cross section was performed with  $200 \text{ pb}^{-1}$  of data. There are 36  $Z(ee)\gamma$  candidate events in the data sample. The main uncertainty on the cross section is due to limited statistics. The current measurement is based on the data with a total integrated luminosity of  $1.07 \text{ fb}^{-1}$ . This gives a factor of 5 improvement in the sample statistics. The loose Z selection (described in Chapter 6)

**Table 9.3:** A summary of the uncertainties for the  $ee\gamma$  cross-section calculation and their correlations between CC and CP channels. A 'x' indicates the uncertainty is applied to that channel and thus correlated to the other channel with the same systematic.

Channel	$Z_{CC}\gamma$		$Z_{CP}\gamma$			
Source	% Uncertainty	% on $\sigma(Z_{CC}\gamma)$	% Uncertainty	% on $\sigma(Z_{CP}\gamma)$	CC	CP
Signal Statistics	7.4	8.0	7.0	8.5		
Luminosity	5.8	5.8	5.8	5.8		
$\gamma$ energy scale	3	2	3	2	x	x
$\gamma$ conversion rate	2	2	2	2	x	x
$\gamma$ ID efficiency	3	3	3	3	x	x
e energy scale	1	2.5	1	2.5	x	x
Central e ID	1	2	1	1	2x	x
Plug e ID	—	—	2	2		x
Trig efficiency	1	1	1	1	x	x
Acceptance	1	1	1	1	x	x
$\gamma$ + Jet bkg	63	0.7	45	3.2	x	x
Z + Jet bkg	38	2.5	39	5.9	x	x
Total Systematic		6.0		8.6		

doubles the final  $Z\gamma$  acceptance. The size of the  $Z\gamma$  sample used in this analysis is a factor of 10 larger than the previous measurement.

### 9.6.2 $Z\gamma$ Cross Section Result

The  $Z\gamma$  cross section using  $1.07 \text{ fb}^{-1}$  of data is presented in Table 9.6.2. There are 390  $ee\gamma$  events observed in data compared to the SM prediction of  $375.3 \pm 25.2$  events. The measured cross section is  $4.7 \pm 0.6 \text{ pb}$  compared to the theory prediction of  $4.5 \pm 0.4 \text{ pb}$ . The  $Z\gamma$  event kinematics distribution plots are shown in Figure 9.1. The distributions shown are the photon  $E_t$ , the three body invariant mass  $M_{ee\gamma}$ , the di-lepton mass  $M_{ee}$  and the separation between the two electrons and the photon. Data (“+” in black) is compared to the SM prediction (blue curve). The Z + jet

background, where a jet is mis-identified as photon, is plotted in pink. The  $\gamma + \text{jet}$  background, where a jet is mis-identified as an electron, is plotted in green. There is good agreement with the SM predictions for all kinematic distributions.

**Table 9.4:** Input parameters to the  $ee\gamma$  cross-section calculation,  $1074\text{pb}^{-1}$ .  $E_t^\gamma > 7$  GeV,  $\Delta R_{e\gamma} > 0.7$  and  $M_{ee} > 40$  GeV/ $c^2$ .

Z $\gamma$ type	eeg
Photon type	Central Photon
Zee type	CC + CP
$\int \mathcal{L} dt (\text{pb}^{-1})$	1074
K-Factor	1.35
$\sigma_{LO}(\text{pb})$	3.4
$\sigma_{NLO}(\text{pb})$	$4.5 \pm 0.4$
$\sigma^{obs}(\text{pb})$	$4.7 \pm 0.3(\text{stat.}) \pm 0.4(\text{syst.}) \pm 0.3(\text{lum})$
$N_{\gamma+Jet}^{bkg}$	$13.9 \pm 7.1$
$N_{Z+Jet}^{bkg}$	$51.6 \pm 14.1$
$N_{SM}^{exp}$	$309.8 \pm 16.6$
$N_{SM}^{exp} + N_{QCD}^{bkg}$	$375.3 \pm 22.9$
$N^{obs}$	390

Figure 9.2 shows the two-dimensional mass distribution of the Z $\gamma$  events. The Z $\gamma$  sample is further divided into two subsets depending on the three-body mass  $M_{ee\gamma}$  of the events. The measurement for the low mass region ( $M_{ee\gamma} < 100$  GeV/ $c^2$ ), dominated by  $Z \rightarrow ee\gamma$  final state radiation (FSR), is shown in Table 9.6.2. There are 236 FSR  $ee\gamma$  events observed in data compared to the SM prediction of  $224.1 \pm 11.7$  events. The measured cross section is  $3.5 \pm 0.4$  pb compared to the theory prediction of  $3.3 \pm 0.3$  pb. The FSR event kinematics are shown in Figure 9.3. Table 9.6.2 is the cross section result for events with  $M_{ee\gamma} > 100$  GeV/ $c^2$  and is predominately due to events with photon emission from initial state radiation (ISR). There are 154 ISR  $ee\gamma$  events observed in data compared to the SM prediction of  $151.2 \pm 13.5$  events. The measured cross section is  $1.2 \pm 0.2$  pb compared to the theory prediction of 1.2

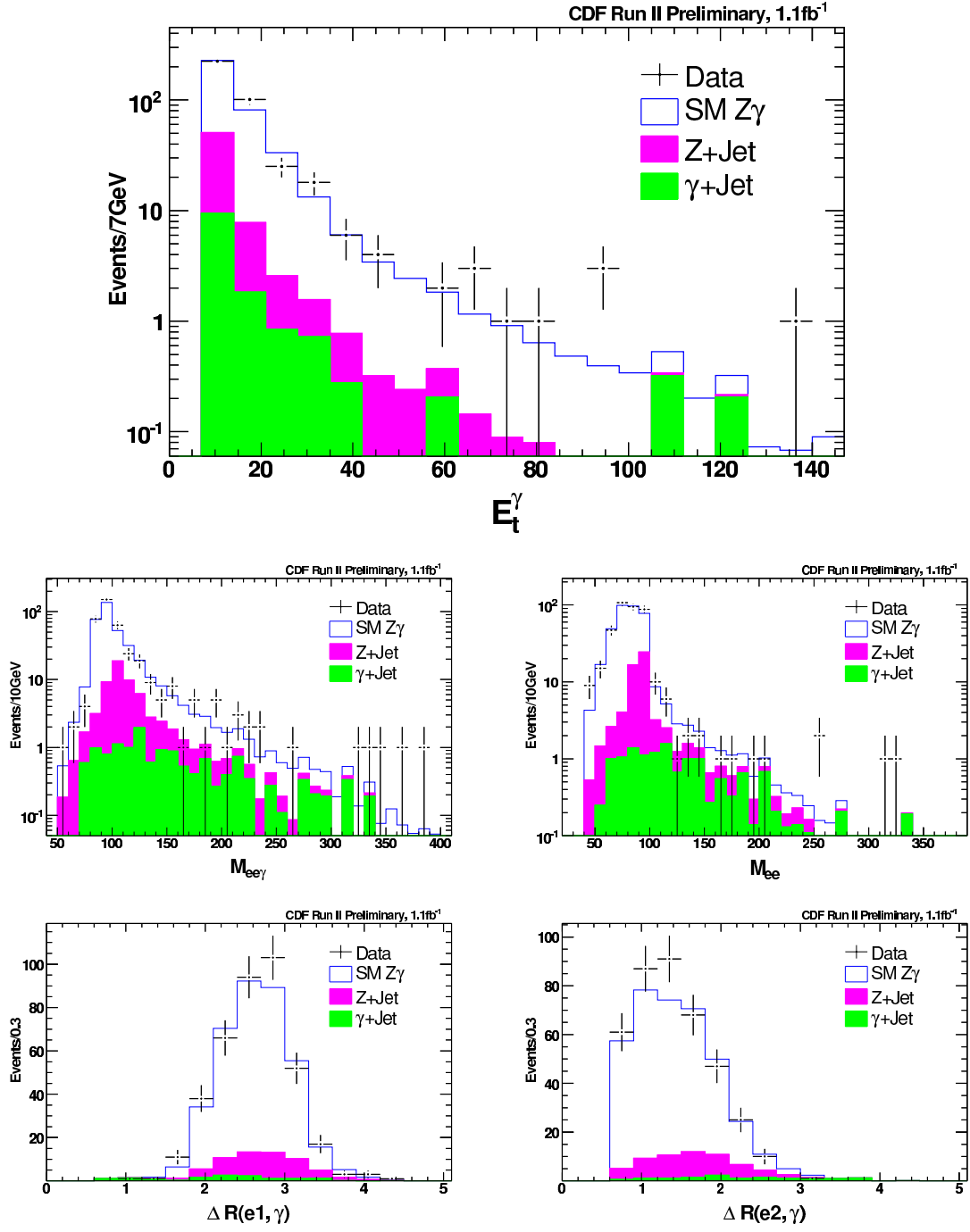


**Figure 9.1:**  $ee\gamma$  event kinematics.  $E_t^\gamma > 7$  GeV,  $\Delta R_{e\gamma} > 0.7$ ,  $M_{ee} > 40$  GeV/ $c^2$ .

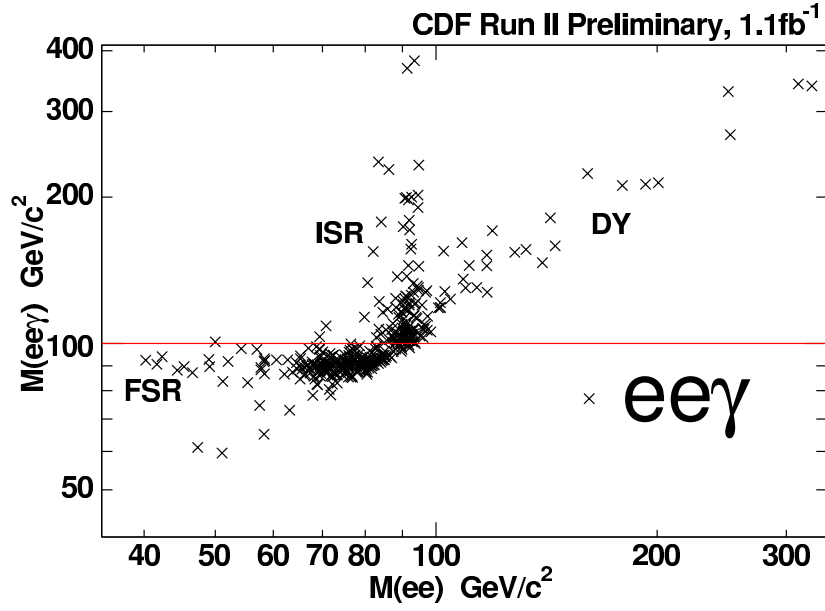


**Figure 9.2:** Data  $M_{ee} - M_{ee\gamma}$  Distribution, CC + CP ,  $1\text{fb}^{-1}$ , 7 GeVphoton  $E_t$  cut.

$\pm 0.1$  pb. The ISR event kinematics are shown in Figure 9.4. The ISR sample is used to probe anomalous triple gauge boson couplings (see Chapter 10).

**Table 9.5:** Input parameters to the FSR  $ee\gamma$  cross-section calculation,  $1074\text{pb}^{-1}$ .  $E_t^\gamma > 7$  GeV,  $\Delta R_{e\gamma} > 0.7$ ,  $M_{ee} > 40$  GeV/ $c^2$  and  $M_{ee\gamma} < 100$  GeV/ $c^2$ .

Z $\gamma$ type	FSR
Photon type	Central Photon
Zee type	CC + CP
$\int \mathcal{L} dt (\text{pb}^{-1})$	1074
K-Factor	1.36
$\sigma_{LO}(\text{pb})$	2.4
$\sigma_{NLO}(\text{pb})$	$3.3 \pm 0.3$
$\sigma^{obs}(\text{pb})$	$3.5 \pm 0.2(\text{stat.}) \pm 0.2(\text{syst.}) \pm 0.2(\text{lum})$
$N_{\gamma+Jet}^{bkg}$	$2.4 \pm 1.6$
$N_{Z+Jet}^{bkg}$	$12.5 \pm 3.0$
$N_{SM}^{exp}$	$209.2 \pm 11.2$
$N_{SM}^{exp} + N_{QCD}^{bkg}$	$224.1 \pm 11.7$
$N^{obs}$	236

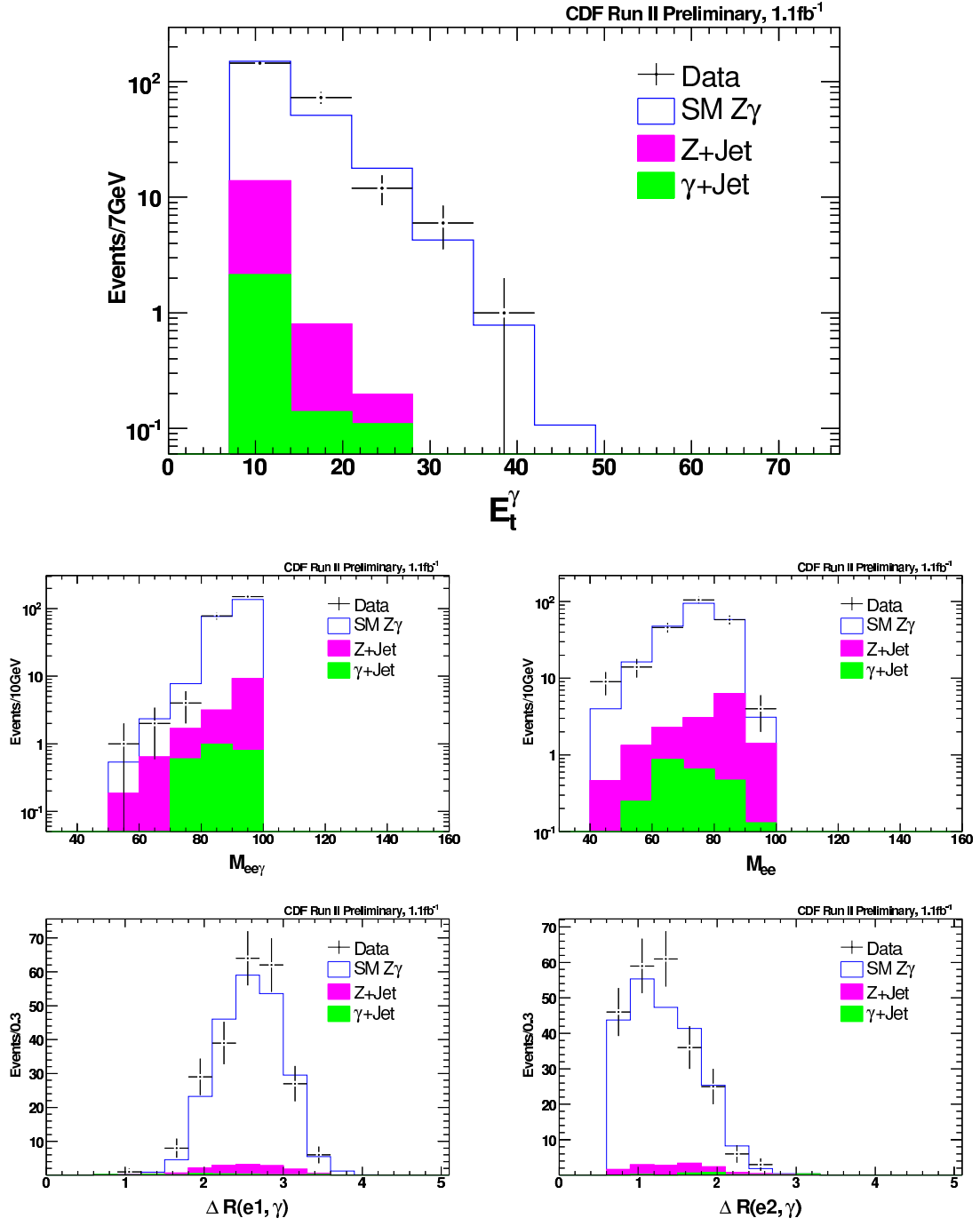


**Figure 9.3:** FSR  $ee\gamma$  events,  $E_t^\gamma > 7$  GeV,  $\Delta R_{e\gamma} > 0.7$ ,  $M_{ee} > 40$  GeV/ $c^2$  and  $M_{ee\gamma} \leq 100$  GeV/ $c^2$ .

**Table 9.6:** Input parameters to the ISR  $ee\gamma$  cross-section calculation,  $1074pb^{-1}$ .  
 $E_t^\gamma > 7$  GeV,  $\Delta R_{e\gamma} > 0.7$ ,  $M_{ee} > 40$  GeV/ $c^2$  and  $M_{ee\gamma} > 100$  GeV/ $c^2$ .

Z $\gamma$ type	ISR
Photon type	Central Photon
Zee type	CC + CP
$\int \mathcal{L} dt (pb^{-1})$	1074
K-Factor	1.33
$\sigma_{LO}(pb)$	0.9
$\sigma_{NLO}(pb)$	$1.2 \pm 0.1$
$\sigma^{obs}(pb)$	$1.2 \pm 0.1(\text{stat.}) \pm 0.2(\text{syst.}) \pm 0.1(\text{lum})$
$N_{\gamma+Jet}^{bkg}$	$11.5 \pm 5.6$
$N_{Z+Jet}^{bkg}$	$39.0 \pm 11.1$
$N_{SM}^{exp}$	$100.6 \pm 5.4$
$N_{SM}^{exp} + N_{QCD}^{bkg}$	$151.2 \pm 13.5$
$N^{obs}$	154



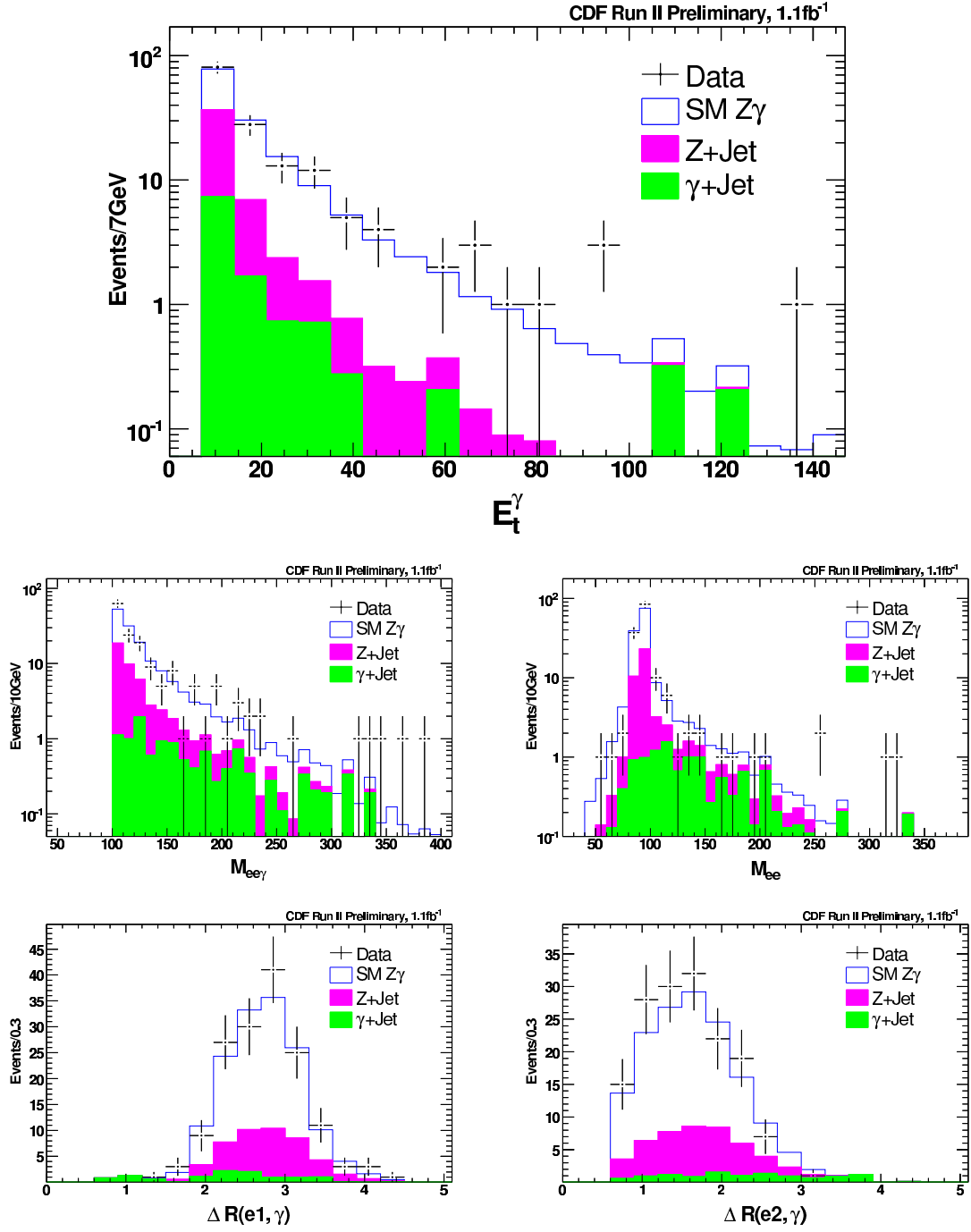


Figure 9.4: ISR  $ee\gamma$  events,  $E_t^\gamma > 7$  GeV,  $\Delta R_{e\gamma} > 0.7$ ,  $M_{ee} > 40$  GeV/ $c^2$  and  $M_{ee\gamma} > 100$  GeV/ $c^2$ .

### 9.6.3 $Z\gamma$ Event Display

In this section, a few events with very high  $M_{ee}$ ,  $M_{ee\gamma}$  or photon  $E_t$  are displayed.

#### The Highest Photon $E_t$ Event

The kinematic of the highest photon  $E_t$  ( $= 135$  GeV) event is as following:

**Table 9.7:** The highest  $E_t^\gamma$   $Z\gamma$  event

Run	Event	Z Type	$E_t^\gamma$	$M_{ee\gamma}$	$M_{ee}$	$P_t^{ee\gamma}$	$E_t^{e1}$	$E_t^{e2}$	$\eta^\gamma$	$\eta^{e1}$	$\eta^{e2}$
161830	69435	CC	135	368	92	17	137	27	-0.6	0.8	-0.2

Figure 9.5 shows the COT view and the calorimeter tower view of this event.

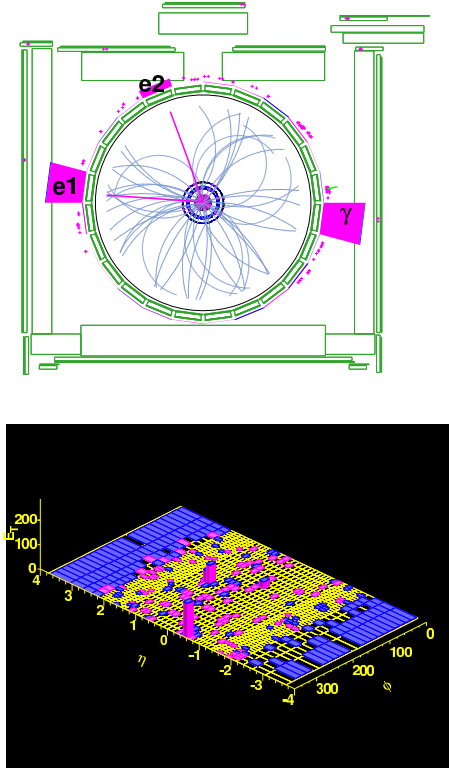


**Figure 9.5:** The COT view and the calorimeter tower view of the highest photon  $E_t$  event, event 69435 in run 161830.

## The Highest $M_{ee\gamma}$ Event

The kinematic of the highest  $M_{ee\gamma}$  ( $= 381 \text{ GeV}/c^2$ ) event is as following:

**Table 9.8:** The highest  $M_{ee\gamma}$   $Z\gamma$  event

Run	Event	Z Type	$E_t^\gamma$	$M_{ee\gamma}$	$M_{ee}$	$P_t^{ee\gamma}$	$E_t^{e1}$	$E_t^{e2}$	$\eta^\gamma$	$\eta^{e1}$	$\eta^{e2}$
161555	619905	CP	83	381	93	9	35	56	-0.9	0.4	2.2

Figure 9.6 shows the COT view and the calorimeter tower view of this event.

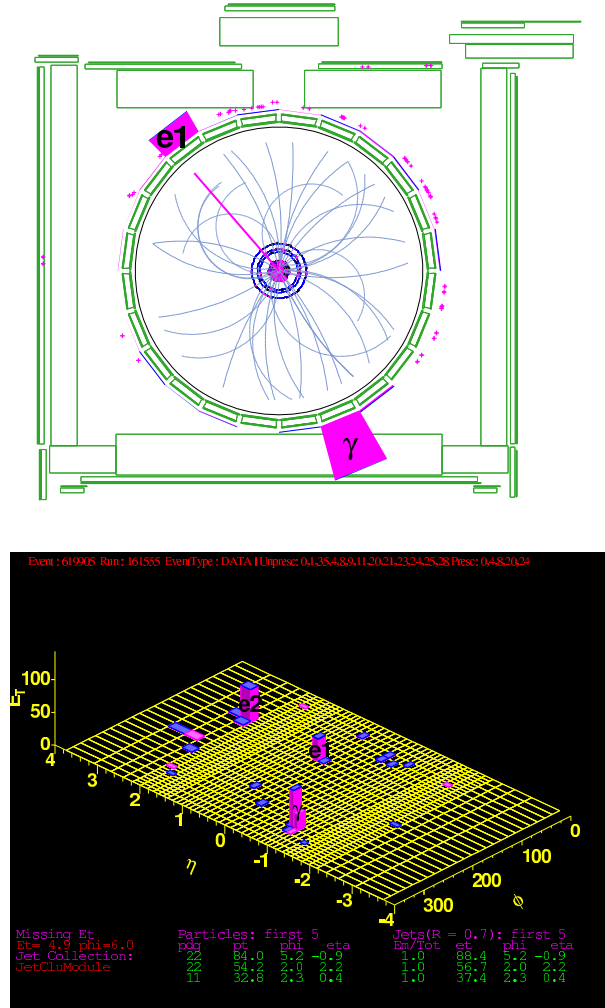


**Figure 9.6:** The COT view and the calorimeter tower view of the highest  $M_{ee\gamma}$  event, event 619905 in run 161555.

## The Highest $P_t^{ee\gamma}$ Event

The kinematic of the highest  $P_t^{ee\gamma}$  ( $= 142 \text{ GeV}/c$ ) event is as following:

**Table 9.9:** The highest  $P_t^{ee\gamma}$  event

Run	Event	$E_t^\gamma$	$M_{ee\gamma}$	$M_{ee}$	$\cancel{E}_t$	$P_t^{ee\gamma}$	$E_t^{e1}$	$E_t^{e2}$	$\eta^\gamma$	$\eta^{e1}$	$\eta^{e2}$
162857	3732149	10	88	44	42	142	101	46	0.21	-0.97	-0.33

Figure 9.7 shows the COT view and the calorimeter tower view of this event.

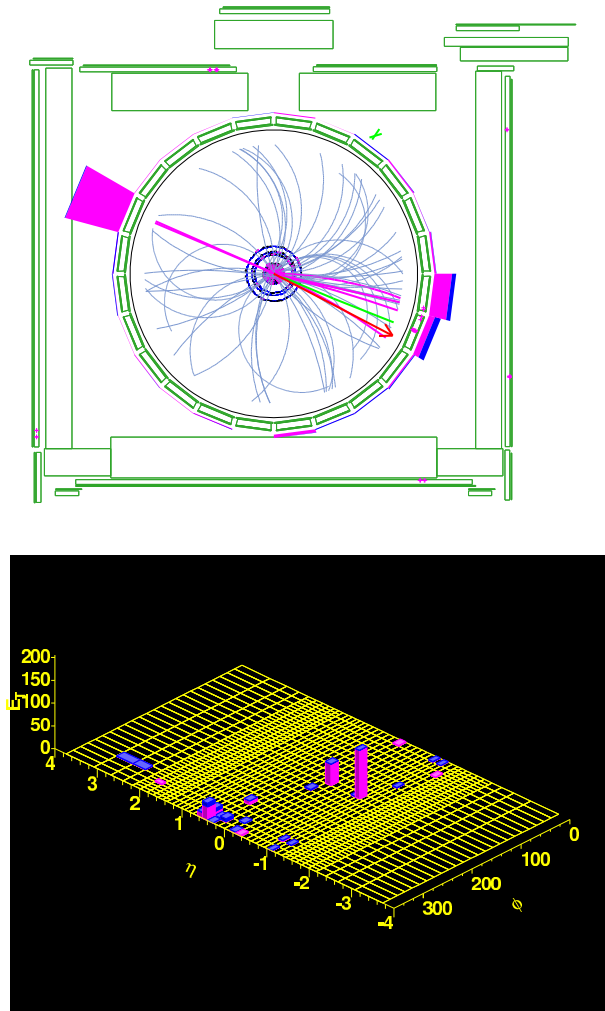


**Figure 9.7:** The COT view and the calorimeter tower view of the highest  $P_t^{ee\gamma}$  event, event 3732149 in run 162857 .

## A Very High $M_{ee}$ Event

The kinematic of a very high  $M_{ee}$  ( $= 251 \text{ GeV}/c^2$ ) event is as following:

**Table 9.10:** The very high  $M_{ee}$   $Z\gamma$  event

Run	Event	Z Type	$E_t^\gamma$	$M_{ee\gamma}$	$M_{ee}$	$P_t^{ee\gamma}$	$E_t^{e1}$	$E_t^{e2}$	$\eta^\gamma$	$\eta^{e1}$	$\eta^{e2}$
186048	5975330	CP	19	269	251	60	64	83	0.5	-1.05	1.3

Figure 9.8 shows the COT view and the calorimeter tower view of this event.

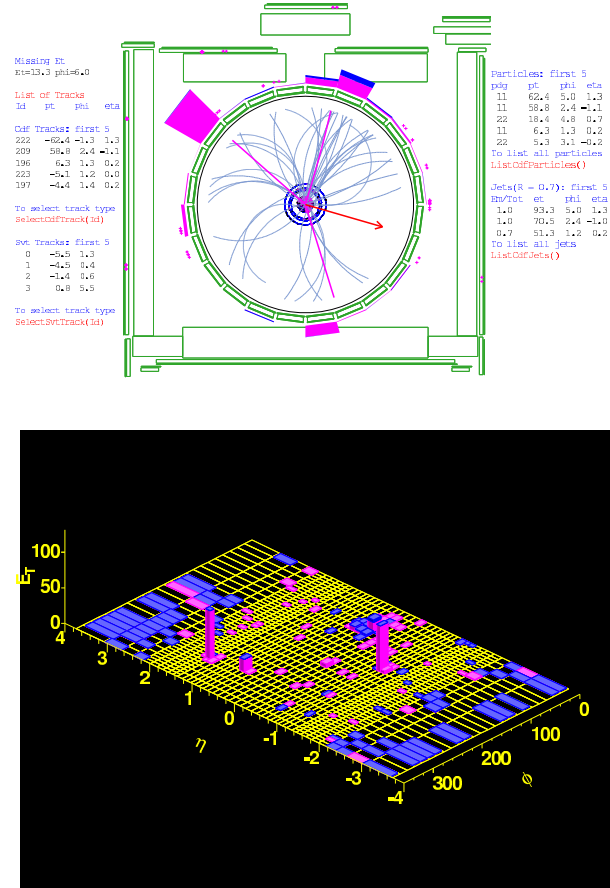


**Figure 9.8:** The COT view and the calorimeter tower view of a very high  $M_{ee}$  event, event 5975330 in run 186048.

# Chapter 10

## Anomalous Triple Gauge Boson Couplings

The Standard Model Electroweak theory makes precise predictions for the couplings between gauge bosons. Gauge boson pair production provides direct tests of the triple gauge boson couplings. Any non Standard Model (anomalous) couplings enhance gauge boson pair production cross-section and would indicate new physics beyond the Standard Model. This chapter describes a search for anomalous gauge couplings (AGC) in  $Z\gamma$  production using the  $Z \rightarrow ee$  decay channel with  $1 \text{ fb}^{-1}$  of  $p\bar{p}$  integrated luminosity.

### 10.1 Current Limits on $ZZ\gamma$ and $Z\gamma\gamma$ Couplings

The parameters used to describe  $ZZ\gamma$  and  $Z\gamma\gamma$  vertices are  $h_i^V$  ( $i = 1 - 4$ ,  $V = Z$  or  $\gamma$ , see Section 5.1.2). The current published limits on  $ZZ\gamma$  and  $Z\gamma\gamma$  couplings are summarized in Table 10.1. CDF Run I limits are based on  $20 \text{ pb}^{-1}$  of  $p\bar{p}$  integrated luminosity. Limits from the Tevatron D0 experiment are measured with  $1.1 \text{ fb}^{-1}$  of  $p\bar{p}$  integrated luminosity.

**Table 10.1:** 95% C.L. limits on  $Z\gamma$  anomalous couplings.

Experiment Luminosity( $\text{fb}^{-1}$ )	CDF Run I [20] 0.02	LEP II [12] 0.7	D0 [21] 1.1
$h_3^Z$	-3.0, 2.9	-0.20, 0.07	-0.083, 0.082
$h_4^Z$	-0.7, 0.7	-0.05, 0.12	-0.005, 0.005
$h_3^\gamma$	-3.1, 3.1	-0.049, 0.008	-0.085, 0.084
$h_4^\gamma$	-0.8, 0.8	-0.02, 0.034	-0.005, 0.005

## 10.2 Anomalous Gauge Couplings (AGC)

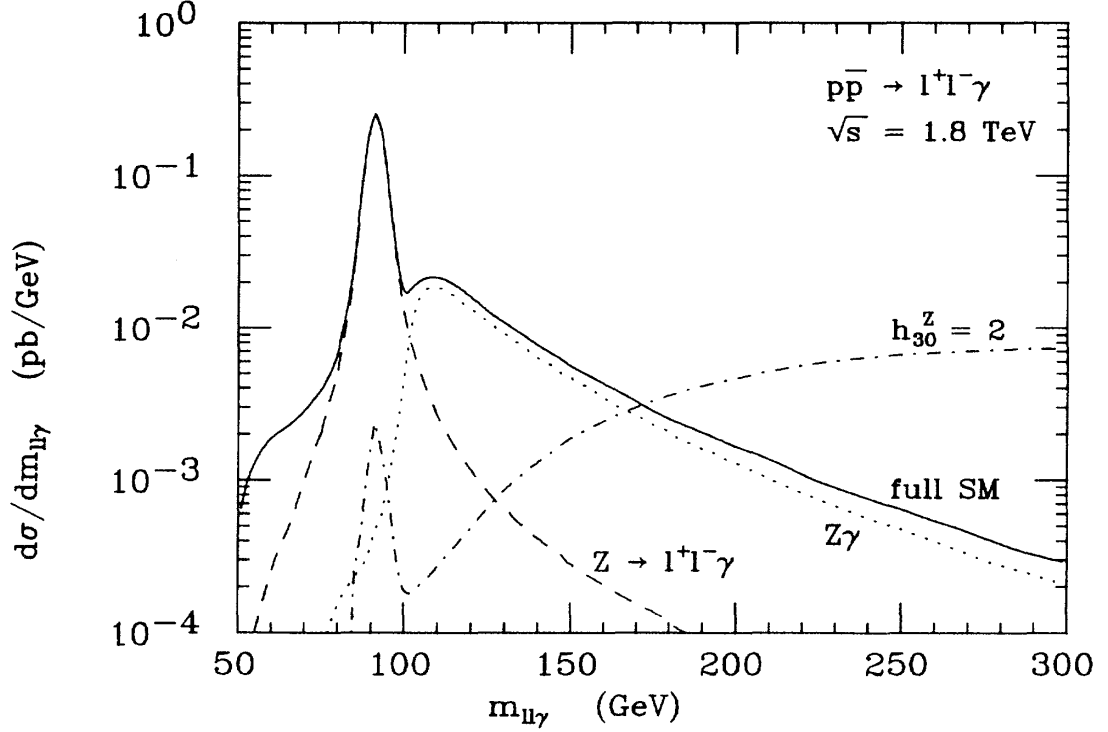


**Figure 10.1:**  $ll\gamma$  Mass distribution in  $Z\gamma$  production [50]. High mass region is most sensitive to anomalous couplings. Dashed line: FSR; dotted line: ISR; solid curve: SM; dash-dotted curve: anomalous couplings.

The three-body invariant mass distributions from the SM contribution and from an example of a anomalous coupling are plotted in Figure 10.1. The prediction of the SM  $Z\gamma$  production is shown with the solid line. This has contributions from the initial state radiation process (dotted line) and the final state radiation process (dashed line). The Feynman diagrams for the ISR process are shown in Figure 5.4 (a) and (b). The Feynman diagrams for the FSR process are shown in Figure 5.4 (c) and (d). For comparison, the contribution from a non-zero triple gauge boson coupling is plotted in dash dotted line. As shown in the plot, the high mass region

is most sensitive to anomalous couplings. We use the subset of  $Z\gamma$  events with  $M_{ee\gamma} > 100 \text{ GeV}/c^2$  to probe anomalous couplings. Table 9.6.2 shows the result of the cross section for this region ( $M_{ee\gamma} > 100 \text{ GeV}/c^2$ ). The data agrees well with the SM prediction. Figure 10.2 shows the  $E_t^\gamma$  distribution of the signal and background. Data from the experiment (+) is compared to the prediction of the SM for  $Z\gamma$  production and backgrounds (in blue). The background from  $Z + \text{jet}$  events where a jet is mis-identified as a photon is shown in pink and the background from  $\gamma + \text{jet}$  events is shown in green. The  $E_t^\gamma$  distribution is used to extract limits on  $Z\gamma$  anomalous couplings. The red dashed line shows the photon  $E_t$  distribution for a non-zero anomalous coupling. It shows that the high  $E_t^\gamma$  region is most sensitive to deviation from the SM prediction.

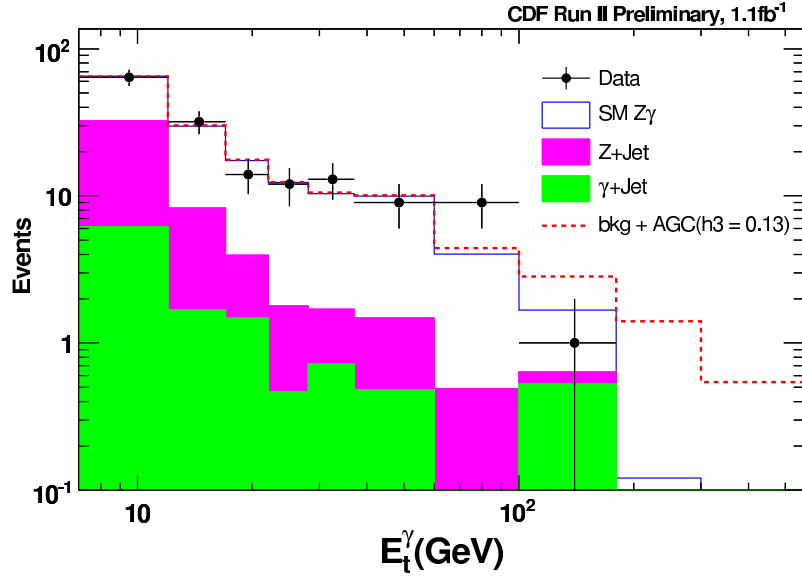


**Figure 10.2:** Photon  $E_t$  distribution for  $ee\gamma$  events with  $M_{ee\gamma} > 100 \text{ GeV}/c^2$ . Electron  $1\text{fb}^{-1}$ .



## 10.3 Anomalous Coupling Monte Carlo Samples

A  $p\bar{p} \rightarrow Z \gamma + X$  event generator (ZGAMMA [50]) is used to generate  $Z\gamma$  production with various anomalous couplings. For  $h_3^V$  couplings, 400 samples are generated in the range  $[-0.2, 0.2]$ , in steps of 0.001. For  $h_4^V$  couplings, 400 samples are generated in the range  $[-0.002, 0.002]$ , in steps of 0.0001.

## 10.4 Reconstruction Efficiency

To avoid full CDF detector simulation for every event sample, an universal efficiency curve is applied to generator level samples to take into account the reconstruction efficiency of the electrons and photons.

The universal efficiency is defined as  $\epsilon(E_t^\gamma) = N_{Rec}(E_t^\gamma) / N_{Accp}(E_t^\gamma)$ , where the cuts applied to denominator and numerator are listed below:

- Denominator: events with acceptance cuts on generator level quantities.
  - $E_t^\gamma > 7 \text{ GeV}$ ,  $\Delta R_{e\gamma} (e, \gamma) > 0.7$ ,  $M_{ee\gamma} > 100 \text{ GeV}/c^2$ .
  - $|\eta^\gamma| < 1.1$ ,  $E_t^e > 20$ ,  $|\eta^e| < 1.1(C)$ ,  $|\eta^e| < 2.8(P)$
- Numerator: events passing selection cuts on reconstructed quantities.
  - ISR  $Z\gamma$  events selection cuts (see Section 9.1)
  - No cuts are apply to generator level quantities. Generated events outside our acceptance range do not contribute to the denominator but can contribute to the numerator due to the detector resolution effects.

Figure 10.3 plots the efficiency as a function of photon  $E_t$  measured from the SM  $Z\gamma$  detector simulation. The upper curves are for  $ee\gamma$  events with two central

electrons; the lower curves are for  $ee\gamma$  events with one central and one plug electron. The efficiency curves measured from one AGC ( $h_3^Z = 0.25$ ) sample are also shown. The difference is assigned as systematic uncertainty for the universal efficiency.

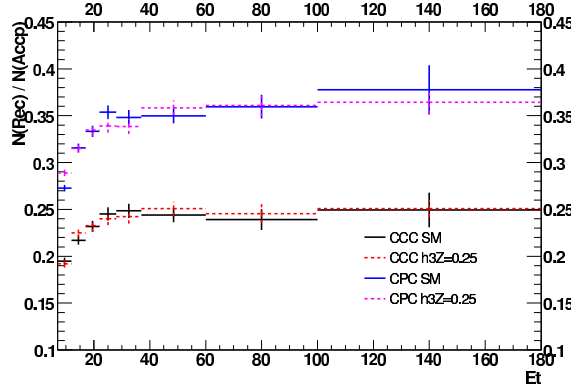


**Figure 10.3:** Universal efficiency  $N_{Rec}(E_t^\gamma) / N_{Accp}(E_t^\gamma)$  for ISR  $Z\gamma$  events with CC Z's (upper curves) and CP Z's (lower curves). SM vs AGC.

## 10.5 Setting Limits on Anomalous Gauge Couplings

The limits on the gauge couplings are extracted using binned maximum likelihood method from  $E_t^\gamma$  spectra. The binned likelihood is calculated as following:

$$\mathcal{L} = \prod_i \frac{\mu_i^{N_i} e^{-\mu_i}}{N_i!} \quad (10.1)$$

where,

- $N_i$  is the number of data events observed in the  $i$ th bin in data
- $\mu_i$  is the number of expected signal plus background events ( $= S_i(h_3, h_4) + bkg_i$ )
- $S_i(h_3, h_4) = \sigma(h_3, h_4) * \text{KF} * \text{Acceptance} * \text{Efficiency} * \text{Luminosity}$

- $\sigma(h_3, h_4)$  is not equal to the SM value  $\sigma(h_3 = 0, h_4 = 0)$

A 95% limits are obtained by calculating the intergral of  $\mathcal{L}$ :

- $\int_A^B \mathcal{L} = 95\%$ , where A(B) is the lower (upper) limit

The likelihood distributions of the couplings  $h_{3,4}^{Z,\gamma}$  are shown in Figure 10.4 - 10.7.

The observed limits are listed in Table 10.2.

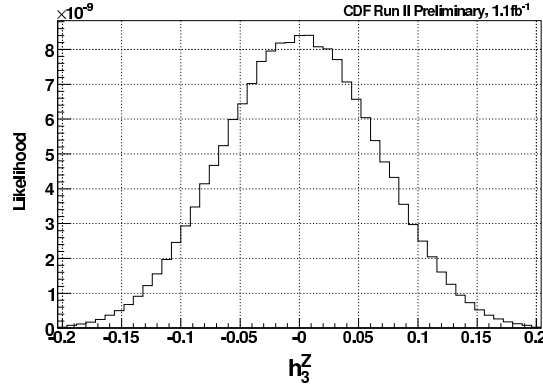


**Figure 10.4:** Likelihood distribution as a function of  $h_3^Z$  from data.  $h_3^Z$  95% C.L. observed limit: 0.124

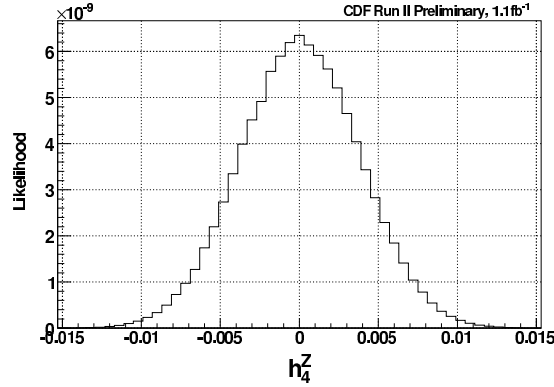


**Figure 10.5:** Likelihood distribution as a function of  $h_4^Z$  from data.  $h_4^Z$  95% C.L. observed limit: 0.0074.

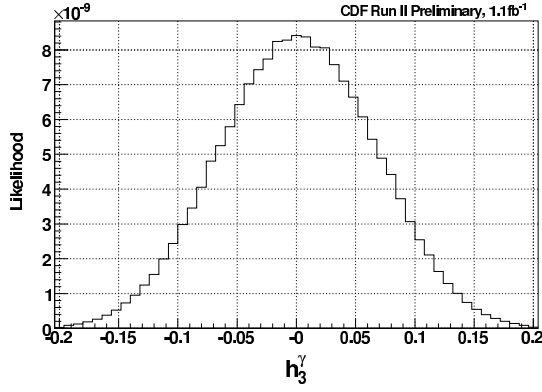


**Figure 10.6:** Likelihood distribution as a function of  $h_3^\gamma$  from data.  $h_3^\gamma$  95% C.L. observed limit: 0.13.

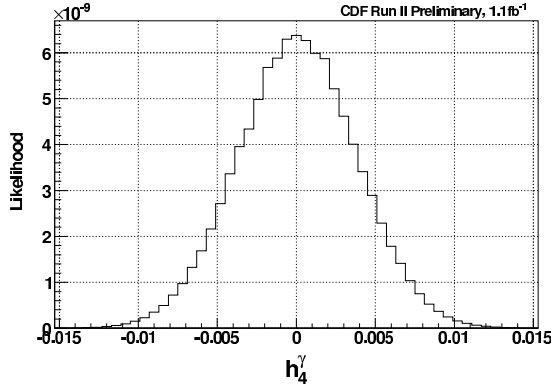


**Figure 10.7:** Likelihood distribution as a function of  $h_4^\gamma$  from data.  $h_4^\gamma$  95% C.L. observed limit: 0.0074.

### 10.5.1 Expected limits

A simulation of our experiment is used to obtain expected limits on the couplings. To generate one pseudo-experiment, we poisson smear the number of expected SM signal and background events. Then we throw random numbers to generate  $N_s(\text{PE})$  and  $N_b^i(\text{PE})$  events according to the SM signal and background  $E_t^\gamma$  distributions. Finally, a binned maximum likelihood is calculated using the generated pseudo-data as "data" and the 95% C.L. upper and lower limits are extracted. The pseudo-

experiments are repeated 200 thousand times and the upper and lower limits of the 95% C.L. limits are determined.

Figure 10.8 shows the distribution of the upper and lower limits obtained from pseudo-experiments for the AGC parameter  $h_3^Z$ . The average value is taken as the expected limit on  $h_3^Z$ .

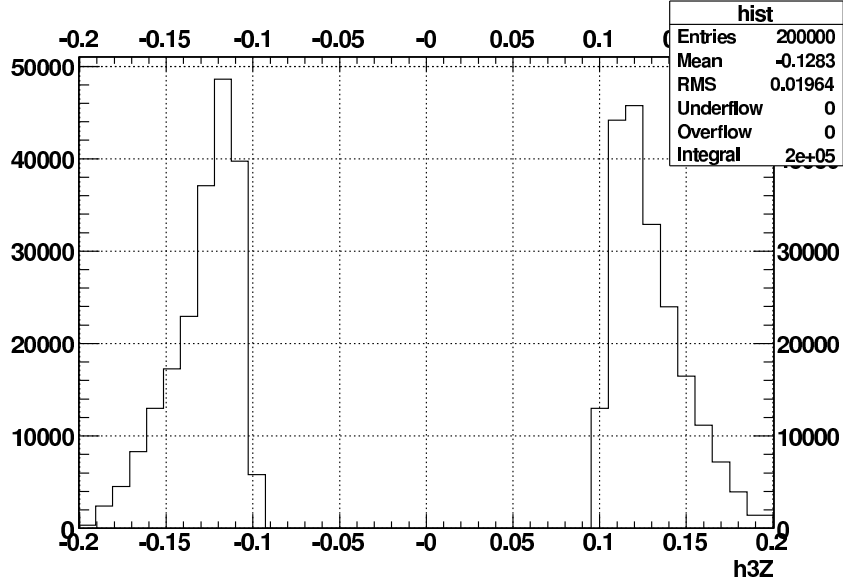


**Figure 10.8:** Expected lower and upper limit of  $h_3^Z$  from pseudo-experiments:  $[-0.128, 0.128]$ ,  $1\sigma = 0.0196$  (stat only).

### 10.5.2 Uncertainties on expected limits

Due to limited statistics at high  $E_t^\gamma$  bins (less than 5 events), the statistic uncertainty is the dominant error. The systematic uncertainties included in the calculation are the following:

- Bkg:  $N_b^i \pm \Delta N_b^i$ , Gaussian smearing with mean =  $N_b^i$ , width =  $\Delta N_b^i$
- Expected Signal: Gaussian mean =  $N^{exp}$ , width =  $\Delta N^{exp}$

- $N^{exp} = \text{LO Baur ME} \times \text{Acceptance} \times \epsilon(E_t^\gamma) \times \text{kF}(E_t^\gamma) \times \sigma^{LO} \times \mathcal{L}$
- 6% on luminosity
- 5% on  $\sigma_{th}^{LO}$
- 3% on  $\text{kF}(E_t^\gamma)$
- 3% on  $\epsilon(E_t^\gamma)$
- Other systematics already included in the cross-section measurement ( $\approx 5\%$ ), such as uncertainties on the electron and photon identification efficiencies, energy scale.

The expected limits for  $h_3^Z$  is  $|h_3^Z| < 0.128$ , with a statistical uncertainty of 0.0196. The uncertainty is 0.0199 if including both statistic and systematic uncertainties.

## 10.6 Results

The expected and observed limits of the couplings are summarized in Table 10.2. Limits for the four coupling parameters  $h_3^Z, h_4^Z, h_3^\gamma$  and  $h_4^\gamma$  are presented. The observed limits agree well with the expected limits within uncertainties.

**Table 10.2:** 95% C.L. limits on  $Z\gamma$  anomalous couplings using  $1\text{fb}^{-1}$  electron data.

	Observed Limits	Expected Limits
$ h_3^Z $	0.124	$0.128 \pm 0.020$
$ h_4^Z $	0.0074	$0.0079 \pm 0.0010$
$ h_3^\gamma $	0.126	$0.130 \pm 0.020$
$ h_4^\gamma $	0.0074	$0.0078 \pm 0.0010$

## 10.7 Combine $Z \rightarrow ee$ and $Z \rightarrow \mu\mu$ Channels

A measurement of  $Z\gamma$  production using the  $Z \rightarrow \mu\mu$  decay channel with  $2 \text{ fb}^{-1}$  of  $p\bar{p}$  integrated luminosity has been performed in parallel to this analysis [70]. Table 10.7 shows the measured  $Z\gamma$  cross section in the ISR dominant region with  $M_{l\gamma} > 100 \text{ GeV}/c^2$  using the  $Z \rightarrow \mu\mu$  decay channel. Table 10.7 shows the combined cross section result from the  $Z \rightarrow ee$  and  $Z \rightarrow \mu\mu$  data. There are 273 ISR  $ee\gamma$  events observed in data compared to the SM prediction of  $274.3 \pm 22.6$  events. The measured cross section is  $1.2 \pm 0.2 \text{ pb}$  compared to the theory prediction of  $1.2 \pm 0.1 \text{ pb}$ . There is excellent agreement with the SM predictions. The photon  $E_t$  distribution is shown in Figure 10.9. This is used to calculate the binned maximum likelihood function. The limits on the couplings are listed in Table 10.5. Our observed limits are slightly better than the limits from the D0 experiment by a few percent (see Table 10.1).

**Table 10.3:** Input parameters to the ISR  $\mu\mu\gamma$  cross-section calculation, 2007  $pb^{-1}$ .  $E_t^\gamma > 7 \text{ GeV}$ ,  $\Delta R_{l\gamma} > 0.7$ ,  $M_{ll} > 40 \text{ GeV}/c^2$  and  $M_{l\gamma} > 100 \text{ GeV}/c^2$ .

Z $\gamma$ type	ISR
Photon type	Central Photon
Lepton Channel	$\mu\mu\gamma$
$\int \mathcal{L} dt (pb^{-1})$	2007
K-Factor	1.3
$\sigma_{LO}(pb)$	0.9
$\sigma_{NLO}(pb)$	$1.2 \pm 0.1$
$\sigma^{obs}(pb)$	$1.2 \pm 0.1(\text{stat.}) \pm 0.1(\text{syst.}) \pm 0.1(\text{lum})$
$N_{Z+Jet}^{bkg}$	$30.5 \pm 8.8$
$N_{SM}^{exp}$	$92.6 \pm 4.5$
$N_{SM}^{exp} + N_{QCD}^{bkg}$	$123.1 \pm 9.9$
$N^{obs}$	119

**Table 10.4:** Input parameters to the ISR  $ee\gamma + \mu\mu\gamma$  cross-section calculation, 1074 (e) + 2007 ( $\mu$ )  $pb^{-1}$ .  $E_t^\gamma > 7$  GeV,  $\Delta R_{l\gamma} > 0.7$ ,  $M_{ll} > 40$  GeV/ $c^2$  and  $M_{ll\gamma} > 100$  GeV/ $c^2$ .

Z $\gamma$ type	ISR
Photon type	Central Photon
Lepton Channel	$ee\gamma + \mu\mu\gamma$
$\int \mathcal{L} dt (pb^{-1})$	1074 (e) + 2007 ( $\mu$ )
K-Factor	1.3
$\sigma_{LO}(pb)$	0.9
$\sigma_{NLO}(pb)$	$1.2 \pm 0.1$
$\sigma^{obs}(pb)$	$1.2 \pm 0.1(\text{stat.}) \pm 0.2(\text{syst.}) \pm 0.1(\text{lum})$
$N_{\gamma+Jet}^{bkg}$	$11.5 \pm 5.6$
$N_{Z+Jet}^{bkg}$	$69.5 \pm 19.9$
$N_{SM}^{exp}$	$193.2 \pm 9.0$
$N_{SM}^{exp} + N_{QCD}^{bkg}$	$274.3 \pm 22.6$
$N^{obs}$	273

**Table 10.5:** Limits (95% C.L.) for e +  $\mu$  combined

	Observed Limits	Expected Limits
$ h_3^Z $	0.083	$0.085 \pm 0.018$
$ h_4^Z $	0.0047	$0.0052 \pm 0.0009$
$ h_3^\gamma $	0.084	$0.086 \pm 0.017$
$ h_4^\gamma $	0.0047	$0.0051 \pm 0.0009$

## 10.8 Chapter Summary

A study of anomalous gauge couplings in  $p\bar{p} \rightarrow ll\gamma + X$  production using the CDF detector has been performed. The photon  $E_t$  distribution of  $ll\gamma$  events is used to set limits on the  $ZZ\gamma$  and  $Z\gamma\gamma$  couplings. These are the first limits measured using CDF Run II data. Our observed limits are slightly better than the limits from the D0 experiment by a few percent. A measurement of  $Z\gamma$  production using the  $Z \rightarrow \nu\nu$  decay channel with 2 fb $^{-1}$  of  $p\bar{p}$  integrated luminosity has been performed [71]. We plan to include the  $Z(\nu\nu)\gamma$  channel for setting anomalous coupling limits. With this



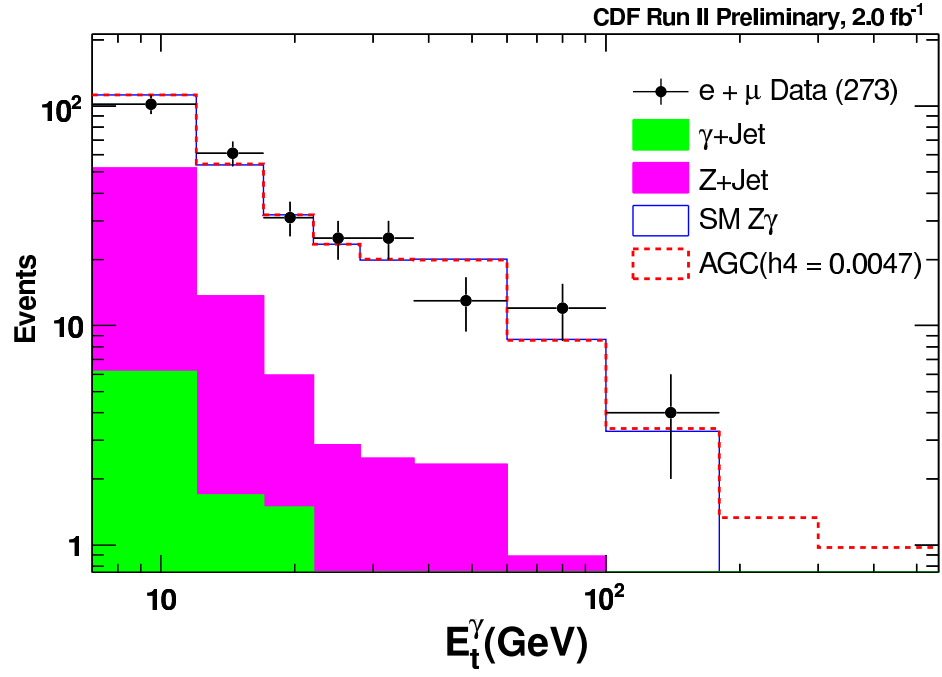


**Figure 10.9:** Photon  $E_t$  distribution for  $ee\gamma$  events with  $M_{ee\gamma} > 100 \text{ GeV}/c^2$ . Electron  $1 \text{ fb}^{-1}$  + Muon  $2 \text{ fb}^{-1}$ .

addition, we expect to obtain limits that are better than any other single experiment.

# Chapter 11

## Summary and Conclusion

The  $p\bar{p} \rightarrow Z\gamma + X \rightarrow e^+e^-\gamma + X$  production cross section is measured using the CDF detector with  $1.1 \text{ fb}^{-1}$  of  $p\bar{p}$  integrated luminosity at  $\sqrt{s} = 1.96 \text{ TeV}$ . The cross section is compared to the theoretical prediction based on Standard Model electroweak theory. The measured cross section agrees well with the Standard Model theory prediction.

A loose electron selection is developed which doubles the size of the inclusive  $Z \rightarrow ee$  sample. The loose Z selection is validated by measuring the cross section of the inclusive  $Z \rightarrow ee$  production. Good agreement is found in the measured Z boson cross section when compared with the Standard Model prediction.

A new method to measure the photon detection efficiency from a pure photon sample is presented. The efficiency measured from the data agrees well with the prediction from the simulation of the CDF detector. This is the first photon efficiency measured directly from a photon sample using the CDF detector.

From the large Z sample, events with an additional photon with  $E_t^\gamma > 7 \text{ GeV}$  are selected. The cross section for  $p\bar{p} \rightarrow e^+e^-\gamma + X$  production is measured for the kinematic region of  $E_t^e > 20 \text{ GeV}$ ,  $E_t^\gamma > 7 \text{ GeV}$ ,  $\Delta R_{e\gamma} > 0.7$  and  $M_{ee} > 40 \text{ GeV}/c^2$ . There are 390  $ee\gamma$  events found with  $1.1 \text{ fb}^{-1}$  of data, compared to the SM prediction of  $375.3 \pm 25.2$  events. The measured cross section is  $4.7 \pm 0.6 \text{ pb}$ . The theoretical prediction based on SM electroweak theory for the cross section is  $4.5 \pm 0.4 \text{ pb}$ . The cross section and kinematic distributions of the  $ee\gamma$  events are in good agreement with the theoretical prediction.

A high mass sample with  $M_{ee\gamma} > 100 \text{ GeV}/c^2$  is selected to study anomalous triple gauge boson couplings. There are 154  $ee\gamma$  candidate events in this mass range, compared to the SM prediction of  $151.2 \pm 13.5$  events. The measured cross section is  $1.2 \pm 0.2 \text{ pb}$  compared to the theoretical prediction of  $1.2 \pm 0.1 \text{ pb}$ . Good agreement is found in the kinematic distributions compared with the theoretical prediction. The photon  $E_t$  distribution is used to set limits on the  $ZZ\gamma$  and  $Z\gamma\gamma$  couplings. These are the first limits measured using CDF Run II data. The result of this thesis will be combined with measurements in the  $Z \rightarrow \mu\mu$  and  $Z \rightarrow \nu\nu$  channels. We expect the combined limits to be better than any other single experiment, and will provide important test of the interaction of the photon and the Z boson.

# Appendix

# Appendix A

## Electroweak Theory

In this chapter, a theoretical overview of Electroweak theory [4] is presented.

### A.1 Local Gauge Symmetry

We begin with the Dirac field  $\psi(x)$  and demand that the Lagrangian should be invariant under the following local phase transformation:

$$\psi(x) \rightarrow e^{i\alpha(x)}\psi(x). \quad (\text{A.1})$$

It can be shown that the following mass term is invariant under such transformation

$$m\bar{\psi}\psi, \quad (\text{A.2})$$

where

$$\bar{\psi} = \psi^\dagger \gamma^0 \quad (\text{A.3})$$

Next, we define a derivative  $D_\mu(x)$ , called the *covariant derivative*, and require that it transforms in the same way as the field  $\psi(x)$ :

$$D_\mu\psi(x) \rightarrow e^{i\alpha(x)}D_\mu\psi(x). \quad (\text{A.4})$$

The covariant derivative has the form:

$$D_\mu \psi(x) = \partial_\mu \psi(x) + ieA_\mu(x), \quad (\text{A.5})$$

where  $A_\mu(x)$  is a vector field. It transforms as

$$A_\mu(x) \rightarrow A_\mu(x) - \frac{1}{e} \partial_\mu \alpha(x). \quad (\text{A.6})$$

Thus the following term is invariant under the local phase transformation:

$$\bar{\psi}(i\not{D})\psi, \quad (\text{A.7})$$

where

$$\not{D} = D_\mu \gamma^\mu. \quad (\text{A.8})$$

Next, we try to find a kinetic energy term for the field  $A_\mu$  that is invariant. Eqs. (A.4) shows that the covariant derivative  $D_\mu \psi$  has the same transformation law as the field  $\psi(x)$ . Thus the second covariant derivative of  $\psi$  also transforms in the same way as the field  $\psi$ . We finds:

$$[D_\mu, D_\nu] \psi(x) \rightarrow e^{i\alpha(x)} [D_\mu, D_\nu] \psi(x). \quad (\text{A.9})$$

However, by using Eqs. (A.5), we get:

$$[D_\mu, D_\nu] \psi = ie(\partial_\mu A_\nu - \partial_\nu A_\mu) \cdot \psi = ieF_{\mu\nu} \psi. \quad (\text{A.10})$$

Thus,

$$[D_\mu, D_\nu] = ieF_{\mu\nu}. \quad (\text{A.11})$$

Since  $\psi(x)$  accounts for the entire transformation law on the right side of the Eqs. (A.9), the factor  $F_{\mu\nu}$  must be invariant.

Now, the invariant Lagrangian is:

$$\mathcal{L} = \bar{\psi}(i\not{D})\psi - m\bar{\psi}\psi - \frac{1}{4}(F_{\mu\nu})^2 \quad (\text{A.12})$$

which is the familiar QED Lagrangian. Therefore, by requiring local gauge symmetry, we have now recovered the QED Lagrangian. The local gauge symmetry requires the existence of a massless vector field  $A_\mu(x)$ .

## A.2 Spontaneously Symmetry Breaking

We begin with an example where the broken symmetry is discrete. Consider the following Lagrangian:

$$\mathcal{L} = \frac{1}{2}(\partial_\mu\phi)^2 - V(\phi), \quad (\text{A.13})$$

with the potential

$$V(\phi) = -\frac{1}{2}\mu^2\phi^2 + \frac{\lambda}{4!}\phi^4. \quad (\text{A.14})$$

The Lagrangian is invariant under the operation  $\phi \rightarrow -\phi$ . The minimum of the potential  $V(\phi)$  is given by

$$\phi(x) = \phi_0 = \pm v = \pm\sqrt{\frac{6}{\lambda}}\mu. \quad (\text{A.15})$$

The constant  $v$  is called the *vacuum expectation value* of  $\phi$ . If the system is near one of the minima ( $\phi_0 = v$ ), we can define:

$$\phi(x) = v + \sigma(x). \quad (\text{A.16})$$

Rewrite the Lagrangian in terms of  $\sigma(x)$  and drop the constant terms, we get:

$$\mathcal{L} = \frac{1}{2}(\partial_\mu \sigma)^2 - \frac{1}{2}(2\mu^2)\sigma^2 - \sqrt{\frac{\lambda}{6}}\mu\sigma^3 - \frac{\lambda}{4!}\sigma^4. \quad (\text{A.17})$$

The discrete symmetry  $\phi \rightarrow -\phi$  is no longer apparent in this Lagrangian, this is called *spontaneous broken symmetry*. This Lagrangian describes a scalar field of mass  $\sqrt{2}\mu$ , with  $\sigma^3$  and  $\sigma^4$  interactions.

In the case of continuous symmetry, the theory must contain a massless particle for every spontaneously broken continuous symmetry. This is known as *Goldstone's theorem*, and the massless particles are called *Goldstone bosons*.

### A.3 The Higgs Mechanism

As discussed in Section (A.1) and (A.2), a local gauge symmetry requires the existence of a massless gauge vector field; and when a global symmetry is spontaneously broken, the theory contains massless particles, Goldstone bosons. Next, we will include both local gauge symmetry and spontaneous symmetry breaking in the same theory. It shows that spontaneous symmetry breaking generates a mass for a gauge boson. Consider a complex scalar field coupled to an electromagnetic field

$$\mathcal{L} = -\frac{1}{4}(F_{\mu\nu})^2 + |D_\mu \phi|^2 - V(\phi), \quad (\text{A.18})$$

with the potential

$$V(\phi) = -\mu^2 \phi^* \phi + \frac{\lambda}{2}(\phi^* \phi)^2. \quad (\text{A.19})$$



The Lagrangian is invariant under a global phase transformation

$$\phi(x) \rightarrow e^{i\theta} \phi(x), \quad (\text{A.20})$$

where  $\theta$  is a constant. This Lagrangian is also invariant under a local phase transformation

$$\phi(x) \rightarrow e^{i\alpha(x)} \phi(x), \quad A_\mu(x) \rightarrow A_\mu(x) - \frac{1}{e} \partial_\mu \alpha(x) \quad (\text{A.21})$$

The field acquires a vacuum expectation value

$$|\phi(x)| = \phi_0 = \sqrt{\frac{\mu^2}{\lambda}}, \quad (\text{A.22})$$

and the global symmetry is spontaneously broken.

Rewrite the complex field  $\phi(x)$  as

$$\phi(x) = \phi_0 + \frac{1}{\sqrt{2}}(\phi_1(x) + i\phi_2(x)), \quad (\text{A.23})$$

and the potential has the form

$$V(\phi) = -\frac{1}{2\lambda}\mu^4 + \frac{1}{2} \cdot 2\mu^2\phi_1^2 + \mathcal{O}(\phi_i^3). \quad (\text{A.24})$$

It describes a scalar field  $\phi_1$  of mass  $\sqrt{2}\mu$ , and  $\phi_2$  is the massless Goldstone boson.

Inserting Eqs. (A.23) to the kinetic energy term  $|D_\mu(\phi)|^2$ , we get a mass term:

$$\frac{1}{2}m_A^2 A_\mu A^\mu, \quad (\text{A.25})$$

where the mass

$$m_A^2 = 2e^2\phi_0^2 \quad (\text{A.26})$$

comes from the vacuum expectation value of the field  $\phi$ .

It shows spontaneous symmetry breaking generates a mass for a gauge boson. This mechanism is called the *Higgs mechanism*.

## A.4 The GSW Electroweak Theory

Consider a theory with  $SU(2) \times U(1)$  symmetry. The scalar field transforms as follows:

$$\phi \rightarrow e^{i\alpha^a \tau^a} e^{i\beta/2} \phi, \quad (\text{A.27})$$

with  $\tau^a = \sigma^2/2$ .

The covariant derivative of  $\phi$  is

$$D_\mu \phi = (\partial_\mu - igA_\mu^a \tau^a - i\frac{1}{2}g'B_\mu)\phi, \quad (\text{A.28})$$

where  $A_\mu^a$  and  $B_\mu$  are the  $SU(2)$  and  $U(1)$  gauge bosons respectively. As in Section (A.3), the gauge boson mass terms arise from the vacuum expectation value  $\phi_0$  of the field  $\phi$ . If  $\phi_0$  has the form

$$\phi_0 = \frac{1}{\sqrt{2}} \begin{pmatrix} 0 \\ v \end{pmatrix}, \quad (\text{A.29})$$

the mass terms will be

$$\begin{aligned} \Delta\mathcal{L} &= \frac{1}{2} \begin{pmatrix} 0 & v \end{pmatrix} (gA_\mu^a \tau^a + \frac{1}{2}g'B_\mu) (gA^{\mu b} \tau^b + \frac{1}{2}g'B^\mu) \begin{pmatrix} 0 \\ v \end{pmatrix} \\ &= \frac{1}{2} \frac{v^2}{4} [g^2(A_\mu^1)^2 + g^2(A_\mu^2)^2 + (-gA_\mu^3 + g'B_\mu)^2]. \end{aligned} \quad (\text{A.30})$$

There are three massive vector bosons and one massless vector boson, as follows:

$$\begin{aligned}
W_\mu^\pm &= \frac{1}{\sqrt{2}}(A_\mu^1 \mp iA_\mu^2) && \text{with mass } m_W = g\frac{v}{2}; \\
Z_\mu^0 &= \frac{1}{\sqrt{g^2 + g'^2}}(gA_\mu^3 - g'B_\mu) && \text{with mass } m_Z = \sqrt{g^2 + g'^2}\frac{v}{2}; \\
A_\mu &= \frac{1}{\sqrt{g^2 + g'^2}}(g'A_\mu^3 + gB_\mu) && \text{with mass } m_A = 0.
\end{aligned} \tag{A.31}$$

We define the *weak mixing angle*,  $\theta_w$ , as the rotation angle from basis  $(A^3, B)$  to the mass eigenstate basis  $(Z^0, A)$ :

$$\begin{pmatrix} Z^0 \\ A \end{pmatrix} = \begin{pmatrix} \cos \theta_w & -\sin \theta_w \\ \sin \theta_w & \cos \theta_w \end{pmatrix} \begin{pmatrix} A^3 \\ B \end{pmatrix} \tag{A.32}$$

Comparing to Eqs. (A.31), we get:

$$\cos \theta_w = \frac{g}{\sqrt{g^2 + g'^2}}, \quad \sin \theta_w = \frac{g'}{\sqrt{g^2 + g'^2}}; \tag{A.33}$$

and

$$m_W = m_Z \cos \theta_w. \tag{A.34}$$

Next consider the coupling of the vector fields to fermions. The covariant derivative takes the form

$$D_\mu = (\partial_\mu - igA_\mu^a T^a - ig'Y B_\mu) \tag{A.35}$$

In terms of the mass eigenstate fields, it becomes

$$\begin{aligned}
D_\mu &= \partial_\mu - i \frac{g}{\sqrt{2}} (W_\mu^+ T^+ + W_\mu^- T^-) - i \frac{1}{\sqrt{g^2 + g'^2}} Z_\mu (g^2 T^3 - g'^2 Y) \\
&\quad - i \frac{gg'}{\sqrt{g^2 + g'^2}} A_\mu (T^3 + Y) \\
&= \partial_\mu - i \frac{g}{\sqrt{2}} (W_\mu^+ T^+ + W_\mu^- T^-) - i \frac{g}{\cos \theta_w} Z_\mu (T^3 - \sin^2 \theta_w Q) - ie A_\mu Q,
\end{aligned} \tag{A.36}$$

where

$$T^\pm = \frac{1}{2}(\sigma^1 \pm i\sigma^2) = \sigma^\pm, \quad Q = T^3 + Y, \tag{A.37}$$

$$e = \frac{gg'}{\sqrt{g^2 + g'^2}} = g \sin \theta_w. \tag{A.38}$$

It shows all the couplings can be described by two parameters: the electron charge  $e$  and the weak mixing angle  $\theta_w$ . The Glashow-Weinberg-Salam Electroweak theory thus unifies the weak and electromagnetic interactions.

## Bibliography

- [1] Gordon Kane. The Dawn of PHYSICS BEYOND THE STANDARD MODEL. *Scientific American*, June 2003.
- [2] The standard model of particle physics. *Nature Insight*, 448:270, 19 July 2007.
- [3] Standard Model of Fundamental Particles and Interactions. Available at: [http://upload.wikimedia.org/wikipedia/en/4/4c/Particle\\_chart.jpg](http://upload.wikimedia.org/wikipedia/en/4/4c/Particle_chart.jpg).
- [4] M. Peskin and D. Schroeder. *An Introduction to Quantum Field Theory*.
- [5] Donald H. Perkins. *Introduction to High Energy Physics*. 2000.
- [6] Gargamelle was a bubble chamber detector, designed mostly for the detection of neutrinos. With a diameter of nearly 2 meter and 4.8 meter in length, Gargamelle held nearly 12 cubic meters of freon (CF<sub>3</sub>Br). It operated for many years at the CERN Proton Synchrotron(PS) and Super Proton Synchrotron(SPS).
- [7] G. Arnison et al. UA1 Collaborations. Experimental observation of isolated large transverse energy electrons with associated missing energy at  $\sqrt{s} = 540$  GeV . *Phys. Lett. 122B*, page 103, 1983.
- [8] M. Banner et al. UA2 Collaborations. Observation of single isolated electrons of high transverse momentum in events with missing transverse energy at the CERN  $\bar{p}p$  collider . *Phys. Lett. 122B*, page 476, 1983.
- [9] G. Arnison et al. UA1 Collaboration. Experimental Observation of Lepton Pairs of Invariant Mass around 95 GeV/c<sup>2</sup> at the CERN SPS Collider . *Phys. Lett. 126B*, page 398, 1983.
- [10] The Nobel prize in physics, available at: [http://www-cdf.fnal.gov/upgrades/tdr/tdr\\_3\\_cot.html](http://www-cdf.fnal.gov/upgrades/tdr/tdr_3_cot.html).
- [11] S. Chuang et al. CDF Collaboration. Search for a Standard-Model Higgs Boson in WW Dilepton Decay Channels with 200/pb Run II Data at CDF . *CDF-note 7152*.
- [12] L3 OPAL the LEP Electroweak Working Group LEP Collaborations ALEPH, DELPHI and the SLD Heavy Flavour Group. A Combination of Preliminary Electroweak Measurements and Constraints on the Standard Model . *CERN-EP-2002-091*, v3:hep-ex/0212036 v3, 2002.
- [13] D. Amidei et al. CDF Collaboration. First Measurements of Inclusive W and Z Cross Sections from Run II of the Tevatron Collider. *CDF note-7332*.

- [14] Emily Nurse CDF Collaboration. W mass and width measurements at the Tevatron, available at: [http://fcdfwww.fnal.gov/physics/ewk/2007/wwidth/index\\_files/nurse\\_moriond\\_QCD.ps](http://fcdfwww.fnal.gov/physics/ewk/2007/wwidth/index_files/nurse_moriond_QCD.ps).
- [15] T. Aaltonen et al. CDF Collaboration. First Measurement of the W Boson Mass in Run II of the Tevatron. *hep-ex/0707.0085*.
- [16] Evidence for ZZ production in  $p\bar{p}$  collision at  $\sqrt{s} = 1.96$  TeV, CDF internal note 8775.
- [17] Cdf run 2 electroweak public results. Available at: <http://fcdfwww.fnal.gov/physics/ewk/>.
- [18] Mark S. Neubauer for the CDF and D0 Collaborations. Diboson physics at the tevatron. *hep-ex/0605066*.
- [19] A. Nagano et al. Measurement of the  $W\gamma \rightarrow e\nu\gamma$  Cross Sections using 1 fb<sup>-1</sup> of CDF Data. *CDF note 8756*.
- [20] F. Abe et al. CDF Collaboration. Limits on z-photon couplings from p- $\bar{p}$  interactions at  $\sqrt{s} = 1.8$  tev. *Physics Review Letters*, 74:1941, 1995.
- [21] V.M. Abazov et al. D0 Collaboration.  $Z\gamma$  production and limits on anomalous  $ZZ\gamma$  and  $Z\gamma\gamma$  couplings in p  $\bar{p}$  collisions at  $\sqrt{s} = 1.96$  TeV . *Physics Letter B*, 653:378, 2007.
- [22] Ron Moore. FNAL Accelerator Complex 101: What s Happening in the Machines? April 2005. Accelerator Lectures for CDF Ace Training, available at: [http://www-cdfonline.fnal.gov/ops/ace2helpaccelerator\\_guide/moore\\_ace\\_20050420.pdf](http://www-cdfonline.fnal.gov/ops/ace2helpaccelerator_guide/moore_ace_20050420.pdf).
- [23] Concepts Rookie Book v3.1. November 2006. Available at: [http://www-bdnew.fnal.gov/operations/rookie\\_books/rbooks.html](http://www-bdnew.fnal.gov/operations/rookie_books/rbooks.html).
- [24] Linac Rookie Book. July 2006. Available at: [http://www-bdnew.fnal.gov/operations/rookie\\_books/rbooks.html](http://www-bdnew.fnal.gov/operations/rookie_books/rbooks.html).
- [25] <http://www2.slac.stanford.edu/vvc/accelerators/structure.html>.
- [26] <http://www-bd.fnal.gov/public/synchrotrons.html>.
- [27] <http://www-bd.fnal.gov/public/proton.html>.
- [28] <http://www-bd.fnal.gov/public/antiproton.html>.
- [29] Tevatron Rookie Book. September 2006. Available at: [http://www-bdnew.fnal.gov/operations/rookie\\_books/rbooks.html](http://www-bdnew.fnal.gov/operations/rookie_books/rbooks.html).

- [30] Roger Dixon. Accelerator status & plans for Run 2. February 2006. available at: [http://www-cdf.fnal.gov/internal/WebTalks/Archive/0702/070201\\_collab/02\\_070201\\_collab\\_m2\\_roser\\_CDF.pdf](http://www-cdf.fnal.gov/internal/WebTalks/Archive/0702/070201_collab/02_070201_collab_m2_roser_CDF.pdf).
- [31] J. Ellis et al. The Phenomenology of the Next Left-handed Quarks. *Nuclear Physics*, B131:285 – 307, 1977.
- [32] Particle Data Group at Lawrence Berkeley National Labs. The Particle Adventure. available at: [http://particleadventure.org/frameless/component\\_detector.html](http://particleadventure.org/frameless/component_detector.html).
- [33] Young-Kee Kim and Nigel Lockyer. Principle Drift Chambers. April 2004. CDF Detector Lectures, available at: [http://www-cdf.fnal.gov/internal/WebTalks/Archive/0404/040422\\_cot/01\\_040422\\_cot\\_YoungKee\\_Nigel\\_1\\_ykkim\\_COT\\_April04.pdf](http://www-cdf.fnal.gov/internal/WebTalks/Archive/0404/040422_cot/01_040422_cot_YoungKee_Nigel_1_ykkim_COT_April04.pdf).
- [34] A Brief Description of Run II Detector. July 2004. Available at: [http://www-cdf.fnal.gov/internal/detectors/cdf\\_det.ps](http://www-cdf.fnal.gov/internal/detectors/cdf_det.ps).
- [35] CDF Run II Detector Parameters. Available at: <http://www-cdf.fnal.gov/internal/detectors/parameters.html>.
- [36] Paul Lujan. An Ace's Guide to the CDF Run II Detector. August 2006. Available at: [http://www-cdfonline.fnal.gov/ops/ace2help/detector\\_guide/detector\\_guide.html](http://www-cdfonline.fnal.gov/ops/ace2help/detector_guide/detector_guide.html).
- [37] Christian Joram. CERN Summer Student Lectures 2001, Particle Detectors.
- [38] Tom LeCompte. A Tutorial on CDF Muon Identification. July 2001. available at: [http://www-cdfonline.fnal.gov/ops/cdf\\_muon/docs/muon\\_tutorial\\_TLCompte.pdf](http://www-cdfonline.fnal.gov/ops/cdf_muon/docs/muon_tutorial_TLCompte.pdf).
- [39] Kevin Lannon. Everything I Know About CMU Charge Division, I Learned From Lee, CDF note 5715.
- [40] The CDF II Detector Technical Design Report. *FERMILAB-Pub-96/390-E*, nov 1996.
- [41] The CDF II Detector Technical Design Report. Central Outer Tracker (COT), available at: [http://www-cdf.fnal.gov/upgrades/tdr/tdr\\_3\\_cot.html](http://www-cdf.fnal.gov/upgrades/tdr/tdr_3_cot.html).
- [42] et al. L. Balka. The CDF Detector, An Overview. *Nucl. Instr. & Meth.*, A 267:272, 1988.

- [43] Chengju Lin. Trigger Philosophy. November 2004. CDF Detector Lectures, available at: [http://www-cdf.fnal.gov/internal/WebTalks/Archive/0411/041118\\_detector\\_lecture\\_cdf\\_trigger/01\\_041118\\_detector\\_lecture\\_cdf\\_trigger\\_ChengJu\\_Lin\\_1\\_cjl\\_cjl\\_intro\\_trigger.pdf](http://www-cdf.fnal.gov/internal/WebTalks/Archive/0411/041118_detector_lecture_cdf_trigger/01_041118_detector_lecture_cdf_trigger_ChengJu_Lin_1_cjl_cjl_intro_trigger.pdf).
- [44] Peter Wilson. Run IIb Trigger & Data Acquisition Upgrades. October 2005. CDF Collaboration Meeting.
- [45] S. Abachi et al. D0 Collaboration. Studies of gauge boson pair production and trilinear couplings. *PHYSICAL REVIEW D*, 56:6742, 1997.
- [46] U. Baur and E.L. Berger. Probing the  $WW\gamma$  vertex at the Fermilab Tevatron Collider. *PHYSICAL REVIEW D*, 41:1476, 1990.
- [47] K. Hagiwara *et al.* Probing the weak boson sector in  $e^+e^- \rightarrow W^+W^-$ . *Nuc. Phys. B*, 282:253, 1987.
- [48] G. J. Gounaris *et al.* Signatures of the anomalous  $Z\gamma$  and  $ZZ$  production at lepton and hadron colliders. *PHYSICAL REVIEW D*, 61:073013, 2000.
- [49] G. J. Gounaris *et al.* New and standard physics contributions to anomalous  $Z$  and  $\gamma$  self-couplings. *PHYSICAL REVIEW D*, 62:073013, 2000.
- [50] U. Baur and E.L. Berger. Probing the weak-boson sector in  $Z\gamma$  production at hadron colliders. *PHYSICAL REVIEW D*, 47:4889, 1993.
- [51] The Pythia Program. Available at: <http://www.thep.lu.se/~torbjorn/Pythia.html>.
- [52] The LHAPDF Interface. Available at: <http://vircol.fnal.gov/>.
- [53] J. Ohnemus. Hadronic  $Z\gamma$  production with QCD corrections and leptonic decays. *PHYSICAL REVIEW D*, 51:1068, 1995.
- [54] Helen Hayward. Measurement of  $Z\gamma$  Production in  $p\bar{p}$  Collisions at  $\sqrt{s} = 1.96$  TeV. *CDF note 7996, PhD thesis*.
- [55] H.L. Lai et al. Global QCD Analysis of Parton Structure of the Nucleon: CTEQ5 Parton Distributions. *Eur.Phys.J. C12 (2000) 375-392*, pages 375–392, 2000. hep-ph/9903282v3.
- [56] GOOD RUN LIST v13 Page. Available at: <http://www-cdf.fnal.gov/internal/dqm/goodrun/v13/goodv13.html>.
- [57] Loose Electron Baseline Cuts. Available at: [http://www-cdf.fnal.gov/internal/physics/joint\\_physics/instructions/electron\\_cuts\\_gen6.html](http://www-cdf.fnal.gov/internal/physics/joint_physics/instructions/electron_cuts_gen6.html).



- [58] Larry Nodulman. Curvature Corrections for 5.3.1 and 6.1.1. *CDF note 6971*.
- [59] Sam Harper et al. Very High-Pt Electron Identification. *CDF note 7527*.
- [60] J. Deng et al. Z Selection in Z + X Analysis. *CDF note 8505*.
- [61] J. Incandela T. Spreitzer, C. Mills. Electron Identification in Offline Release 6.1.2 . *CDF note 7950*.
- [62] First Measurements of Inclusive W and Z Cross Sections from Run II of the Tevatron Collider. *CDF note 7332*.
- [63] Measurement of the Z Production Cross Section. *CDF note 7865*.
- [64] Event  $|Z_{vtx}| < 60$  Cut Acceptance for Run II (to Aug04). *CDF note 7324*.
- [65] Joint Physics baseline cuts for high Pt photons(v2.3). Available at: <http://www-cdf.fnal.gov/internal/physics/photon/docs/cuts.html>.
- [66] S-M Wynne. Very High-Pt Photon Efficiency Scale Factors V.2. *CDF note 7947, V2.0*.
- [67] H. Hayward *et al.* Determination of the Probability of a Jet to fake an Isolated Photon. *CDF note 6363*.
- [68] H. Hayward *et al.* Update of the Measurement of the Probability of a Jet faking an Isolated photon. *CDF note 6838*.
- [69] Chris Lester *et al.* Measurement of the Rate of Jets Faking Central Isolated Photons Using  $1 \text{ fb}^{-1}$  of Data. *CDF note 9033*.
- [70] Thomas J. Phillips et al.  $Z \rightarrow \mu\mu\gamma$  Production in  $2 \text{ fb}^{-1}$ . *CDF note 9088*.
- [71] Max Goncharov et al. Search for the new physics in the exclusive  $\gamma + \cancel{E}_t$  final state. *CDF note 8979*.
- [72] The Nobel Prize in Physics 1999. Available at: [http://nobelprize.org/nobel\\_prizes/physics/laureates/1999/press.html](http://nobelprize.org/nobel_prizes/physics/laureates/1999/press.html).
- [73] D. Acosta et al. CDF Collaboration. Measurement of the  $W^+W^-$  Production Cross Section in  $p\bar{p}$  Collisions at  $\sqrt{s} = 1.96 \text{ TeV}$  using Dilepton Events . *CDF PRL draft v1*.
- [74] S. Cabrera et al. CDF Collaboration. Measurement of ZZ+ZW cross section at CDF in Run II . *CDF note-6920*.
- [75] F. Abe et al. CDF Collaboration. Evidence for Top Quark Production in  $p\bar{p}$  Collisions at  $\sqrt{s} = 1.8 \text{ TeV}$  . *FERMILAB-PUB-94/097-E*.

- [76] V. Barger and R. Phillips. *Collider Physics* . 1996.
- [77] P. Ratoff. SUSY SEARCHES AT THE TEVATRON, available at: <http://www.hep.lancs.ac.uk/pnrtalks/IDM2002.doc>.
- [78] <http://www-boone.fnal.gov/public/introduction/pics/booster1new.jpg>.
- [79] Rob Roser. Particle Physics Detectors - Lecture 1. 2006 Hadron Collider Physics Summer School at Fermilab, available at: [http://www-cdfonline.fnal.gov/ops/ace2help/detector\\_guide/detector\\_guide.html](http://www-cdfonline.fnal.gov/ops/ace2help/detector_guide/detector_guide.html).
- [80] G. P. Lepage. A New Algorithm for Adaptive Multidimensional Integration. *J. Comput. Phys.*, 27:192, 1978.
- [81] D.Stump et al. Inclusive Jet Production, Parton Distributions, and the Search for New Physics. *hep-ph/0303013*.
- [82] Sam Harper et al. Reconstructing the Plug Electron Electron Energy in 5.3.3. *CDF note 7687*.
- [83] J. Deng et al. Measurement of  $Z\gamma$  Production using 1  $fb^{-1}$  of CDF RUN II Data. *CDF note 8506*.
- [84] <http://atlas.web.cern.ch/Atlas>.
- [85] ATLAS Annual Reports . <http://atlas.web.cern.ch/Atlas/internal/Welcome.html>.
- [86] Electrons, photons and muons in ATLAS. *EPJ Direct, Sect. A-E: 4 (2002) no. CS1, pp.7*. <http://cdsweb.cern.ch/search.py?recid=533231\&ln=en>.
- [87] [http://atlas.web.cern.ch/Atlas/GROUPS/INNER/\\_DETECTOR/SCT/gallery/lhc/lhcunder.jpg](http://atlas.web.cern.ch/Atlas/GROUPS/INNER/_DETECTOR/SCT/gallery/lhc/lhcunder.jpg).
- [88] <http://www-wisconsin.cern.ch/images/atlas.jpg>.
- [89] David J. Miller. The higgs mechanism. <http://www.hep.ucl.ac.uk/~djm/higgsa.html>.
- [90] Steven Weinberg. A unified physics by 2050? *Scientific American*, December 1999.

## Biography

Jianrong Deng was born on January 15, 1975 in Lianchen, China. She is the third child of Shuixing Deng and Huiqun Chen. She is the younger sister of Cailing Deng and Jianhui Deng and elder sister of Jianzhi Deng.

Jianrong attended Sichuan University in Chengdu, Sichuan, where she earned her Bachelor of Science in physics in 1996. She then attended China Institute of Atomic Energy, where she earned her Master of Science in physics in 1999. She matriculated to Duke University in 2002. In 2004, she moved to Chicago and began to work on “ $Z + \gamma$  production at CDF”.

After graduating from Duke in 2008, she will join the ATLAS experiment at LHC working for the University of California at Irvine.